ISSN 2518-7198 (Print)
ISSN 2663-5089 (Online)

BULLETIN
OF THE KARAGANDA UNIVERSITY

PHYSICS
Series

№ 4(112)/2023

ISSN 2663-5089 (Online)
ISSN-L 2518-7198 (Print)
Индексі 74616
Индекс 74616

ҚАРАҒАНДЫ УНИВЕРСИТЕТІНІҢ ХАБАРШЫСЫ

ВЕСТНИК КАРАГАНДИНСКОГО УНИВЕРСИТЕТА

BULLETIN OF THE KARAGANDA UNIVERSITY

ФИЗИКА сериясы

Серия ФИЗИКА

PHYSICS Series

№ 4(112)/2023

Қазан–қараша–желтоқсан
30 желтоқсан 2023 ж.
Октябрь–ноябрь–декабрь
30 декабря 2023 г.
October–November–December
December, 30th, 2023

1996 жылдан бастап шығады
Издается с 1996 года
Founded in 1996

Жылына 4 рет шығады
Выходит 4 раза в год
Published 4 times a year

Қарағанды, 2023
Караганда, 2023
Karaganda, 2023

Редакцияның мекенжайы: 100024, Қазақстан, Қарағанды қ., Университет к-сі, 28
Тел.: +7 701 531 4758; факс: (7212) 35-63-98.
E-mail: vestnikku@gmail.com; karabekova71@mail.ru
Сайты: physics-vestnik.ksu.kz

Атқарушы редактор

PhD д-ры **Г.Б. Саржанова**

Редакторлары

Ж.Т. Нурмуханова, С.С. Балкеева, И.Н. Муртазина

Компьютерде беттеген

М.С. Бабатаева

Қарағанды университетінің хабаршысы. «Физика» сериясы. — 2023. — № 4(112). — 101 б. — ISSN-L 2518-7198 (Print). ISSN 2663-5089 (Online).

Меншік иесі: «Академик Е.А. Бөкетов атындағы Қарағанды университеті» КЕАҚ.

Қазақстан Республикасы Ақпарат және қоғамдық даму министрлігімен тіркелген. 30.09.2020 ж. № KZ38VPY00027378 қайта есепке қою туралы куәлігі.

Басуға 29.12.2023 ж. қол қойылды. Пішімі 60×84 1/8. Қағазы офсеттік. Көлемі 12,62 б.т. Таралымы 200 дана. Бағасы келісім бойынша. Тапсырыс № 109.

«Акад. Е.А. Бөкетов ат. Қарағанды ун-ті» КЕАҚ баспасының баспаханасында басылып шықты.
100024, Қазақстан, Қарағанды қ., Университет к-сі, 28. Тел. (7212) 35-63-16. E-mail: izd_kargu@mail.ru

Адрес редакции: 100024, Казахстан, г. Караганда, ул. Университетская, 28
Тел.: +7 701 531 4758. Факс: (7212) 35–63–98.
E-mail: vestnikku@gmail.com; karabekova71@mail.ru
Сайт: physics-vestnik.ksu.kz

Вестник Карагандинского университета. Серия «Физика». — 2023. — № 4(112). — 101 с. — ISSN-L 2518-7198 (Print). ISSN 2663-5089 (Online).

Собственник: НАО «Карагандинский университет имени академика Е.А. Букетова».

Зарегистрирован Министерством информации и общественного развития Республики Казахстан. Свидетельство о постановке на переучет № KZ38VPY00027378 от 30.09.2020 г.

Подписано в печать 29.12.2023 г. Формат 60×84 1/8. Бумага офсетная. Объем 12,62 п.л. Тираж 200 экз. Цена договорная. Заказ № 109.

Отпечатано в типографии издательства НАО «Карагандинский университет им. акад. Е.А. Букетова». 100024, Казахстан, г. Караганда, ул. Университетская, 28. Тел.(7212) 35-63-16. E-mail:izd_kargu@mail.ru

Postal address: 28, University Str., 100024, Karaganda, Kazakhstan

Tel.: +7 701 531 4758; Fax: (7212) 35-63-98.

E-mail: vestnikku@gmail.com; karabekova71@mail.ru

Web-site: physics-vestnik.ksu.kz

Bulletin of the Karaganda University. "Physics" Series. — 2023. — № 4(112). — 101 p. — ISSN-L 2518-7198 (Print). ISSN 2663-5089 (Online).

Proprietary: NLC "Karagandy University of the name of academician E.A. Buketov".

Registered by the Ministry of Information and Social Development of the Republic of Kazakhstan. Rediscount certificate No. KZ38VPY00027378 dated 30.09.2020.

Signed in print 29.12.2023. Format 60×84 1/8. Offset paper. Volume 12,62 p.sh. Circulation 200 copies. Price upon request. Order № 109.

Printed in the Publishing house of NLC "Karagandy University of the name of acad. E.A. Buketov".
28, University Str., Karaganda, 100024, Kazakhstan. Tel. (7212) 35-63-16. E-mail: izd_kargu@mail.ru

МАЗМҰНЫ — СОДЕРЖАНИЕ — CONTENT

КОНДЕНСАЦИЯЛАНҒАН КҮЙДІҢ ФИЗИКАСЫ
ФИЗИКА КОНДЕНСИРОВАННОГО СОСТОЯНИЯ
PHYSICS OF THE CONDENSED MATTER

ТЕХНИКАЛЫҚ ФИЗИКА
ТЕХНИЧЕСКАЯ ФИЗИКА
TECHNICAL PHYSICS

ЖЫЛУФИЗИКАСЫ ЖӘНЕ ТЕОРИЯЛЫҚ ЖЫЛУТЕХНИКАСЫ
ТЕПЛОФИЗИКА И ТЕОРЕТИЧЕСКАЯ ТЕПЛОТЕХНИКА
THERMOPHYSICS AND THEORETICAL THERMOENGINEERING

DOI 10.31489/2023PH4/6-13

UDC 541.145

A.S. Kayumova[1], S.V. Savilov[2], P.A. Zhanbirbayeva[1], A.S. Baltabekov[1], M.S. Dzhakupova[1], T.M. Serikov[1*]

[1]Karaganda Buketov University, Karaganda, Kazakhstan;
[2]M.V. Lomonosov Moscow State University, Moscow, Russia
[*]Corresponding author's e-mail: serikov-timur@mail.ru

Effect of TNR/Ag/rGO film area on its photocatalytic activity

This paper presents the results of a study of the effect of the area of nanocomposite films formed by titanium dioxide nanorods, silver nanoparticles and reduced graphene oxide (TNR/Ag/rGO) on its photocatalytic activity. The active area of the nanocomposite films was S=1cm^2, S=1.5cm^2, S=2cm^2, S=3cm^2. The photocatalytic activity of the samples was assessed by the value of the generated photocurrent per unit surface of the film and the photodegradation of the methylene blue dye when the surface was illuminated with a light source from a xenon lamp (300 W). A film with an area of 1 cm^2 generated 0.00042 A/cm^2. With increasing film area S=1.5 cm^2, S=2cm^2, S=3cm^2, the photocurrent density was 0.00035 A/cm^2, 0.00028 A/cm^2, 0.00013 A/cm^2, respectively. It was found that in the absence of a nanocomposite film, the degradation of the dye is negligible. When the TNR/Ag/rGO film was immersed in a dye solution, the degradation of the dye increased and amounted to 32, 59, 70 and 81 % for S=1cm^2, S=1.5 cm^2, S=2cm^2, S=3cm^2 with an irradiation duration of 240 minutes. The results obtained suggested that as the active surface area of the films increases, their photocatalytic activity decreases. The decrease in photocatalytic activity is associated with surface defects and an increase in film resistance.

Keywords: titanium dioxide nanorods, silver nanoparticles, reduced graphene oxide, film area, photocatalysis.

Introduction

Titanium dioxide (TiO_2) is a promising semiconductor material in photocatalysis due to its optical, structural, electrical characteristics, high chemical stability, low toxicity, low cost and high photocatalytic activity [1-4]. Among the variety of TiO_2 nanostructures, such as nanoparticles, nanostitches, nanotubes and nanothreads, materials with one-dimensional transport of charge carriers are more promising [5]. One of these is titanium dioxide nanorod (TNR), obtained by hydrothermal synthesis. By controlling the synthesis conditions, for example, temperatures, concentrations of chemical reagents and the number of synthesis stages, it is possible to control the geometric characteristics of TNR and films based on them [6]. Along with the above advantages, films based on TNR have a number of disadvantages, the main of which are low absorption capacity in the visible range of the electromagnetic wave and the high rate of recombination of electron-hole pairs [7]. There are many methods and approaches to expand the spectral sensitivity of TNR, for example, introducing into the structure semiconductors with a narrower band gap, such as CdS CdSe CuO, etc. [8-10]. The introduction of nanoparticles of noble metals Au, Ag, Cu is also promising, while the absorption capacity is enhanced due to hot electrons of the metals and due to surface plasmon resonance [11-13]. To suppress the rate of recombination of electron-hole pairs, graphene nanostructures are applied to the surface or into the pores of TiO_2 nanostructures by electrochemical deposition or airbrush sputtering [14]. Graphene can serve as both an effective conductor, facilitating efficient charge transfer, and absorb visible light, which

increases sensitivity to it. By integrating TiO_2 with graphene, an improvement in the electronic and photoelectric behavior of the material is achieved. This method can overcome some of the disadvantages of one-dimensional TNR structures and create more efficient photocatalysts with reduced recombination and a wider spectrum of light sensitivity [15, 16].

In our previous works, as well as in a number of other sources, it was shown that the introduction of nanoparticles of noble metals Ag and reduced graphene oxide (rGO) into the TiO_2 structure significantly improves its photocatalytic activity [17-21]. When assessing the photocatalytic activity of TNR or TNR/Ag/rGO films, a film area of the order of 1 cm^2 was typically used. If the cost of the materials used is reduced, this technology can potentially be commercialized. In this case, there will be a need to create films on an industrial scale, which will lead to an increase in its area. However, a literature review showed that the published works lack information on the effects of film area on its photocatalytic activity, which is the goal of this work.

Experimental

To obtain TNR/Ag/rGO films with different areas, glass substrates with a conductive FTO layer (8 Ohm/cm^2, Sigma–Aldrich) were cut into geometric dimensions, as shown in Figure 1.

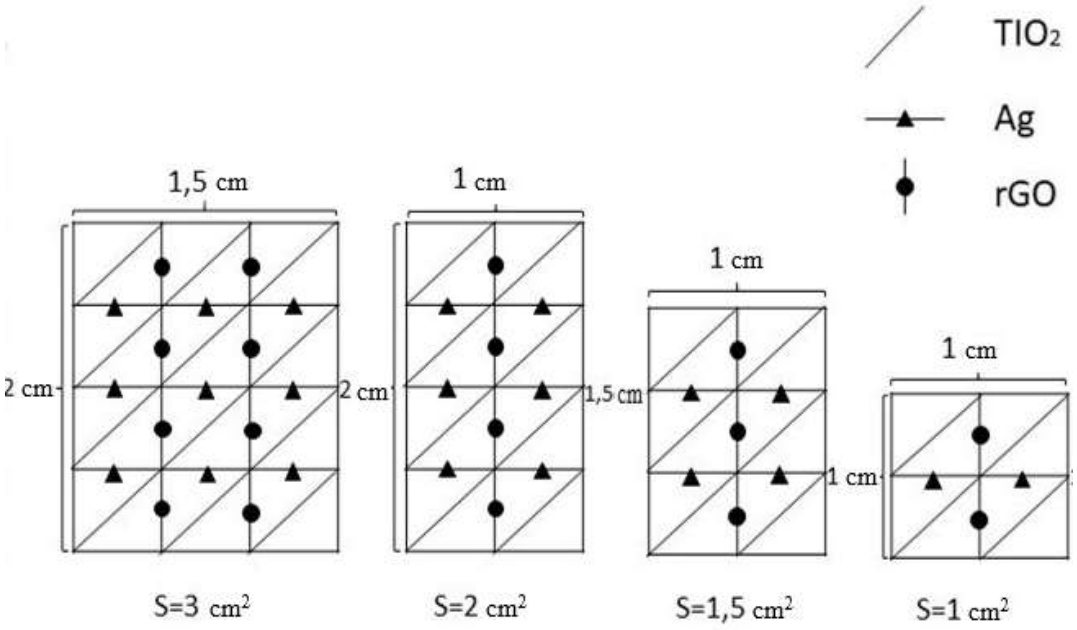

Figure 1. Schematic representation of films with different areas.

TNR with a rutile phase was obtained by hydrothermal synthesis in a stainless steel autoclave with a fluoroplastic vessel. To do this, 12 ml of deionized water, 12 ml of hydrochloric acid (36.5 %, Karagandareaktivsbyt), 0.275 ml of $C_{16}H_{36}O_4Ti$ (97 %, Sigma-Aldrich) were poured into a vessel with a volume of 50 ml and mixed in an ultrasonic bath for 3 minutes. Then, the pre-cleaned FTO glass substrates were placed into a vessel with the conductive side up, sealed tightly and placed in an electronic oven (8.2/1100, SNOL) for 6 hours at a temperature of 180^0C. After cooling, the samples were removed, thoroughly washed with deionized water and subjected to heat treatment in an oven at a temperature of 500^0C for 2 hours. The introduction of silver (Ag) nanoparticles was carried out by chemical deposition. To 0.2 g of polyvinylpyrrolidone (PVP), 20 ml of H_2O and 20 ml of $C_2H_6O_2$ and 2 mmol of $NaBH_4$ were added. The substrates were kept in an oven at 70 °C for 2 minutes, washed with deionized water and dried at room temperature rGO (99 %, Cheaptubes) was deposited onto the surface by electrochemical deposition. The rGO powder was dispersed in a phosphate solution (0.5 g/L), then treated in an ultrasonic bath for 2 hours. The deposition of rGO onto the TNR/Ag surface was carried out using a standard three-electrode system. The working electrode was TNR/Ag, the counter electrode was Pt foil, and the reference electrode was Ag/AgCl. After 5 minutes of deposition, the films were removed and washed several times with deionized water.

The surface morphology and microstructure of the resulting composite was studied using a Mira 3MLU scanning electron microscope (SEM) (Tescan). Spectrophotometric measurements were carried out on a Solar CM 2203 scanning spectrophotometer (Solar) in the wavelength range 190-750 nm. The film resistance was determined using the impedance spectroscopy method in the frequency range from 1 MHz to 100 MHz. For this purpose, the working electrode (test samples) and the counter electrode made of Pt (Platisol T/SP, Solaronix) deposited on FTO were glued together with a polymer film 25 μm thick (Melotonix, Solaronix). The electrolyte used was iodide/triiodide electrolyte (Iodolyte Z-150, Solaronix). The photocatalytic activity of the samples was assessed by measuring the photoinduced current with an illuminated area of 1 cm^2 in a standard three-electrode cell using a CS350 potentiostat/galvanostat with a built-in EIS analyzer (Corrtest Instruments, China). Platinum foil served as the counter electrode, and an AgCl electrode was used as the reference electrode. The measurements were carried out in a 0.1 M NaOH electrolyte in a specially manufactured photoelectrochemical cell with a quartz window. In addition, the photoactivity of the films was assessed by photodegradation of the methylene blue (MB) dye. Methylene blue dye is used as a model pollutant. A xenon lamp with a power of 300 W/cm^2 was used as a radiation source in all experiments (Newport, USA).

Results and discussion

Figure 2 (a, b) shows micrographs of the surface morphology of the TNR film before and after deposition of Ag and rGO nanoparticles. Figure 2a shows that as a result of hydrothermal synthesis, titanium dioxide nanorods are formed on the surface of the FTO substrate, mainly perpendicular to the surface of the substrate. The length of the nanorods is about 2.1 microns, the average diameter of the nanorods is 80-90 nm. As a result of the chemical reduction of silver nitrate, Ag nanoparticles are formed on the TNR surface. The deposited Ag nanoparticles are evenly distributed over the entire surface of the samples and envelope the walls of TNR films, at the same time creating roughness. The average diameter of nanoparticles is 25-30 nm. Also, on the surface of TNR/Ag films, rGO sheets are visible, which were deposited by electrochemical method. The figure shows that graphene sheets partially envelop the TNR/Ag surface.

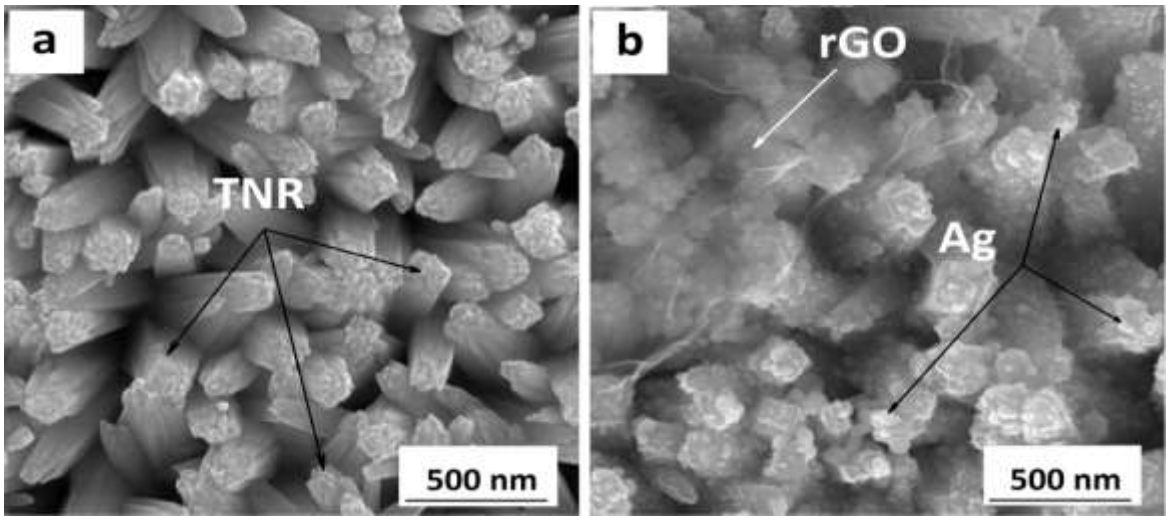

Figure 2. SEM images of the TNR surface before (a) and after (b) deposition of Ag and rGO.

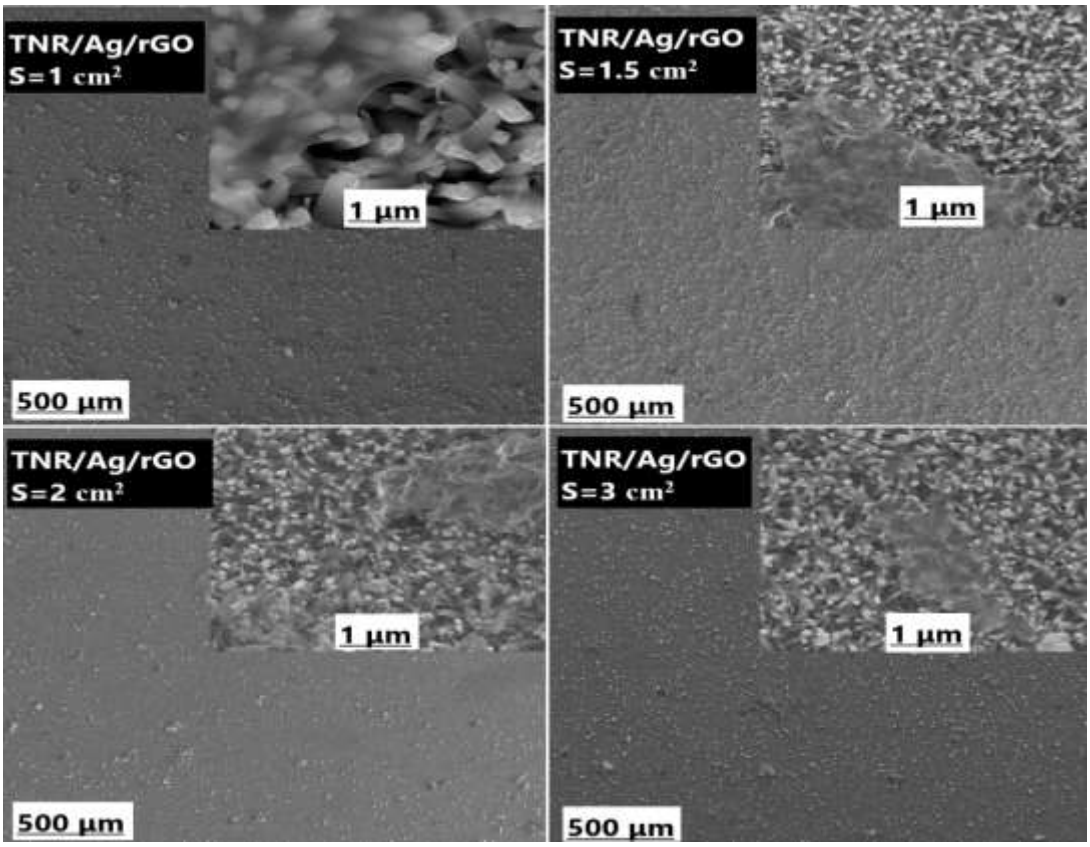

Figure 3. Surface morphology of samples.

Figure 3 shows micrographs of TNR/Ag/rGO films with different areas. The figure shows that increasing the area of the TNR/Ag/rGO film obtained by hydrothermal synthesis does not lead to significant changes in the structure. The film surface is smooth, without visible surface defects.

The photocatalytic activity of the nanocomposites was assessed by the degradation of methylene blue (MB) dye. MB is used as a model dye, which is the source of any contaminants. When films placed in an aqueous solution of this dye are irradiated with light rays, a decrease in the optical density of the dye is observed, which indicates the gradual degradation of molecules in the solution under the influence of light rays. For each sample, an aqueous solution of MB dye with a concentration of 10^{-6} mol/L was poured into a container with a different volume, and the optical density of the dye was determined at certain time intervals. MB volume

S= 3.0 cm^2 → 60 ml
S= 2.0 cm^2 → 40 ml
S= 1.5 cm^2 → 30 ml
S= 1.0 cm^2 → 20 ml.

Figure 4a shows an example of dye photodegradation. At the absorption peak of 662 nm, a change in the absorbance of the MB dye was observed. The photodegradation curve is shown in Figure 4b. As can be seen from the figure, with long-term irradiation, the degradation of MB without a film is less pronounced. In the presence of the film formed by TNR/Ag/rGO, significant degradation of the methylene blue dye is observed (Fig. 4b). In the presence of a film with an area of 3 cm^2, the degradation of the dye over a time period of 240 minutes reached 81 %, and when using a film with an area of 2 cm^2, 1.5 cm^2 and 1 cm^2, this parameter in the specified period of time was only 70, 59, 32 %. The results obtained indicate that in a film with an area of 3 cm^2, the rate of dye degradation increases in relation to films with an area of 2 cm^2, 1.5 cm^2 and 1 cm^2.

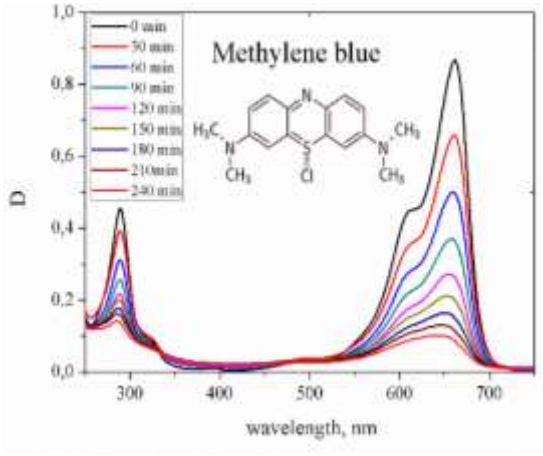

a) example of photodegradation of MB dye

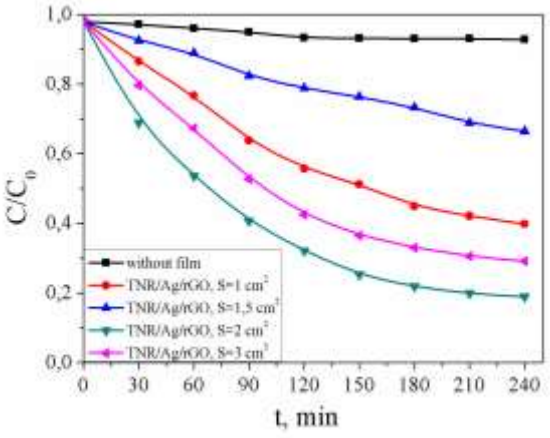

b) photodegradation curves of MB dye

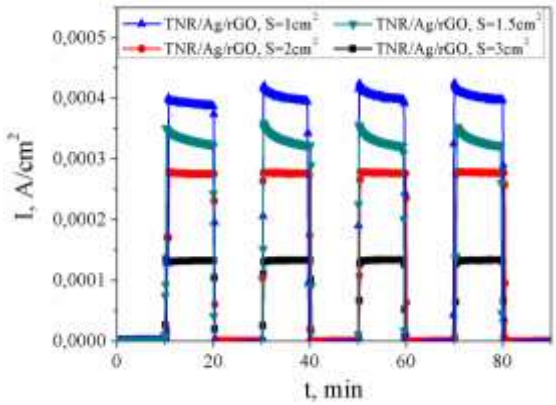

c) Photocurrent density

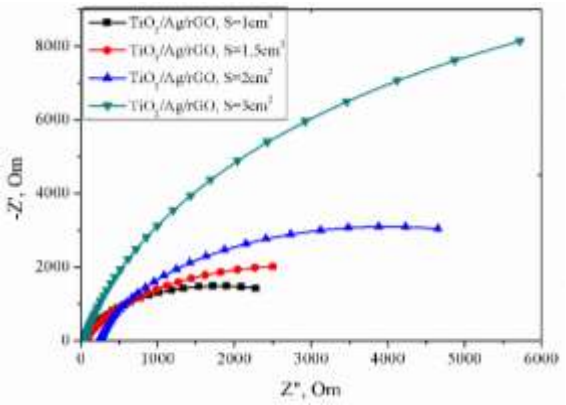

d) Impedance spectra

Figure 4. Photocatalytic properties of TNR/Ag/rGO films at different areas.

And also, the photocatalytic activity of the samples was assessed by the response of the photocurrent when irradiated with artificial sunlight with periodic on-off for 10 s. In the absence of lighting, the photocurrent is zero, but when the light is turned on, its density instantly increases. From Figure 4c it can be seen that the maximum value under illumination for a sample with an area of 1 cm^2 is 0.00042 A/cm^2, for a sample with an area of 1.5 cm^2 it is 0.00035 A/cm^2, for a sample with an area of 2 cm^2 it is 0.00028 A/cm^2 and 0.00013 A/cm^2 for a sample with an area 3 cm^2. All samples show stability over time when recording photocurrent. From the results of the study, we can see that as the area increases, its photocatalytic activity also increases. This means that it increases the likelihood of reactions and allows them to interact better with the catalyst.

Figure 4d shows impedance hodographs as a function of Nyquist coordinates for all samples studied. Using the central arc of the hodograph, which characterizes the processes occurring in the nanocomposite, the main electrical transport properties of the film were calculated using methods described in the literature [22].

The resistance to electron transport in a nanocomposite R_w and the charge transfer resistance R_k will depend directly on the number of electrons received from the number of free electrons. If we take into account that the dimensions and thickness of the semiconductor film are identical for all systems, accordingly, only the deposited layers of graphene oxide will affect the resistance value. The brief calculations performed are presented in Table.

T a b l e

Electrical transport properties of films based on nanocomposite materials

Name of samples and measurement error	R_w, Ohm	R_k, Ohm	$\omega_{max\ Hz}$	τ_{eff}, sec
TNR/Ag/rGO -1cm^2	71.4	2345.5	295.9	0.003
Error, %	9.2	2.0	-	-
TNR/Ag/rGO-1.5cm^2	55.8	2669.9	12.2	0.082
Error, %	0.7	2.6	-	-
TNR/Ag/rGO -2cm^2	242.2	4733.5	2.6	0.377
Error, %	0.9	3.7	-	-
TNR/Ag/rGO -3cm^2	43.0	5934.2	1.7	0.573
Error, %	1.6	4.1		

The resistance of TNR/Ag/rGO films with an area of 3 cm^2 is 3 times greater than that of a film with an area of 1 cm^2 and is 1902 Ohm and 5733 Ohm. And for films with an area of 1.5 cm^2, the resistance value was 2496 Ohm, and 3878 Ohm for a film with an area of 2 cm^2. Based on the hodograph, the electron lifetime τ_{eff} was calculated in films and nanocomposite materials. According to the results obtained, the effective lifetime of an electron in a sample with an area of 3 cm^2 is 0.573 seconds. Samples with an area of 2, 1.5 and 1 cm^2 with a time of 0.377, 0.082 and 0.003 seconds, respectively. It follows that as the area of the films increases, the effective lifetime of the electron in the sample increases. A long electron lifetime increases the probability of electron recombination in trap states associated with both structural and surface structural defects. In addition, as the film area increases, the film resistance also increases, which also impedes the transport of photogenerated electrons. The table also shows the measurement error values as percentages. In general, the magnitude of errors is in the confidence interval from 0.5 to 5 %.

Conclusions

Thus, it was found that as the active area of the TNR/Ag/rGO nanocomposite increases, its photocatalytic activity decreases. It was found that with the same duration of irradiation (240 min) of the dye in the presence of films, the degree of its degradation is different. In the presence of a film with an area of S=3cm^2, during the above period of time the dye reached 66 % degradation, and with S=1cm^2 the degree of dye degradation was 83 %. It should be noted that the volume of dye increased with increasing film area. Similar results were obtained for the magnitude of the generated photocurrent per unit surface of the sample.

The results obtained led to the conclusion that as the active surface area of the films increases, their photocatalytic activity decreases. The decrease in photocatalytic activity is associated with an increase in film resistance, associated with surface defects. Since the charge transfer resistance R_k increased with increasing area of the nanocomposite.

References

1 Lazar, M.A., Varghese S., & Nair, S.S. (2012). Photocatalytic water treatment by titanium dioxide: recent updates. *Catalysts, 2*(4), 572-601.

2 Zhao, Y., Hoivik, N., & Wang, K.Y. (2016). Recent advance on engineering titanium dioxide nanotubes for photochemical and photoelectrochemical water splitting. *Nano energy*, 30, 728-744.

3 Guo, Q., Zhou, C., Ma, Z., & Yang, X. (2019). Fundamentals of TiO2 Photocatalysis: Concepts, Mechanisms, and Challenges. *Advanced Materials*, 31(50).

4 Zhao, X., Zhang, G., & Zhang, Z. (2020). TiO2-based catalysts for photocatalytic reduction of aqueous oxyanions: State-of-the-art and future prospects. *Environment International*, 136, № 105453.

5 Serikov, T.M. (2020). The effect of electric transport properties of titanium dioxide nanostructures on their photocatalytic activity. *Bulletin of the University of Karaganda-Physics. 3*(99), 24–31.

6 Serikov, T.M., Ibrayev, N.Kh., Ivanova, T.M., & Savilov, S.V. (2021). Influence of the hydrothermal synthesis conditions on the photocatalytic activity of titanium dioxide nanorods. *Russian Journal of Applied Chemistry, 94*(4), 438–445.

7 Parashar, M., Shukla, V.K., & Singh, R. (2020). Metal oxides nanoparticles via sol-gel method: a review on synthesis, characterization and applications. *Journal of Materials Science-Materials in Electronics*, 31, 3729-3749.

8 Hong, L.F., Guo, R.T., Yuan, Y., Ji, X.Y., Lin, Z.D., Li, Z.S., & Pan, W.G. (2021). Recent Progress of Transition Metal Phosphides for Photocatalytic Hydrogen Evolution. *Chemsuschem, 14* (2), 539-557.

9 Wu, J., Liu, J., Xia W., Ren, Y.Y., & Wang, F. (2021). Advances on Photocatalytic CO_2 Reduction Based on CdS and CdSe Nano-Semiconductors. *ACTA PHYSICO-CHIMICA SINICA*, *37*(5).

10 Sawicka-Chudy, P., Sibinski, M., Rybak-Wilusz, E., Cholewa, M., Wisz, G., & Yavorskyi, R. (2020). Review of the development of copper oxides with titanium dioxide thin-film solar cells. *aip Advances*, *10*(1).

11 Warren, S.C. (2012). Thimsen E. Plasmonic solar water splitting. *Energy Environ*, 5, 5133-5146.

12 Cozzoli, P.D., Fanizza, E., Comparelli, R., Curri, M.L., Agostiano, A., & Laub, D. (2004). Role of metal nanoparticles in TiO_2/Ag nanocomposite-based microheterogeneous photocatalysis. *J. Phys. Chem.*, 108, 9623-9630.

13 Lang, Q., Chen, Q., Huang, T., Yang, L., Zhong, S., Wu, L., Chen, J., & Bai, S. (2018). Graphene "bridge" in transferring hot electrons from plasmonic Ag nanocubes to TiO2 nanosheets for enhanced visible light photocatalytic hydrogen evolution. *Applied Catalysis B Environmental*, 220, 182–190.

14 Zhumabekov, A.Z., Ibrayev, N.Kh., & Seliverstova, E.V. (2020). Photoelectric properties of a nanocomposite derived from reduced graphene oxide and TiO_2. *Theoretical and Experimental Chemistry*, 55, 398–406.

15 Shen, Sh., Kronawitter, C., & Kiriakidis, G. (2017). An overview of photocatalytic materials. *Journal of Materiomics*, 3, 1–2.

16 Tong, H., Zhan, X., Tian, X., Li, J., Qian, D., & Wu, D. (2018). Understanding the energy level matching relationships between semiconductor photocatalysts and organic pollutants for effective photocatalytic degradations. *Journal of Colloid and Interface Science*, 526, 384–391.

17 Serikov, T.M., Kayumova, A.S., Baltabekov, A.S., Ilyina, L.F., & Zhanbirbayeva, P.A. (2023). Photocatalytic Activity of Nanocomposites Based on Titania Nanorods and Nanotubes Doped with Ag and Reduced Graphene Oxide Nanoparticles. *Nanobiotechnology Reports*, *18*(2), 207–215.

18 Gao, W., Wang, M., Ran, C., Yao, X., Yang, H., Liu, J., He, D., & Bai, J. (2014). One-pot synthesis of Ag/r- GO/TiO2 nanocomposites with high solar absorption and enhanced anti-recombination in photocatalytic applications. *Nanoscale*, 6, 5498–5508.

19 Xiao, L., Youji, L., Chen, F, Peng, X., & Ming, L. (2017). Facile synthesis of mesoporous titanium dioxide doped by Ag-coated graphene with enhanced visible-light photocatalytic performance for methylene blue degradation. *RSC Advances*, 7, 25314–25324.

20 Fei, J.B., & Li, J.B. (2015). Controlled preparation of porous TiO2-Ag nanostructures through supramolecular assembly for plasmon-enhanced photocatalysis. *Advanced Materials*, 27, 314-319.

21 Sharma, M., Behl, K., Nigam, S., & Joshi, M. (2018). TiO2-GO nanocomposite for photocatalysis and environmental applications: A green synthesis approach. *Vacuum*, 156, 434-439.

22 Adachi, M., Sakamoto, M., Jiu, J., Ogata, Y., & Isoda, S. (2006). Determination of parameters of electron transport in dye-sensitized solar cells using electrochemical impedance spectroscopy. *Journal of Physical Chemistry B*, 110, 13872–13880.

А.С. Каюмова, С.В. Савилов, П.А. Жанбирбаева, А.С. Балтабеков,
М.С. Джакупова, Т.М. Сериков

TNR/Ag/rGO қабыршақтары ауданының фотокаталикалық белсенділігіне әсері

Мақалада титан қостотығы, күміс наноөзекшелері және қайта қалпына келтірілген графен оксиді (TNR/Ag/rGO) нанокомпозиттік қабыршақтар ауданының, оның фотокаталитикалық белсенділігіне әсері туралы зерттеу нәтижелері келтірілген. Нанокомпозиттік қабыршақтардың белсенді аудандары S=1см^2, S=1.5 см^2, S=2см^2, S=3см^2 құрайды. Үлгілердің фотокаталитикалық белсенділігі қабыршақ бетінің бірлігінен алынған фототок мөлшері және ксенон шамының (300 Вт) жарық көзімен бетті жарықтандыру кезінде метилен көк бояғыштың фотодеградациясы бойынша бағаланды. 1 см^2 ауданды қабыршақтың фототок тығыздығы 0.00042 А/см^2 құрады. Қабыршақтар ауданының ұлғаюымен S=1.5 см^2, S=2см^2, S=3см^2 фототоктың тығыздығы сәйкесінше 0.00035 А/см^2, 0.00028 А/см^2, 0.00013 А/см^2 құрады. Нанокомпозиттік қабыршақ болмаған кезде бояғыштың деградациясы шамалы екендігі анықталды. TNR/Ag/rGO қабыршағының бояғыш ерітіндісіне батырылған кездегі бояғыштың деградациясы S=1см^2, S=1.5 см^2, S=2см^2, S=3см^2 аудандарында сәулелену ұзақтығы 240 минут болғанда 32, 59, 70 және 81 % өсті. Нәтижелер қабыршақтардың аудан бетінің өсуімен, олардың фотокаталитикалық белсенділігі төмендейтінін көрсетті. Фотокаталитикалық белсенділіктің төмендеуі беткі ақаулармен және қабыршақтардың кедергілерінің жоғарылауымен байланысты.

Кілт сөздер: титан қостотығының наноөзекшелері, күміс нанобөлшектері, қайта қалпына келтірілген графен оксиді, қабыршақ ауданы, фотокатализ.

А.С. Каюмова, С.В. Савилов, П.А. Жанбирбаева, А.С. Балтабеков,
М.С. Джакупова, Т.М. Сериков

Влияние площади и пленки TNR/Ag/rGO на её фотокаталитическую активность

В статье представлены результаты исследования влияния площади нанокомпозитных пленок, образованных наностержнями диоксида титана, наночастицами серебра и восстановленного оксида графена (TNR/Ag/rGO), на её фотокаталитическую активность. Активная площадь нанокомпозитных пленок составила S=1 см^2; S=1,5 см^2; S=2 см^2; S=3 см^2. Фотокаталитическая активность образцов оценивалась по величине генерируемого фототока с единицы поверхности пленки и фотодеградации красителя метиленового голубого при освещении поверхности источником света от ксеноновой лампы (300 Вт). Пленка площадью 1 см^2 генерировала 0,00042 А/см^2. С ростом площади пленок S=1,5 см^2; S=2 см^2; S=3 см^2 плотность фототока составила 0,00035 А/см^2; 0,00028 А/см^2; 0,00013 А/см^2, соответственно. Было установлено, что при отсутствии нанокомпозитной пленки деградация красителя незначительна. При погружении в раствор красителя пленки TNR/Ag/rGO деградация красителя возросла и составила для S=1 см^2; S=1,5 см^2; S=2 см^2; S=3 см^2 32, 59, 70 и 81 % при длительности облучения 240 мин. Полученые результаты позволили предположить, что с ростом активной площади поверхности пленок их фотокаталитическая активность уменьшается. Снижение фотокаталитической активности связано с поверхностными дефектами и ростом сопротивления пленок.

Ключевые слова: наностержни диоксида титана, наночастицы серебра, восстановленный оксид графена, площадь пленки, фотокатализ.

DOI 10.31489/2023PH4/14-22

UDC 535.215; 535.3

S.K. Tazhibayev, M.K. Beisembekov, X.S. Rozhkova, A.M. Zhakanova, A.K. Aimukhanov, A.T. Makhabayeva, A.K. Zeinidenov*.

Karaganda Buketov University, Scientific Center for Nanotechnology and nanomaterials, Karaganda, Kazakhstan
**Corresponding authors e-mail: a.k.zeinidenov@gmail.com*

Impact of the thickness of phthalocyanine films and its metal complexes on optical and electrical properties

The paper presents the results of a study of the structural, optical and electrophysical characteristics of phthalocyanine films and its metal complexes with different thicknesses. Films of phthalocyanine and its metal complexes were obtained on the conductive surface of the FTO by thermal evaporation in vacuum. It is shown that the observed broadening of the B and Q bands and the hypsochromic shift of the maxima in the absorption spectra are associated with the central atom. With a decrease in the thickness of MPc films, there is a decrease in the value of the half-width of the absorption spectra. The effect of the thickness of phthalocyanine films on the efficiency of generation and transport of charge carriers in the FTO/MPc/Al cell was studied. It is shown that the VAC increases almost 2.5 times compared to a photocell based on a metal-free phthalocyanine. From the obtained impedance measurement data, it was found that the electrophysical parameters of phthalocyanines depend on the values of optical density, broadening of absorption bands in the short-wave and visible spectral regions, which is consistent with the data of the volt-ampere characteristic.

Keywords: phthalocyanine, metal phthalocyanines, solid films, absorption spectra, impedance meter, current-voltage characteristics.

Introduction

Phthalocyanines are currently widely studied molecular semiconductors, which is due to both applied and scientific reasons. Phthalocyanines are large aromatic organic compounds constructed from four isoindole units connected by nitrogen atoms. Phthalocyanines are chemically and thermally stable, most of them are organic p-type semiconductors and have photoconductivity, easily forming ordered thin films [1, 2]. This determines their use as media for optical recording of information, for the manufacture of light-emitting diodes (LEDs), solar cells, gas sensors, high-speed magnetic field sensors [3-5].

In recent years, there has been great interest in phthalocyanines with central atoms of various metals (metallophthalocyanines ― MPCs). Groups of metal phthalocyanines are formed as a result of the introduction of divalent metal atoms (e.g. Zn, Cu, Co and Ni) into the phthalocyanine ring. The physical and chemical properties of MPCs are well regulated by optimizing the central metal ions and their structure [6]. Also, the correct choice of morphology and polymorphism of the MPCs thin film structure can have a significant impact on its optical and electrical properties [7].

Due to the remarkable electronic and optical properties, MPCs thin films have become a promising material for organic electronic devices [8, 9]. For example, in recent years MPCs have been implemented in perovskite solar cells as hole transfer materials (HTM), achieving in some cases efficiency exceeding 20 % [10-11]. MPCs are also attractive building blocks in molecular donor-acceptor (D-A) systems due to their ability to efficiently absorb light in the visible region, as well as their ability to act as electron (D) donors during photoexcitation in various D-A systems [12, 13].

Thus, phthalocyanine and its metal complexes have a wide range of potential applications in electronics, energy, chemistry and medicine. Research in this area is ongoing, and it may lead to new and innovative applications of these materials.

In this work, films of phthalocyanine and its metal complexes with different thicknesses were obtained by thermal spraying in vacuum. We studied the effect of film thickness on structural, optical and electrical properties, as well as conducted a detailed analysis of charge transfer processes in phthalocyanine films.

Materials and Methods

Preparation of a solid substrate

An important step in the process of applying films is cleaning the surface of FTO glass substrates. Cleaning of the substrate surface from contamination was carried out using lint-free wipes soaked in isopropyl alcohol. After that, the cleaning process was carried out, consisting of three stages. At the first stage, the holder with glass substrates FTO was placed in a beaker with an ammonia peroxide solution, which consists of 50 ml of a 3% solution of hydrogen peroxide (H_2O_2), 15 ml of a solution of aqueous ammonia (NH_3 + NH_4OH + H_2O) and 135 ml of distilled water. A glass of solution with substrates was heated in a water bath at a temperature of 90-95° C for 15-20 minutes. Then, the holder with glass FTO substrates was washed with distilled water, after which it was purged with a stream of compressed nitrogen (N_2) and dried in a drying cabinet. The second stage was the sequential cleaning of the substrate surfaces in an ultrasonic bath, first with acetone, then with isopropanol for 10-15 minutes with an intermediate purge with a stream of compressed nitrogen in order to completely dry the solvents. The final stage is a 50-60 minutes process of exposure to ultraviolet radiation (with wavelengths of 185 and 254 nm, with an intensity of 20μV / cm^2) on the surface of the substrates, which was carried out at the UV Ozone Cleaner unit manufactured by Ossila.

Production of thin films

The production of films of phthalocyanine and its metal complexes on a solid surface was carried out by thermal evaporation in a vacuum of 10^{-3} Pa. A ceramic crucible was used as an evaporator. Different film thicknesses were obtained by changing the distance of the holder from the evaporator, which was 80, 100, 120 mm. After that, an Al electrode was sprayed onto the surface of the films at a vacuum of 10^{-3} Pa. The thickness and deposition rate of the metal were measured using a piezoelectric quartz resonator. To obtain films of phthalocyanine and its metal complexes, reagents of analytical purity (Sigma-Aldrich) were used, the structural formula is shown in Figure 1.

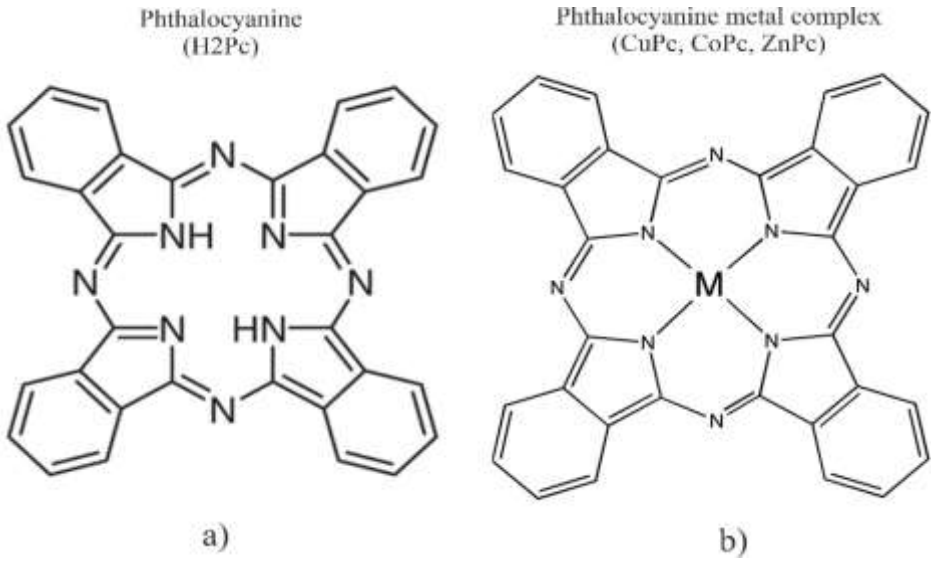

Figure 1. Structural formulas phthalocyanine (a) and its metal complexes (b)

Analysis methods

The surface topography and thickness of the samples were probed by a MIRA 3 LMU (SEM, Tescan). The absorption spectra of the samples were measured by an AvaSpec-ULS2048CL-EVO spectrometer (Avantes). A combined deuterium-halogen light source AvaLight-DHc (Avantes) with an optical range of 200–2500 nm was used as a light source. For thermal deposition, the CY-1700x-spc-2 vacuum sputtering unit (Zhengzhou CY Scientific Instruments Co., Ltd) was used.

The impedance spectra were measured by a P45X potentiostat-galvanostat with an FRA module. Current-voltage (C-V) characteristics of solar devices were measured with PVIV-1A I-V Test Station under the light illumination from Sol3A Class AAA Solar Simulator (Newport).

Results and Discussion

Structural analysis of the prepared films

Figure 2 shows SEM images of the surface and transverse cleavage of phthalocyanine films and its metal complexes. As can be seen from the figure, the morphology of the film surface depends on the thickness of the sample deposition. For a film of nonmetal phthalocyanine (H2Pc) and zinc phthalocyanine (ZnPc), a continuous fine-grained surface is observed, with a decrease in the thickness of the film, the surface becomes more homogeneous. Cobalt phthalocyanine (CoPc) and copper phthalocyanine (CuPc) films have a coarser-grained structure, with a decrease in film thickness, a smooth and fine-grained surface is observed. All MPc films were obtained by vacuum spraying under the same conditions, and as a result, the thickness of the vacuum-deposited films is approximately the same.

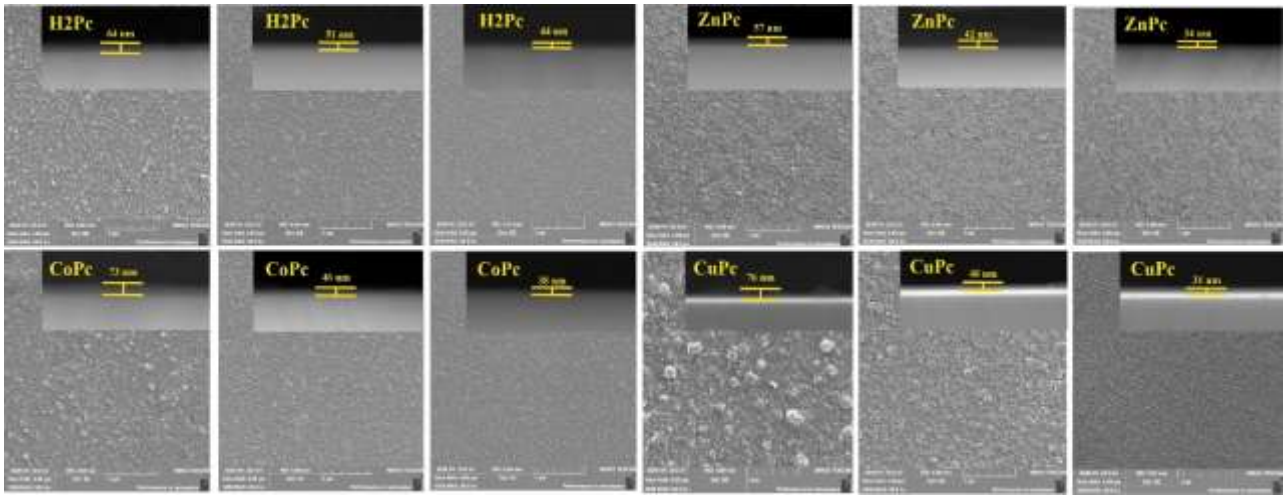

Figure2. SEM images of phthalocyanine films and its metal complexes with different thicknesses.

Optical properties

Figure 3 shows the absorption spectra of vacuum-deposited MPc films. There are two intense bands in the absorption spectra: in the region of 300-450 nm (B-band), which correspond to the mixed π-π* and n-π transitions a2u→2eg and b2u→2eg, and the absorption band in the region of 550-700 nm (Q-band), which corresponds to the π-π* transition a1u→2eg [14-15]. As can be seen from the figure, the absorption band of H2Pc, ZnPc and CoPc films in the B-band region has a maximum at a wavelength of λ = 340 nm. In the Q-band, two maxima are also observed at wavelengths λ =630 nm and λ =690 nm. In turn, for CuPc films, a hypsochromic shift of absorption maxima λ = 227 nm is observed in the B-band region, as well as a shift of maxima in the Q-range λ =485 nm and λ = 553 nm. With a decrease in the thickness of MPc films, there is a decrease in the value of the half-width of the absorption spectra. This is due to the fact that a decrease in the thickness of the films leads to a decrease in the local environment of the absorption center, through which energy is absorbed. A decrease in the local environment of the center in the films leads to a greater probability of photon scattering and, as a result, to a decrease in the half-width of the absorption spectra. Table 1 shows the characteristics of the absorption spectra of the B and Q ranges of MPc films.

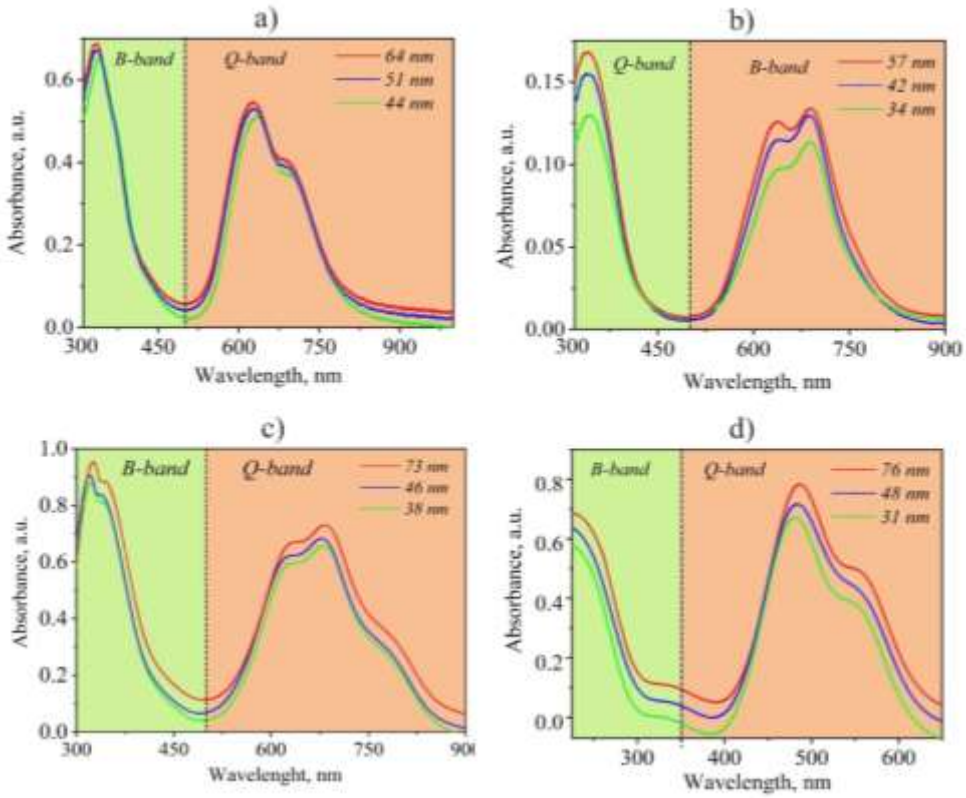

Figure 3. Absorption spectra of H2Pc(a), ZnPc (b), CoPc (c)and CuPc (d) films with different thicknesses.

Table 1

Characteristics of the absorption spectra of the B and Q ranges.

Film, thickness	B-band			Q-band		
	λ_{max}, nm	D (optical density)	FWHM, nm	λ_{max}, nm	D (optical density)	FWHM, nm
H2Pc -64nm	λ=333	D=0.68	110	λ_1=627 λ_2=694	D_1=0.55 D_2=0.41	138
H2Pc -51nm	λ=336	D=0.67	108	λ_1=628 λ_2=692	D_1=0.53 D_2=0.39	114
H2Pc -44nm	λ=340	D=0.65	98	λ_1=632 λ_2=694	D_1=0.51 D_2=0.37	96
ZnPc -57nm	λ=339	D=0.17	94	λ_1=636 λ_2=688	D_1=0.12 D_2=0.13	141
ZnPc -42nm	λ=339	D=0.16	83	λ_1=638 λ_2=685	D_1=0.11 D_2=0.12	130
ZnPc -34nm	λ=344	D=0.13	80	λ_1=638 λ_2=688	D_1=0.09 D_2=0.11	117
CoPc -73nm	λ_1=325 λ_2=348	D_1=0.97 D_2=0.88	99	λ_1=630 λ_2=682	D_1=0.68 D_2=0.72	148
CoPc -46nm	λ_1=320 λ_2=341	D_1=0.90 D_2=0.85	91	λ_1=623 λ_2=678	D_1=0.62 D_2=0.69	126
CoPc -38nm	λ_1=323 λ_2=345	D_1=0.87 D_2=0.82	89	λ_1=627 λ_2=680	D_1=0.59 D_2=0.64	108
CuPc -76nm	λ=227	D=0.69	110	λ_1=485 λ_2=553	D_1=0.79 D_2=0.52	156
CuPc -48nm	λ=227	D=0.62	96	λ_1=482 λ_2=558	D_1=0.71 D_2=0.48	128
CuPc -31nm	λ=227	D=0.58	83	λ_1=476 λ_2=544	D_1=0.67 D_2=0.39	102

Along the edge of the absorption spectra, the width of the optical band gap B and Q of the MPc films was estimated (Fig. 4a, b). The estimation of the width of the optical band gap of MPc films was carried out by the TaucPlot method. As can be seen from Figure 4a, the width of the band gap in the B-band was for H2Pc films: Up=3.10, ZnPc: Up=2.94, CoPc: Up=2.99, CuPc: Up=3.25. The width of the optical band gap in the Y-band showed values for H2Pc films: Up=1.62, ZnPc: Up=1.66, CoPc: Up=1.62, CuPc: Up=1.65 (Fig. 4b).

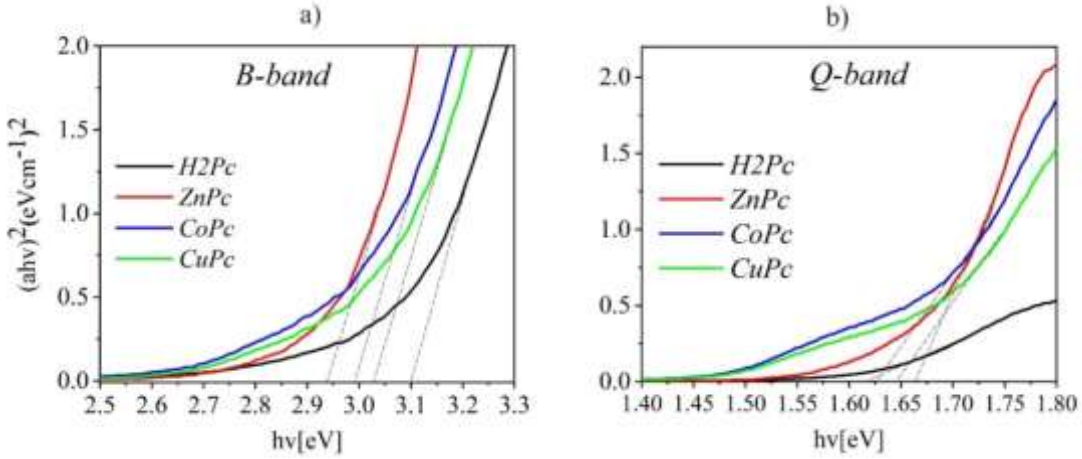

Figure 4. The width of the optical band gap B (a) and Q(b) ranges of phthalocyanine films and its metal complexes

Photoelectrical characterizations

Photovoltaic cell samples consisting of a glass substrate, a transparent conductive layer of polycrystalline FTO (anode), a photoactive MPc layer and an aluminum electrode were prepared for photovoltaic measurements (Fig. 5a). Figure 5b shows a diagram of MPc energy levels. It can be seen from the diagram of energy levels that the values of the band gap width and the position of the energy levels of HOMO and LUMO phthalocyanines differ slightly. The width of the forbidden zone varies in the range from 1.6 to 1.9 eV. The shift of the energy levels of HOMO and LUMO in phthalocyanines depends on the central metal atom.

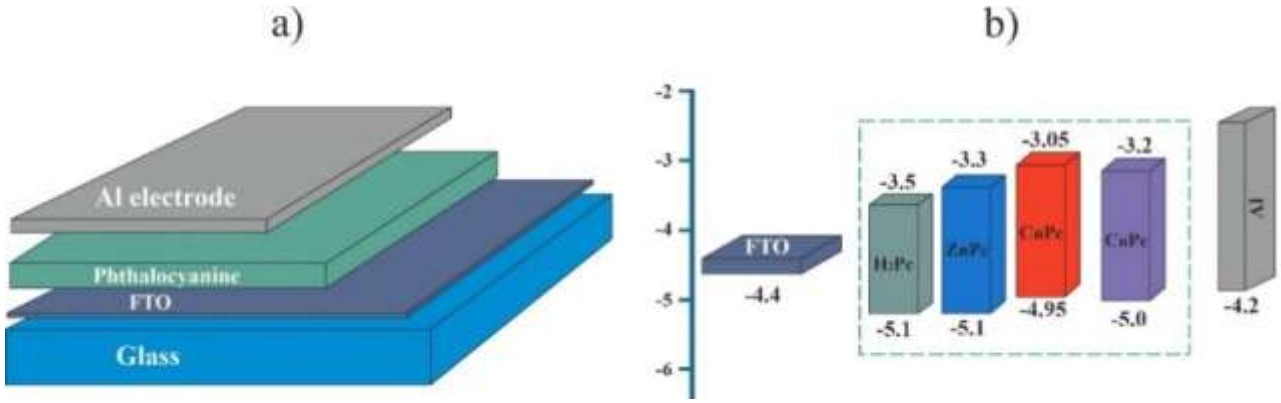

Figure 5. Photovoltaic cell structure (a) and diagram energy levels (b)

Figure 6 shows MPc current-voltage characteristics with different thicknesses. As can be seen from the figure, the current-voltage characteristics are nonlinear. The photosensitive cell based on H2Pc has the lowest values of electrical characteristics. The efficiency of charge carrier generation in a solid H2Pc film is low due to the weak broadening of the absorption bands in the B- and Q-bands (Fig. 3a). This is indicated by the low value of the short-circuit current density J_{sc} = 3.7 mA/cm^2. The maximum no-load voltage V_{oc} = 0.48 V has been achieved for films with a thickness of 51 nm. The ZnPc-based photocell has improved characteristics, such as the short-circuit current density J_{sc} =12.3 mA/cm^2 and the maximum value of the no-load voltage V_{oc} = 0.90 V. These values were obtained for films with a thickness of 34 nm. For CoPc films, the current density value J_{sc} = 9.2 mA/cm^2 and the maximum voltage V_{oc} = 1.26 V were obtained for films with a thickness of 73 nm. The current-voltage characteristics of CuPc-based cells showed a value of J_{sc}

=8.2 mA/cm^2, while the maximum voltage value at a film thickness of 48 nm is V_{oc} = 0.90 V. This fact is due to an increase in the optical density and a broadening of the absorption bands in the short-wave and visible spectral regions. The analysis of the current-voltage characteristics in the figures shows that the values of J_{max} and J_{sc} cells based on phthalocyanine with a central metal atom increase by almost 2.5 times, compared to a photocell based on nonmetal phthalocyanine, while the dependence of J_{sc} on the thickness of films in all MPCs does not change. However, there is a dependence of V_{oc} on the thickness of MPc films (Table 2).

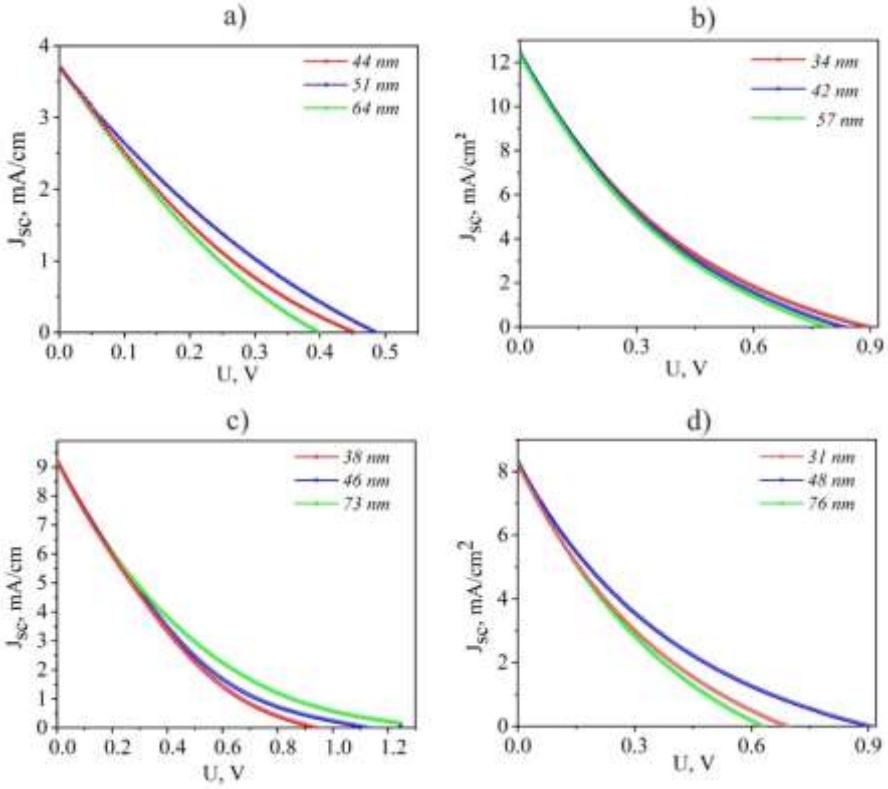

Figure 6. Current-voltage characteristics of H2Pc(a), ZnPc (b), CoPc (C)and CuPc (d) with different thicknesses

Table 2

Photovoltaic characteristics of phthalocyanine and its metal complexes

Film, thickness	V_{oc}(V)	J_{sc}(mA/cm^2)	V_{max} (V)	J_{max}(mA/cm^2)	FF
H2Pc -64 nm	0.39	3.7	0.20	1.3	0.15
H2Pc -51 nm	0.48	3.7	0.23	1.5	0.19
H2Pc -44 nm	0.45	3.7	0.21	1.4	0.19
ZnPc -57 nm	0.78	12.3	0.32	4.6	0.15
ZnPc -42 nm	0.83	12.3	0.33	4.7	0.16
ZnPc -34 nm	0.90	12.3	0.34	4.8	0.14
CoPc -73nm	1.26	9.2	0.44	3.1	0.11
CoPc -46 nm	1.11	9.2	0.42	3.2	0.13
CoPc -38 nm	0.94	9.2	0.41	3.4	0.16
CuPc -76 nm	0.69	8.2	0.30	3.2	0.16
CuPc -48 nm	0.90	8.2	0.33	2.9	0.13
CuPc -31nm	0.62	8.2	0.29	2.8	0.14

Figure 7 shows the impedance spectra of cells of the FTO/MPc/Al structure with different thickness of the MPc layer. As can be seen from the figure, the cell based on H2Pc has the highest values of electrophysical characteristics. The resistance of the H2Pc film with a layer thickness of 64 nm is 5697.8 ohms, the recombination resistance is 1.57-105 ohms. When the layer thickness decreases to 51 nm, a decrease in the resistance value is observed, and at a thickness of 44 nm, the film has minimal electrophysical characteristics for this type of phthalocyanine, R_w =4389.3 ohms, R_{rec}=1.39-105 ohms. The conditional mobility of charge

carriers increases with a decrease in the thickness of H2Pc. The data of the impedance spectra are consistent with the data of the current-voltage characteristics and the characteristics of the optical absorption spectrum. For CoPc films, a device with a layer thickness of 46 nm has optimal characteristics. R_{rec} = 1.34-106 ohms, R_w = 368.6 ohms. For a 76 nm thick CuPc film, the resistance parameters are equal to R_{rec} = 0.42 -105 ohms and R_w = 4012.7 ohms. However, the ZnPc-based device has the best characteristics. For a ZnPc film with a thickness of 34 nm, the minimum resistance value R_w = 173.4 ohms has been achieved, at this thickness the recombination resistance is 1.37-106 ohms, the effective lifetime of charge carriers is 81 ms and is the highest among all the studied samples, D_{eff} is 34.2 10^{-8} cm^2 $/s^{-1}$, and the conditional mobility of charge carriers it is maximum and equal to 1.4-$10^5 cm^2V^{-1},s^{-1}$. The dynamics of changes in electrophysical parameters is caused by changes in the values of optical density, broadening of absorption bands in the short-wave and visible spectral regions and is consistent with the data of the current-voltage characteristics (Table 3).

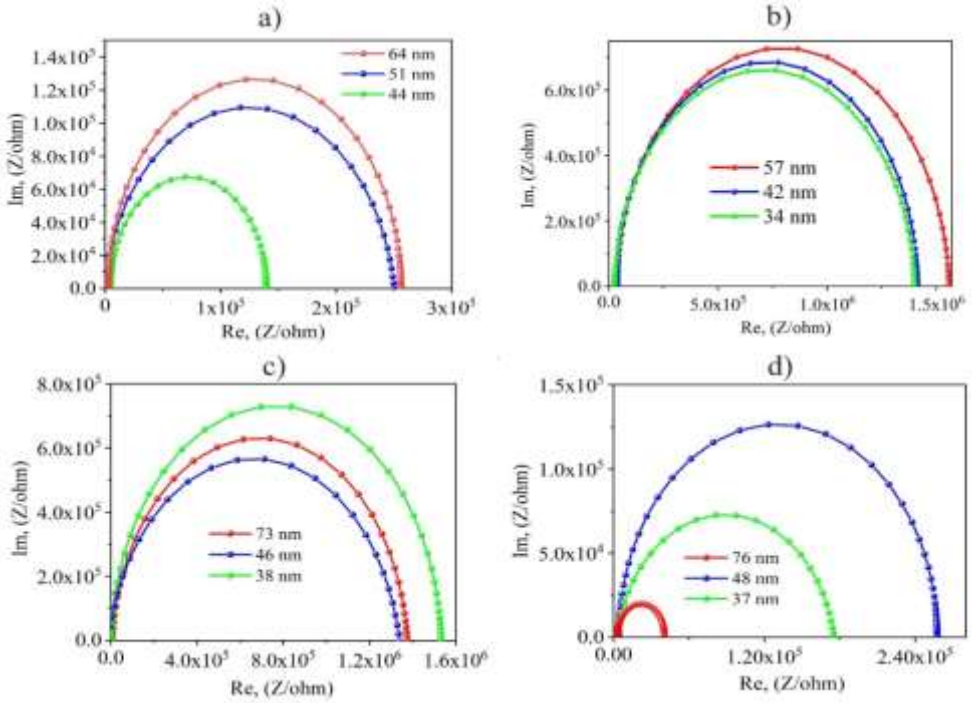

Figure 7. Impedance hodographs in Nyquist coordinates for sprayed films H2Pc (a), ZnPc (b), CoPc (c) and CuPc (d) with different thicknesses

Table 3

Charge transfer parameters of phthalocyanine films and its metal complexes with different layer thicknesses

Film, thickness	D_{eff}, ($sm^2 \cdot s^{-1}$)	k_{eff}, (s^{-1})	τ_{eff}, (ms)	R_{rec}, (ohm)	R_w, (ohm)	μ, (cm^2V^{-1} ,s^{-1})
H_2Pc -64 nm	$28.7 \cdot 10^{-5}$	25.5	39	$1.57 \cdot 10^5$	5697.8	$0.1 \cdot 10^{-5}$
H_2Pc -51 nm	$20.9 \cdot 10^{-5}$	26.4	37	$1.46 \cdot 10^5$	4789.7	$0.9 \cdot 10^{-5}$
H_2Pc -44 nm	$17.2 \cdot 10^{-5}$	28.1	35	$1.39 \cdot 10^5$	4389.3	$0.7 \cdot 10^{-5}$
ZnPc -57 nm	$23.8 \cdot 10^{-7}$	15.5	64	$1.5 \cdot 10^6$	316.3	$1.3 \cdot 10^{-5}$
ZnPc -42 nm	$17.5 \cdot 10^{-7}$	14.2	70	$1.42 \cdot 10^6$	203.2	$1.1 \cdot 10^{-5}$
ZnPc -34 nm	34.210^{-8}	12.3	81	$1.37 \cdot 10^6$	173.4	$1.4 \cdot 10^{-5}$
CoPc -73nm	$29.7 \cdot 10^{-7}$	15.3	65	$1.38 \cdot 10^6$	378.1	$0.2 \cdot 10^{-5}$
CoPc -46 nm	$10.5 \cdot 10^{-7}$	13.7	72	$1.34 \cdot 10^6$	368.6	$0.8 \cdot 10^{-5}$
CoPc -38 nm	$79 \cdot 10^{-6}$	13.3	75	$1.52 \cdot 10^6$	370.1	$0.5 \cdot 10^{-5}$
CuPc -76 nm	$15.5\ 10^{-5}$	25.7	38	$0.42 \cdot 10^5$	4012.7	$0.2 \cdot 10^{-5}$
CuPc -48 nm	$21.1 \cdot 10^{-5}$	17.5	57	$2.11 \cdot 10^5$	4025.7	$0.1 \cdot 10^{-5}$
CuPc -37 nm	$2.5 \cdot 10^{-5}$	4.3	23	$1.73 \cdot 10^5$	4063.7	$0.6 \cdot 10^{-5}$

Conclusions

As a result of vacuum spraying under the same conditions, MPc films were obtained, the SEM image of the transverse cleavage of the films showed that the thickness of the vacuum-deposited films is approximately the same. The measured absorption spectra showed that the maximum of the B-band for H2Pc, ZnPc and CoPc films is located at a wavelength of λ = 340 nm. In the Q-band, two maxima are observed at wavelengths λ = 630 nm and λ = 690 nm. For CuPc films, a hypsochromic shift of absorption maxima λ = 227 nm is observed in the B-band region, as well as a shift of maxima in the Q-range λ=485 nm and λ = 553 nm. Based on the results obtained, it was found that the value of the half-width of the absorption spectra decreases with a decrease in the thickness of MPc films. Along the edge of the absorption spectra, the width of the optical band gap of the B and Q ranges of MPc films is determined. The photovoltaic properties of FTO/MPc/Al cells with different MPc thicknesses were measured. The measured of the current-voltage shows that the values of J_{max} and J_{sc} cells with metal phthalocyanine increase almost 2.5 times compared to the H2Pc-based photocell, while the dependence of Jsc on the thickness of films in all MPCs does not change, however, there is a dependence of V_{oc} on the thickness of MPc films. The ZnPc-based photocell is characterized by improved characteristics of the short-circuit current density J_{sc} = 12.3 mA/cm^2 and the maximum no-load voltage V_{oc} = 0.90 V, which are obtained for films with a thickness of 34 nm. The measurement of the impedance spectra of the cells confirms that the effective lifetime of the charge carriers for the ZnPc film was 81 ms and is the highest indicator among all the samples studied. The dynamics of the electrophysical parameters for all MPc films is due to changes in the optical density values, broadening of the absorption bands in the short-wave and visible spectral regions and is consistent with the data of the current-voltage characteristic.

Acknowledgments

This research is funded by the Science Committee of the Ministry of Science and Higher Education of the Republic of Kazakhstan (Grant No. AP19576784).

References

1 Yang, Y.J., Li, S.X., Chen, D.L., & Long, Z.W. (2022). Geometric structure, electronic, and spectral properties of metal-free phthalocyanine under the external electric fields. *ACS Omega*, 7, 41266. https://doi.org/10.1021/acsomega.2c04941.

2 El-Saady, A.A., Roushdy, N., Farag, A.A.M., El-Nahass, M.M., & Abdel Basset, D.M. (2023). Exploring the molecular spectroscopic and electronic characterization of nanocrystalline metal-free phthalo-cyanine: a DFT investigation. *Opt. Quantum Electron*, 55, 662. https://doi.org/10.1007/s11082-023-04877-8.

3 El-Saady, A.A., Roushdy, N., Farag, A.A.M. & Ashour, A.H. (2023). Influence of Gamma-irradiation on the Structural, Morphological, and Optical Properties of β-H2Pc Nanocrystalline Films: Implications for Optoelectronic Applications. *Journal of Electronic Materials.* https://doi.org/10.1007/s11664-023-10703-4.

4 Zavgorodniy, A.V., Aimukhanov, A.K., Zeinidenov, A.K., & Akhatova, Z.Z. (2019). Study of the effect of an external magnetic field on the photoelectric properties of a copper phthalocyanine film. *Eurasian Physical Technical Journal, 16, 2*(32). http://rep.ksu.kz//handle/data/5802.

5 Rosemary, R., Cranstonaand Lessard, & Benoît, H. (2021). Metal phthalocyanines: thin-film formation, microstructure, and physical properties. *RSC Advances, 11*(35), 21716–21737. https://doi.org/10.1039/D1RA03853B.

6 Sridevi, B.R., Hoskeri, Priya, A. & Joseph, C.M. (2021). Effect of annealing on the optical, structural and electrochromic properties of vacuum evaporated manganese phthalocyanine thin films. *Thin Solid Films. 723, 138584.* https://doi.org/10.1016/j.tsf.2021.138584.

7 Gorduk, S., & Altindal, A. (2019). Peripherally tetra-substituted metallophthalocyanines bearing carboxylic acid groups for efficient dyesensitized solar cells. *J. Mol. Struct.*, 1196, 747–753. https://doi.org/10.1016/j.molstruc.2019.07.027.

8 Sukhikh, A., Bonegardt, D., Klyamer D., Krasnov, P., & Basova, T. (2020). Chlorosubstituted Copper phthalocyanines: Spectral study andstructure of thin films. *Molecules*, 1620. https://doi.org/10.3390/molecules25071620.

9 Reddy, G., Devulapally, K., Islavath, N., & Giribabu, L. (2019). Metallated macrocyclic derivatives as a hole — Transporting materials forperovskite solar cells. *Chem Rec.*, 19, 2157–2177. https://doi.org/10.1002/tcr.201800171.

10 Urbani, M., Torre, Gema de la., Nazeeruddin, M.K. & Torres, T. (2019). Phthalocyanines and porphyrinoid analogues as hole- and electron-transporting materials for perovskite solar cells. *Chem. Soc. Rev.*, 48, 2738–2766. https://doi.org/10.1039/C9CS00059C.

11 Yu, Z., Hagfeldt, A., & Sun, L. (2020). The application of transition metal complexes in hole-transporting layers for perovskite solar cells: Recent progress and future perspectives. Coord. *Chem. Rev.*, 406, 213143. https://doi.org/10.1016/j.ccr.2019.213143

12 Mack, J., & Kobayashi, N. (2011). Low symmetry phthlocyanines and their analogues. *Chem. Rev.*, 111, 281–321. https://doi.org/10.1021/cr9003049.

13 Martínez-Díaz, M.V., Ince, M., & Torres, T. (2011). Phthalocyanines: Colorful macroheterocyclic sensitizers for dye-sensitized solar cells. *Monatsh. Chem.*, 142, 699–707. https://doi.org/10.1007/s00706-010-0431-0.

14 Liao M.S., & Scheiner S. (2001). Electronic structure and bonding in metal phthalocyanines, metal=Fe, Co, Ni, Cu, Zn, Mg.*J. Chem. Phys.* doi.org/ 10.1063/1.1367374.

15 Guo, T., Zou, P.S., Song, Y., Mu, M., Xiao, F., Zhang, J., Wu, W., & Wang, H. (2020). A new polymorph of zinc-phthalocyanine and its optical properties. *Journal of Crystal Growth*, 546, 125760. https://doi.org/10.1016/j.jcrysgro.2020.125760

С.К. Тажибаев, М.К. Бейсембеков, К.С. Рожкова, А.М. Жақанова,
А.К. Аймуханов, А.Т. Махабаева, А.К. Зейниденов

Фталоцианин мен оның металл кешендері қабыршақтары қалыңдығының оның оптикалық және электрлік қасиеттеріне әсері

Мақалада әртүрлі қалыңдықтағы фталоцианин және оның металл кешендері қабықшаларының құрылымдық, оптикалық және электрфизикалық сипаттамаларының зерттеу нәтижелері ұсынылған. Вакуумда термиялық булану арқылы өткізгіш FTO бетінде фталоцианин және оның металл кешендерінің қабықшасы алынды. B және Q жолақтарында байқалатын кеңею және жұтылу спектрінің максимумдарының гипохромдық ығысуы орталық атоммен байланысты екені көрсетілген. MPc қабықшаларының қалыңдығы азайған сайын жұтылу спектрінің жарты ені азаяды. FTO/MPc/Al ұяшығында фталоцианин қабықшаларының қалыңдығы заряд тасымалдаушылар генерациясының және тасымалдануының тиімділігіне әсері зерттелді. Металсыз фталоцианин негізіндегі фотоэлементпен салыстырғанда ток кернеуінің сипаттамасы шамамен 2,5 есе өсетіні көрсетілген. Алынған импеданс нәтижелерінен фталоцианиндердің электрфизикалық параметрлері, оптикалық тығыздық мәндері мен спектрдің қысқа толқынды және көрінетін аймақтарындағы жұтылу жолақтарының кеңеюіне байланысты екені анықталды, бұл вольт-амперлік сипаттамасына талдау деректерімен сәйкес келеді.

Кілт сөздер: фтолацианин, металдар фтолацианині, қатты қабықшалар, жұтылу спектрлері, импедансметр, вольт-амперлік сипаттамалар.

С.К. Тажибаев, М.К. Бейсембеков, К.С. Рожкова, А.М. Жаканова, А.К. Аймуханов,
А.Т. Махабаева, А.К. Зейниденов

Влияние толщины пленок фталоцианина и его металлокомплексов на оптические и электрические свойства

В статье представлены результаты исследования структурных, оптических и электрофизических характеристик пленок фталоцианина и его металлокомплексов различной толщины. На проводящей поверхности FTO методом термического испарения в вакууме были получены пленки фталоцианина и его металлокомплексов. Показано, что наблюдаемое уширение полос B и Q и гипсохромный сдвиг максимумов спектра поглощения связаны с центральным атомом. С уменьшением толщины пленок MPc происходит снижение значения полуширины спектра поглощения. Изучено влияние толщины пленок фталоцианина на эффективность генерации и транспорта носителей заряда в ячейке FTO/MPc/Al. Показано, что ВАХ увеличивается почти в 2,5 раза по сравнению с фотоэлементом на основе безметаллового фталоцианина. Из полученных данных измерения импеданса установлено, что электрофизические параметры фталоцианинов зависят от значений оптической плотности, уширения полос поглощения в коротковолновой и видимой области спектра, что согласуется с данными анализа вольт-амперной характеристики.

Ключевые слова: фталоцианин, фталоцианины металлов, твердые пленки, спектры поглощения, импедансметр, вольт-амперные характеристики.

DOI 10.31489/2023PH4/23-37

UDC 528.563

E.N. Bezvesilnaya[1], Y.V. Kyrychuk[2], M.S. Hrynevych[3], T.A. Tolochko[4]

[1,2,4] National Technical University of Ukraine "Igor Sikorsky Kyiv Polytechnic Institute", Kyiv, Ukraine;
[3] State University "Zhytomyr Polytechnic", Zhytomyr, Ukraine
[1]o.bezvesilna@gmail.com, [2]y.kyrychuk@kpi.ua, [3]kakit_gms@ztu.edu.ua, [4]prilad168@gmail.com
[*]Corresponding author's e-mail: [1]o.bezvesilna@gmail.com

Simulation of the influence of parameters of disturbing vibration accelerations on the operation of a new two-channel transformer gravimeter

A new two-channel transformer gravimeter of an automated aviation gravimetric system was considered, the accuracy of which is higher than gravimeters known today. Its design was described. The influence of the parameters of disturbing vibrational accelerations on the operation of a new two-channel transformer gravimeter was simulated. The influence of frequencies and amplitudes of perturbing accelerations for the most unfavorable resonant cases on the operation of a two-channel transformer gravimeter was studied using a computer. After all, today there are no scientific, theoretical and practical works devoted to researching the possibility and expediency of using a two-channel transformer gravimeter as an AGS gravimeter. The transformer gravimeter contains a sensitive element consisting of a magnetic circuit, a movable armature, a primary excitation winding and a secondary output winding having two identical sections. Two sections of the secondary winding are connected in series-opposite, and the movable armature is connected to the motor, which, with a certain period, lowers the armature down and lifts it up along the magnetic circuit, and the motor is controlled by a switching device connected to the control voltage source, and the output signal from the secondary output winding is fed to the input of the output signal calculator, where an output signal is generated that is proportional to twice the value of the gravitational acceleration. A transformer gravimeter is a means of measuring the vertical component of the gravitational acceleration vector from an aircraft and can be used in the field of geodesy, geophysics, in particular, in the formation of reference gravimetric grids in hard-to-reach areas of the globe, as well as in aircraft and rocket building. The transformer gravimeter is part of the aviation gravimetric system placed on the aircraft.

Keywords: two-channel transformer gravimeter, disturbing action, resonant modes, damping, gravitational acceleration.

Introduction

Today, the use of an aviation gravimetric system (AGS) for mineral exploration (geology, geophysics, geodesy), for the correction of inertial navigation systems (aircraft and rocket science), for locating moving objects in the waters of the seas and oceans (military area), etc. Gravimetric measurements are made on the surface of the Earth, on submarines, on surface vessels and on aircraft. Airborne measurements make it possible to obtain information on gravitational acceleration (GA) in hard-to-reach areas of the globe with a speed and efficiency much higher than ground-based measurements.

Ground-based gravimetric systems do not allow determining GA in hard-to-reach regions of the Earth; they are carried out extremely slowly. Traditional airborne gravimetry is characterized by somewhat outdated technology and an insufficient level of accuracy. Aviation gravimetry has undeniable advantages over land and sea gravimetry. This is both greater speed, and the ability to carry out measurements in hard-to-

reach areas of the Earth, higher productivity, and a fairly high measurement accuracy. It is possible to significantly improve the accuracy by using an aviation gravimetric system [1], the sensitive element of which is a new two-channel transformer gravimeter, the advantages of which over the known gravimeters are high accuracy, powerful output signal, linearity of the characteristic over a large range, etc.

Review of scientific literature on the research topic. The analysis of the literature has shown that a great contribution to the theory and practice of measuring transducers, which are the basis for the operation of gravimeters, is associated with the names of L. Bergman, G. Tiersten, A.A. Andreeva, V.V. Malova, N.A. Shulgi, V.V. Lavrinenko, S.I. Pugacheva, O.P. Kramarova, A.E. Kolesnikova, P.A. Gribovsky and others [1-10].

To date, there are several types of gravimeters for aviation gravimetric systems, which have both advantages and disadvantages. In [4], the elastic element and the moving mass are made in the form of an element made of a sapphire single crystal. The invention [5] improves accuracy by reducing zero drift, increasing the range of linearity, and improving the filtering of inertial noise. In the gravimeter [6], the sensitive element for determining the BC is made of silicon or glass. This provides the sensitive element with exceptional reliability, high accuracy and stability of readings with respect to time and temperature.

Leading technical universities in the USA, Japan, Germany and other countries of the world are developing new models of AGS gravimeters and improving their accuracy [11-14]. However, almost all known gravimeters simultaneously measure the useful signal GA and the noise signal of vertical acceleration [1, 9, 15], which is 10^3 times greater than the useful signal GA [1, 9]. They need long-term periodic calibration, tuning, filtering of the output signal [16], which greatly complicates the work. The existing latest developments relate to marine [17, 18] and land [19] measurement methods that are not used in aviation gravimetry.

In the last 20 years, mainly quartz heavily damped gravimeters, string gravimeters, and gyroscopic gravimeters have been used as aviation gravimeters [20–27]. A single-channel capacitive gravimeter (CG) is also known. It is the main sensitive element of automated AGS [28]. However, the single-channel CG does not provide for the elimination of errors caused by the influence of vertical acceleration, as well as instrumental errors.

It is known [29] that the capacitive method of mass displacement measurement provides high accuracy only when measured by its compensation method, in which the gap is kept constant. Provides an accuracy of 2 mGal, which is not sufficient for GA measurements.

In the invention [30], the elastic element and the moving mass are made in the form of an element made of a sapphire single crystal. This element has the shape of a polyhedral prism with two through side holes. However, the sensitivity of the gravimeter is limited mainly by aging processes and depends on the change in the elastic properties of the spring in the gravimeter with temperature.

The gravimeter [31] consists of a quartz sensitive system damped by a liquid. The invention improves accuracy by reducing zero drift and increasing the range of linearity. The disadvantages of this gravimeter is the complexity of the design, the lack of full compensation of the main interference – vertical inertial acceleration; the presence of a filter complicates the design and reduces its reliability.

According to analysts from Gartner, microelectromechanical systems make it possible to increase the sensitivity and accuracy of converters (sensors) at the crystal level at minimal cost. Capacitive, piezoelectric, tensoresistive, thermoresistive, Hall effect, photoelectric converters are mainly used. Capacitive MEMC accelerometers manufactured by AnalogDevices, Bosch, Delphi, Denso, Freescale, Kionix, SiliconDesigns, ST Microelectronics, VTI Technologies are leaders in the modern market [12]. However, the accuracy of their work and the stability of the characteristics are not high enough. They are unstable, depend on the influence of external electromagnetic fields, which are large on the aircraft.

Having studied and analyzed the literature and Internet data [20-31], we can conclude that the known gravimeters have the following main disadvantages: non-linearity of the initial characteristic; low measurement accuracy (2-8mGal); the need to use complex procedures for filtering the output signal of the AGS gravimeter using special filters; the presence of instrumental errors and errors from the action of vertical acceleration; low speed of information processing (processing of the results of gravimetric measurements is carried out on Earth for months) and others.

The proposed transformer gravimeter (TG) [7] has undeniable advantages over known gravimeters: it measures acceleration in both positive and negative directions. The TG can measure static accelerations and vibrations with high accuracy. The main part of the gravimeter is a symmetrical sensitive element (SE), which has two sensitive transformer converters [1]. This reduces tempera-

ture dependence, sensitivity to cross-accelerations and increases linearity. The influence of vertical acceleration is eliminated, as well as instrumental errors and errors from non-identical parameters of the two channels are eliminated. An increase in the power of the output signal of the TG is provided by feeding the output signals of two transformer converters to the adder, where the useful output signal GA is doubled.

Statement of the research problem. Today, there are no scientific-theoretical and practical works devoted to research of the possibility and expediency of using a two-channel transformer gravimeter as an AGS gravimeter, the advantages of which over known gravimeters are greater accuracy (due to the elimination of the effect of vertical acceleration, instrumental and other errors) and sensitivity, small weight and size characteristics , simplicity of design, and others [7]. Therefore, it is expedient to study the parameters and characteristics of this type of gravimeter.

The object of study of this article: the process of measuring the acceleration of gravity.

Subject of the article: two-channel transformer gravimeter.

The purpose of this article is to model and study the influence of the parameters of disturbing vibrational accelerations on the operation of a new two-channel transformer gravimeter (two-channel TG) of an automated aviation gravimetric system using a computer.

Objectives of the article: to present data on the design and principle of operation of a new two-channel transformer gravimeter; to investigate the stability of two-channel TG; to simulate the effect of disturbing vibrational accelerations on the operation of the two-channel TG; develop software and use it to investigate the influence of frequencies ω, amplitudes w_a, w_b of disturbing vibrational accelerations and damping coefficient for the most unfavorable resonant cases: $\omega = \omega_0$, $\omega = 2\omega_0$, $2\omega = \omega_0$; where ω_0 is the natural frequency of the two-channel TG; analyze the obtained simulation results.

Research methods and materials

Next, we present the main materials and research methods in accordance with the goals and objectives.

1. Stability studies of a system with a two-channel TG

When carrying out measurements, a transient process always occurs, in which the output signal of the measuring instrument changes significantly with time. This is explained by the inertial properties of the measuring instrument, which cause the appearance of a dynamic error [1, 8]. The system under study is nonlinear, like most systems in nature and technology. In [1, 9], the characteristic equation of the two-channel TG system was obtained:

$$D(p) = T^2 p^2 + 2 \cdot \xi \cdot T \cdot p + \left(1 + K_{TCTG}\right) = 100\, p^2 + 14\, p + (1 + 40). \quad (1)$$

With a stable two-channel TG system, under any real impact on it, the controlled value during the transient will not deviate from the set value indefinitely. There are many stability criteria, both analytical and graphical. The best known are the Nyquist and Hurwitz criteria. Let us define the stability of the system with two-channel TG according to these criteria. In accordance with the Hurwitz stability criterion, in order for the automatic control system to be stable, it is necessary and sufficient that all Hurwitz determinants have the same signs with the sign of the leading coefficient of the characteristic equation a_n, that is, when $a_{n-1} > 0$ they are positive [8].

Thus, a necessary and sufficient stability condition for a second-order system, which is equation (1), is the positivity of the coefficients of the characteristic equation. In our two-channel TG system, we observe the following:

$$\begin{gathered} a_0 = T^2 = 100 > 0, \\ a_1 = 2 \cdot \xi \cdot T = 14 > 0 \\ a_2 = 1 + K = 40 > 0. \end{gathered} \quad (2)$$

Thus, according to the Hurwitz stability criterion, the two-channel TG system (2) is stable.

Transfer function two-channel TG over the HA channel for the output voltage [8]:

$$W_{TG}(p) = \frac{K_{TG}}{T_1 p^2 + T_2 p + 1}, \quad (3)$$

where K_{TG} – static transmission factor two-channel TG, T_1 and T_2 – time constants of the object of the second order.

To study two-channel TG for stability, according to the Nyquist criterion, we use the two-channel TG transfer function (3):

$$W_{TCTG}(p)=\frac{40}{100p^2+14p+1}. \tag{4}$$

We substitute $p=j\omega$ into equation (4) and obtain the two-channel TG frequency transfer function:

$$W(j\omega)=\frac{40}{-100\omega^2+14j\omega+1}=\frac{40(1-100\omega^2+14j\omega)}{(1-100\omega^2)^2+j(-14\omega)^2}.=X(\omega)+jY(\omega), \tag{5}$$

where $X(\omega)$, $Y(\omega)$ – real and imaginary parts of the two-channel TG transmission frequency function, respectively.

We select from equation (5) the real and imaginary parts and find the point of intersection of the amplitude-phase characteristic (APC) real axis $X(\omega)$:

$$\begin{cases} X(\omega)=\dfrac{40(1-100\omega^2).}{(1-100\omega^2)^2+j(-14\omega)^2}; \\ Y(\omega)=\dfrac{40\cdot 14\omega}{(1-100\omega^2)^2+j(-14\omega)^2}; \end{cases} \tag{6}$$

$$X(0)=40.$$

Based on the calculated data (6), we construct the APC (Fig. 1) in the MatLab software environment (Nyquist hodograph).

In order for the two-channel TG system to be stable, it is necessary and sufficient that the Nyquist hodograph does not cover the point with coordinates (-1, j0). As we see from Figure 1, the point is not covered, therefore, the two-channel TG system is stable.

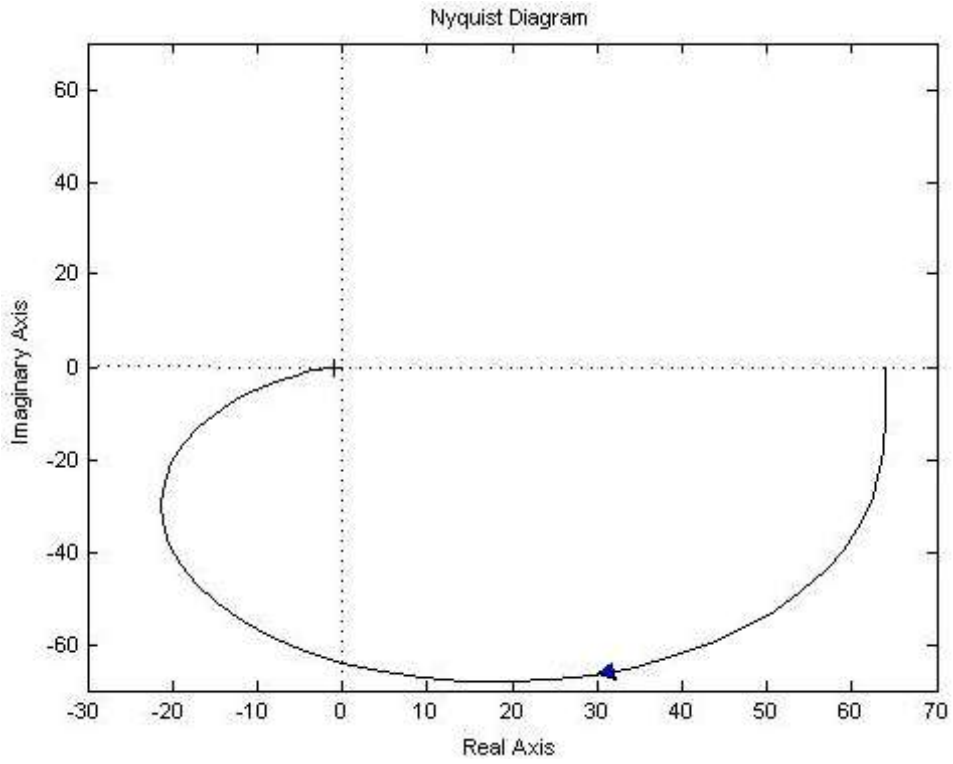

Figure 1. Amplitude-phase characteristic of two-channel TG

2. Design and principle of operation of the transformer gravimeter

The transformer gravimeter belongs to the means of measuring the vertical component of the HA vector on board the aircraft and can be used in the field of geodesy, geophysics, in particular, in the formation of reference gravimetric grids of hard-to-reach areas of the Earth, as well as in the aerospace area.

The closest analogue of two-channel TG is a solenoid-type *transformer converter* [1, 4] (Fig. 2).

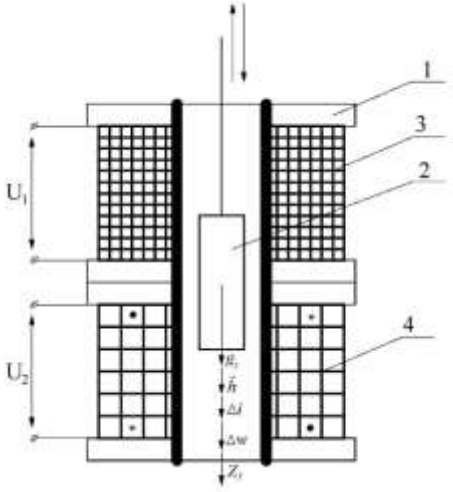

Figure 2. Transformer converter [1, 4]

The common essential features of a transformer converter (TC) and a transformer gravimeter (TG) is that they contain a sensitive element, which consists of a magnetic circuit 1, a movable armature 2, a primary excitation winding 3 and a secondary output winding 4, which has two identical sections.

However, unlike TG, TC has a number of disadvantages. Two sections of the secondary winding 4 W_2 in TC connected in series-accordingly (beginning-end of one section, beginning-end of another section). That is, the output winding 4 W_2 is solid (Fig. 2). Under the action of acceleration of the force of gravity g_z, which acts along the sensitivity axis of the transformer converter O_z, the force of gravity arises $G = mg_z$. Excitation winding 3 W_1 is connected to voltage U_1 and forms an electromagnetic flux of excitation Φ_1. According to the law of electromagnetic induction, this flux induces EMF E_2 in winding 4 W_2. Under the action of the acceleration of gravity, the anchor 2 moves down in the middle of the magnetic conductor 1 and causes a change in the electromagnetic flux Φ_1. Then the electromotive force E_2 in winding 4 W_2 will change in proportion to the acceleration of gravity $g_z: E_2 = mg_z$. The output electrical signal U_2 will be proportional to $g_z: U_2 = mg_z$. Under the action of an external electromagnetic flux of an obstacle (significant extraneous electromagnetic fluxes occur on moving objects: aircraft, surface and submarines), the EMF E_{Π} of the obstacle will be induced in the output winding 4 $W_2: E_2 = mg_Z + E_n$. Accordingly, the output signal will be $U_2 = mg_Z + U_n$. Instrumental errors from the influence of changes in temperature, humidity, pressure, moment of dry friction forces, etc. are significant for TC and are not compensated in any way. Vertical acceleration $\ddot{h}$, when installing TC on aircraft, will act along the axis of sensitivity of the converter, then: $E_2 = mg_Z + m\ddot{h}$. The value of the vertical acceleration $\ddot{h}$ is 10^3 times greater than the value of g_z, that is, the value of the error significantly exceeds the useful signal.

Thus, a significant drawback of the TC is its low accuracy in measuring gravitational acceleration.

3. New two-channel transformer gravimeter

The new transformer gravimeter is based on the task of increasing the accuracy of measuring gravitational acceleration. *Transformer gravimeter* contains a sensitive element, which consists of a magnetic circuit 1, a movable armature 2, a primary excitation winding 3 and a secondary output winding 4, which has two identical sections. To improve the accuracy of measuring the gravitational acceleration, two sections of

the secondary winding 4 are connected in series-opposite, the movable armature 2 is connected to the motor 5, which, with a certain period, sequentially lowers the armature 2 down and raises it up along the magnetic circuit 1, and the motor 5 is controlled by the switching device 6, which connected to the source 7 of the control voltage, and the output signal from the secondary output winding 4 is fed to the input of the device 8 for calculating the output signal, where an output signal is generated that is proportional to the double value of the gravitational acceleration (Fig. 3).

An increase in the accuracy of measuring gravitational acceleration in a new two-channel transformer gravimeter is provided as follows. Under the action of an external electromagnetic flow of an obstacle, this flow will induce two EMF obstacles in two sections W_2, which are included in series-opposite $E_{2П}$ and $-E'_{2П}$. In total, these errors are compensated. That is, such a counter connection of the sections provides compensation for errors from the influence of external electromagnetic flows, which can be significant when installing the gravimeter on a moving object. The action of instrumental errors from the influence of changes in temperature, humidity, pressure, moment of dry friction forces, etc. will be compensated in a similar way due to the counter connection of two sections W_2. Thus, the proposed transformer gravimeter provides a significant increase in the accuracy of measuring gravitational acceleration. *The essence of the operation of a two-channel transformer gravimeter (two-channel TG) is explained by the diagram in Figure 3.*

The sensitive element of the TG, as in the case of a transformer converter, consists of a magnetic circuit 1, a moving armature 2, a primary excitation winding 3 and a secondary output winding 4, which has two identical sections. Two sections of the secondary winding 4 are connected in series-opposite. The moving armature 2 is connected to the motor 5, which every second successively lowers the armature 2 down and up the magnetic circuit 1. The motor 5 is controlled by the switching device 6, which is connected to the source 7 of the control voltage. The output signal from the secondary output winding 4 is fed to the input of the device 8 for calculating the output signal, the output of which is a signal that is proportional to the double value of the gravitational acceleration and does not include errors from the influence of the vertical acceleration of the aircraft, residual instrumental errors, residual errors from the projections of horizontal cross accelerations and errors caused by the influence of external electromagnetic flows.

The new transformer gravimeter works as follows (Fig. 3).

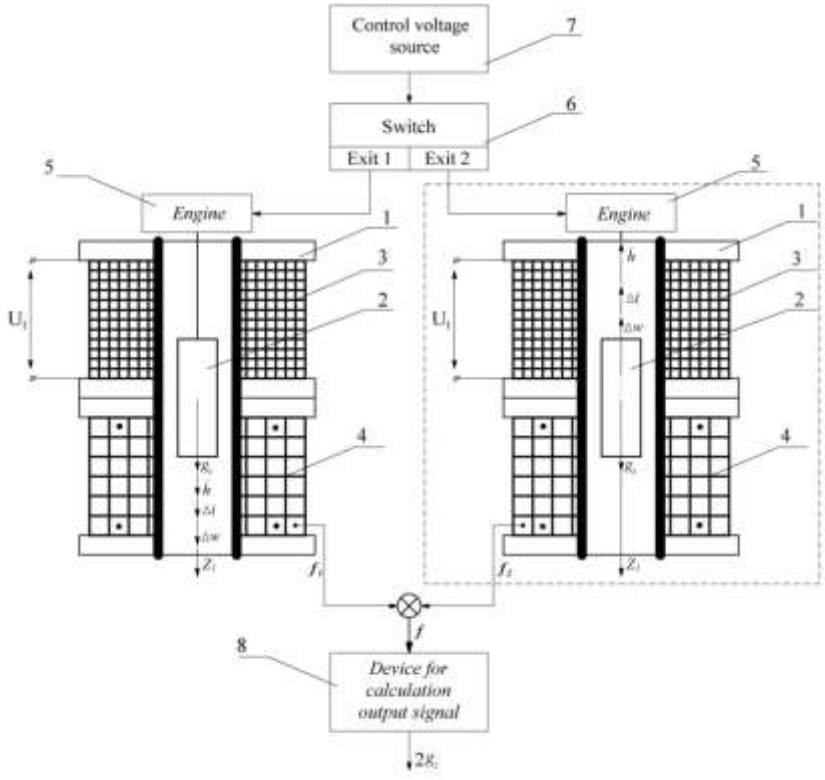

Figure 3. Block diagram of the new two-channel TG [7]

Under the influence of gravitational acceleration g_z, which acts along the sensitivity axis of the gravimeter O_z, there is a gravity force $G = mg_z$. The excitation winding W_1 is connected to the voltage source 7 U and creates an electromagnetic excitation flux Φ_1. According to the law of electromagnetic induction, this flux induces two EMFs E_2 and $-E'_2$ in two sections of the winding W_2. Under the influence of gravity, the anchor 2 moves down in the middle of the magnetic conductor 1 and causes a change in the electromagnetic flux Φ_1 and, respectively, E_2 and $-E'_2$. At the point of electromagnetic symmetry TG we will also receive $E_2 = |-E'_2|$ and the output signal $U_2 = 0$. When the anchor 2 is moved relative to the point of symmetry down (Fig. 3) or up (Fig. 3, circled with dashed lines) $E_2 \neq |-E'_2|$, the output signal of the gravimeter will be proportional $U_2 \equiv |E_2 - E'_2| \equiv mg_z$. In the new two-channel TG, a switch device (SD) 6 was additionally introduced, which is powered by a control voltage source 7, which, at regular intervals of 1 s, switches the supply of the vertical movement of the armature 2 down (Fig. 3) and up (Fig. 3, circled by a dotted line) through motor 5.

When a downward motion pulse is supplied from switch device 6 to armature 2, the output signal f_1 of the sensitive element is fed to the output signal calculation device 8. After 1 s., an upward movement pulse is applied to armature 2 and the output signal calculation device 8 receives a signal f_2. In the device for calculating the output signal 8, the final output signal is formed: $f = f_1 + f_2 = g_Z + \ddot{h} + \Delta i + \Delta w + g_Z - \ddot{h} - \Delta i - \Delta w = 2g_Z$, where $f_1 = g_Z + \ddot{h} + \Delta i + \Delta w$ – output signal when armature 2 moves down; $f_2 = g_Z - \ddot{h} - \Delta i - \Delta w$ – output signal when armature 2 moves up; $\ddot{h}$ – vertical acceleration of the aircraft; Δi – residual instrumental errors; Δw – residual errors from the influence of projections of horizontal cross accelerations on the sensitivity axis of the invention.

That is, in the device 8 for calculating the output signal TG, an output signal equal to the doubled value is formed $2g_Z$. Unlike the transformer converter, the output signal of TG does not have measurement errors caused by the influence of vertical acceleration $\ddot{h}$, residual instrumental errors Δi and residual errors from the influence of horizontal cross accelerations Δw. Thus, it is shown that two-channel TG has a higher accuracy compared to known gravimeters.

4. Development of software for simulation of two-channel TG operation under the action of external perturbing accelerations

If we divide the two-channel TG equation of motion by m, we get:

$$\ddot{x} + 2 \cdot \xi\omega_0\dot{x} + \omega_0^2 x = -2g_z, \tag{7}$$

where ξ – damping factor; ω_0 – natural frequency of a two-channel TG.

Considering that in a real two-channel TG design there will be residual instrumental errors due to temperature effects, changes in medium pressure or other factors, as well as residual errors from the influence of vertical acceleration, which can lead to a non-linearity of the equation of motion of our two-channel TG , we rewrite equation (7) in the form [1, 9]:

$$m\ddot{x} + \dot{x}\left[2n - L\sin(\omega t + \varepsilon)\right] + \omega_0^2 x = N\sin\omega t, \tag{8}$$

where $L = mw_a$, $N = mw_b$ – vibration parameters; w_a, w_b – vibration acceleration amplitudes.

We consider in (8) that $M(t) = 2n - L\sin(\omega t + \varepsilon)$, and $D(t) = \omega_0^2$, then:

$$\ddot{x} + \dot{x}M(t) + D(t)x = 0, \tag{9}$$

where $M(t)$ *and* $D(t)$ – T-periodic functions.

Equation (9) without changing the characteristic indicators can be reduced to a similar one, where $M(t) = const$.

Let be

$$\int_0^t M(t_1)dt_1 = \Psi t + M_1(t), \tag{10}$$

where $\Psi = 2n$; $M(t_1) = \int_0^t (M(t_1) - \Psi)dt = \frac{L}{\omega}\cos(\omega t + \varepsilon)$.

After all mathematical transformations (10), the two-channel TG motion equation can be written as:

$$\ddot{x}' + 2\xi\omega_0\dot{x}' + (\omega_0^2 + v_1 w_b \sin\omega t)x' = 0{,}005\, w_a \sin\omega t, \tag{11}$$

where $v_1 = \frac{v_0}{w_b}$.

Thus, an equation (11) of the Mathieu-Hill type was obtained, taking into account residual errors from the influence of instrumental errors and $\ddot{h}$, which is convenient for computer simulation [1, 9, 10].

The software for modeling the operation of the two-channel TG under the action of external disturbances was developed taking into account (11) in the C# software environment. C# is an object-oriented programming language developed by Anders Galesberg, Scot Wiltamuth and Peter Golde under the auspices of Microsoft Research (at Microsoft).

The software product consists of one working window (Fig. 6), in which the parameters for modeling are set and its results are displayed in the form of Table 1 and graphs (Fig. 4-7).

In Table 1 we will give all the parameters that appear in the calculations and program interfaces.

Table 1

List of used parameters

№	Conventions	Name
1	2	3
1	ξ	Damping factor two-channel TG
2	w	Oscillation frequency
3	w_0	Natural frequency of two-channel TG
4	w_a	The amplitude of the perturbing action along the Oz axis
5	w_b	The amplitude of the perturbing action along the Oy axis
6	t_0	Start time
7	t_{max}	Limit of integration (end time)
8	dt	Integration step
9	m	Mass of the sensing element of the two-channel TG

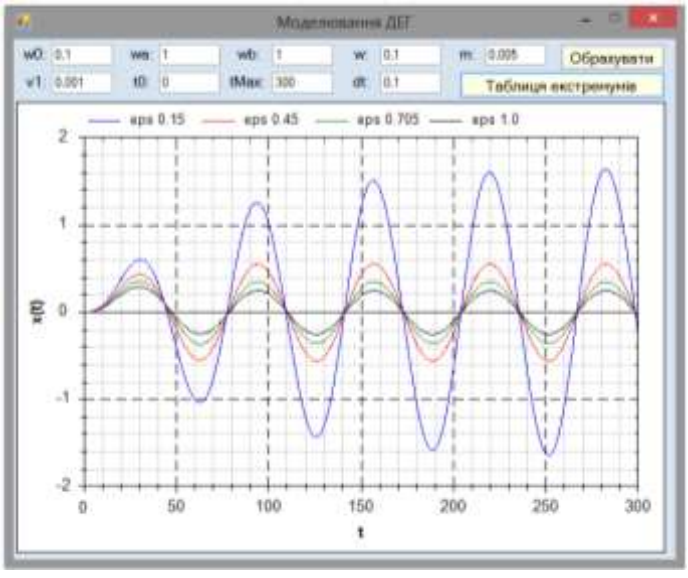

Figure 4. Interface of the computer program for simulating the operation of two-channel TG under the action of external perturbing accelerations

After entering the data in the appropriate fields of the program, for the calculation (or recalculation), you must click on the "Calculate" button — the graphs will change. To get the numerical values of extremes, you need to click on the button "Table of extremes". The program window will expand (Fig. 5.) and the required table will appear on the right side, as well as a schematic representation of the two-channel TG.

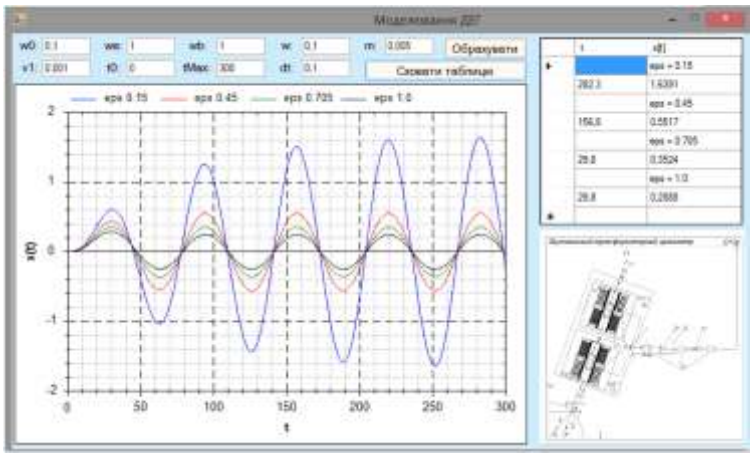

Figure 5. Extended interface of the computer program for modeling the operation of two-channel TG under the action of external perturbing accelerations

5. Results and discussion of computer simulation studies of the influence of unfavorable resonant modes

Thus, the equation of motion that we will model

$$\ddot{x} + 2\xi\omega_0\dot{x} + (\omega_0^2 + v_1 w_b \sin\omega t)x = 0{,}005\, w_a \sin\omega t,\ \ v_1 = \frac{v_0}{w_b}.$$

The parameters of the studied most unfavorable resonant modes are presented in the form of Table 2

Table 2

Parameters of the studied resonance processes

№	ω, c^{-1}	w_a	w_b	ξ			
		$м/с^2$		0,15	0,45	0,75	1
1		1	1	Resonance	0,110000	0,0661010	0,0496894
2		3	3		0,329914	0,1981360	0,1487170
3	ω_0 =0,1	3	10		0,329782	0,1979630	0,1485420
					1,099710	0,6604540	0,4957240
4		10	3				
5		3	15		0,329687	0,1978360	0,1484160
					1,349570	0,9906820	0,7435860
6		15	3				
7		1	1	0,130020	0,110905	0,0941927	0,0793500
8		3	3	0,389417	0,332314	0,2819150	0,2373970
9	ω_0 /2 =0,05	3	10	0,387163	0,339915	0,2796080	0,2352390
10		10	3	1,298060	1,140430	0,9397170	0,7913230
11		3	15	0,386474	0,338340	0,2779130	0,2338590
12		15	3	1,947090	1,710650	1,4095000	1,1869800
13		1	1	0,110504	0,109731	0,1004580	0,0932015
14	ω_0 /3 =0,03	3	3	0,331016	0,328430	0,3005490	0,2783220
15		3	10	0,329287	0,325772	0,2976650	0,2743310
16		10	3	1,103390	1,094770	1,0018300	0,9277410
17		3	15	0,328061	0,323891	0,2956390	0,2725110
18		15	3	1,65508	1,642150	1,5027400	1,3916100

19		1	1	No resonance Beats	0,0273533	0,0235304	0,0200020
					Continuation of Table 2		
20		3	3		0,0822427	0,0707352	0,0601209
21		3	10		0,0828793	0,0712361	0,0605205
					0,2741720	0,2357840	0,2004030
22	$2\omega_0 = 0,2$	10	3				
23		3	15		0,0833300	0,0715904	0,6080320
					0,4112140	0,3536760	0,3006050
24		15	3				
25		1	1	No resonance	0,0120460	0,0105930	0,0097958
26		3	3		0,0362657	0,0316432	0,0294926
27		3	10		0,0367120	0,0320451	0,0298588
					0,1208850	0,1054780	0,0983086
28	$3\omega_0 = 0,3$	10	3				
29		3	15		0,0370285	0,0323305	0,0301188
30		15	3		0,1813280	0,1582160	0,1474630

Let us represent the obtained graphs of the results of simulation of resonant modes in the form of Fig. 6-7.

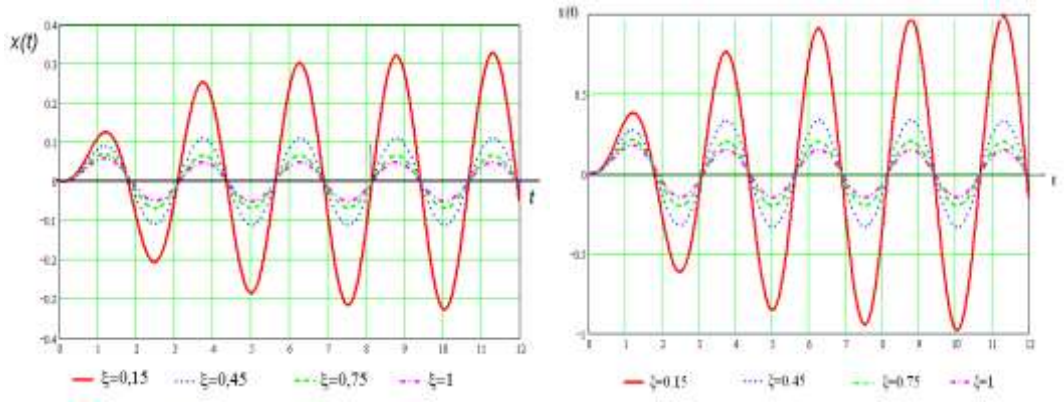

a b

Figure 6. Plot of two-channel TG output signal for different values of the damping factor ζ at $w_a = w_b = 1\,m/s^2$ and $\omega = \omega_0 = 0{,}1\,s^{-1}$ (a) and ζ at $w_a = w_b = 3\,m/s^2$ and $\omega = \omega_0 = 0{,}1\,s^{-1}$ (b)

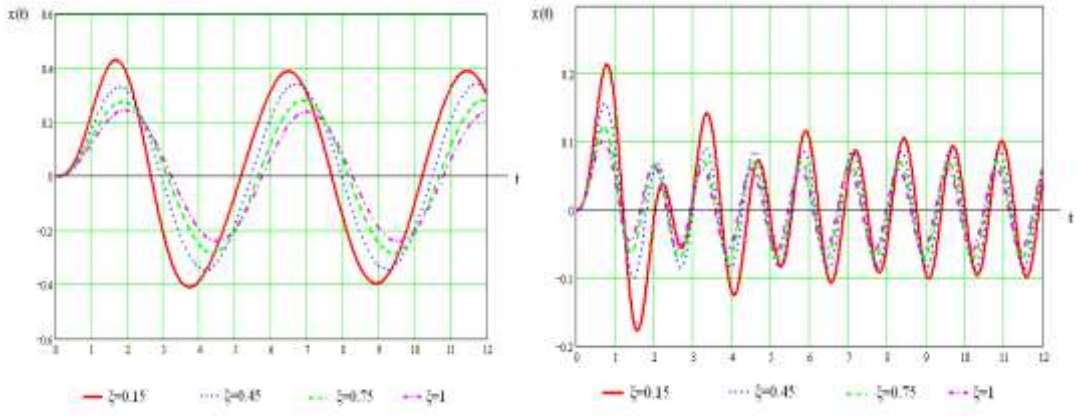

a b

Figure 7. Two-channel TG output plot for different damping ratios ζ at $w_a = w_b = 3\,m/s^2$ and $\omega = \omega_0 / 5 = 0{,}05\ s^{-1}$ (a) and ζ at $w_a = w_b = 3\,m/s^2$ and $\omega = 2\omega_0 = 0{,}2\ s^{-1}$.

Analyzing the obtained graphs of two-channel TG operation simulation in the most dangerous resonant modes, presented on Figures 6-7, we can draw the following conclusions:

1) The most dangerous, from the point of view of the possibility of resonance, is only the case of equality of the frequency of the perturbing action ω to the frequency of natural oscillations of the device ω_0, since resonance is possible with low damping ζ=0,15. For other frequency ratios ω and ω_0 ($2\omega = \omega_0$, $3\omega = \omega_0$), resonance does not occur even with low damping and different ratios of the amplitudes of disturbing accelerations ($w_a = 1, 3, 10, 15$ and $w_b = 1, 3, 10, 15\ m/s^2$).

With a frequency ratio $\omega = 2\omega_0$, $\omega = 3\omega_0$ and low damping, two-channel TG performs complex oscillations (beats) – the result of the addition of natural oscillations with a frequency of ω_0 and forced oscillations with a frequency of ω. With an increase in the relative damping coefficient ξ at $\omega = \omega_0$, the resonance is already eliminated at ξ=0,45, and at $\omega = 2\omega_0$, $\omega = 3\omega_0$, the beats turn into steady oscillations, which are carried out with a perturbation frequency ω.

Recommended values of relative damping coefficient $\xi = 0{,}45...0{,}75$ for $\omega = \omega_0$, $\omega = 2\omega_0$, $\omega = 3\omega_0$ and $\xi = 0{,}15...0{,}30$ for $2\omega = \omega_0$, $3\omega = \omega_0$.

2) The conclusion was confirmed that horizontal cross accelerations do not affect the operation of the TG, the amplitudes of the two-channel TG oscillations are directly proportional to the perturbing acceleration along the sensitivity axis.

3) Digital simulation of the influence of disturbing acceleration parameters on the two-channel TG AGS, as well as the instrument's own parameters, confirms the main advantage of two-channel TG over known gravimeters – its higher accuracy (rms error is 0.01 mGal).

Conclusions: formulation of conclusions based on the results obtained; comparison of the obtained results with existing results on the topic; evaluation of scientific novelty and practical value of the obtained results.

Formulation of conclusions based on the results obtained:

- a study of the stability of the new two-channel TG, in accordance with the Nyquist and Hurwitz criteria, showed that DTG is stable;
- as a result of the simulation of the most dangerous resonant modes, graphs of the change in the output signal x(t) of a two-channel transformer gravimeter for different values of the perturbation frequency ω and different values of the amplitudes of disturbing vibrational accelerations wa, wb and different values of the damping coefficient in the most dangerous resonant modes were obtained. It has been established that only the case of the main resonance $\omega = \omega_0$ is the most dangerous. Resonance may occur with a small damping factor. It is shown that as the damping coefficient increases to 0.705, the resonance disappears. For other frequency ratios, resonance does not occur even with a small damping factor;
- digital simulation of the influence of vibrational acceleration parameters on the DTG, as well as its own parameters, confirms the main advantage of the DTG over the known gravimeters — its higher accuracy.

Comparison of the obtained results with existing results on this topic:

the results obtained are not contained in previously published materials.

Evaluation of the scientific novelty of the results obtained:

in this article, the following new results were obtained: for the first time, modeling was carried out and the corresponding graphs of the most dangerous resonant modes of a new two-channel transformer gravimeter were obtained. It is shown that resonance is possible only in the case when the frequency of perturbing vibrational accelerations is equal to the frequency of natural vibrations of the device. It is shown that the resonance is eliminated by increasing the damping coefficient to 0.705. In other cases, resonance does not occur.

Assessment of the practical value of the results obtained:

the practical value of the results obtained in this article lies in the fact that the expediency of the practical use of a new two-channel transformer gravimeter is substantiated, since it has greater accuracy compared to known gravimeters, is stable, has a simple design and a powerful doubled output signal for its operation, does not affect horizontal cross accelerations with any ratio of their frequency and the natural frequency of a two-channel transformer gravimeter.

References

1 Безвесильная Е.Н. Авиационные гравиметрические системы и гравиметры / Е.Н. Безвесильная. — Житомир: ЖДТУ, 2007. — 604 с.

2 Быковский А.В. К вопросу о разработке малогабаритного аэрогравиметра / А.В. Быковский, А.В. Полынков // Вестн. МГТУ им. Н.Э. Баумана. — 2013. — № 2 (14). — С. 32–41.

3 Гирняк Ю.В. Микроэлектромеханические системы в современном приборостроении / Ю.В. Гирняк // Измерительная техника и метрология. — 2008. — № 69. — С. 97–102.

4 Безвесильная Е.Н. Преобразователи физических величин. Технические средства автоматизации: учеб. с грифом ЖДТУ / Е.Н. Безвесильная. — Киев: НПО «Приоритеты», 2019. — 809 с.

5 Патент № 113038. Авиационная гравиметрическая система для измерения аномалий ускорения силы тяжести. МПК: G01V 7/02, G01V 7/16, G01P 15/09 [Текст] / Е.Н. Безвесильная, А.Г. Ткачук, Т.В. Хильченко. — № A201512205. — Заявл. 09.12.2015. — Опубл. 25.11.2016. — Бюлл. № 22.

6 Huang Y. SGA-WZ: A New Strapdown Airborne Gravimeter / Y. Huang, A.V. Olesen, M. Wu, K. Zhang // Sensors. — 2012. — Vol. 12, Issue 12. — P. 9336–9348. doi: 10.3390/s120709336.

7 Патент на полезную модель 142824; МПК: G01V 7/00 (2020.01 Патент на полезную модель 142824; МПК: G01V 7/00 (2020.01). Трансформаторный гравиметр. — Заявитель и патентодержатель — Государственный университет «Житомирская политехника» / А.Г. Ткачук, Е.Н. Безвесильная. — u2020 00884. — Заявл. 12.02.2020. — Недр. 25.06.20220. — Бюлл. № 12.

8 Самотокин Б.Б. Лекции по теории автоматического управления / Б.Б. Самотокин. — Житомир: ЖИТИ, 2001. — 508 с.

9 Безвесильная Е.Н. Авиационные гравиметрические системы и гравиметры / Е.Н. Безвесильная. — Житомир: ЖДТУ, 2007. — 504 с.

10 Roussel C. Integration of a strapdown gravimeter system in an autonomous underwater vehicle / C. Roussel, J. Verdun, J. Cali, M. Maia // ISPRS — International Archives of the Photogrammetry, Remote Sensing and Spatial Information Sciences. — 2015. — Vol. XL-5/W5. — P. 199–206. doi: 10.5194/isprsarchives-xl-5-w5-199-2015.

11 Быковский А.В. Аэрогравиметрический метод измерения гравитационных аномалий / А.В. Быковский, А.В. Полынков, В.Д. Арсеньев // Авиакосмическое приборостроение. — 2013. — № 12. — С. 11–19.

12 Bezvesilna E. Two-channel MEMS gravimeter for the automated aircraft gravimetric system / I. Korobiichuk, E. Bezvesilna, A. Tkachuk, A. Praczukowska, T. Khylchenko // Systems, Control and Information Technology Warsaw, 20-21.05.2016/ P.481-488.

13 Gramert W.R. Third generation aero gravity system / W.R. Gramert // International Association of Geodesy Symposium G4, IUGG XXI General Assembly. — Boulder, Colorado, 1995.

14 Harrison J.C. The LST Airborne Gravity System / J.C. Harrison, J.D. MacQueen, A.C. Rauhut, J.Y. Cruz // International Association of Geodesy Symposium G4, IUGG XXI General Assembly. — Boulder, Colorado, 1995.

15 Wei M. Analysis of GPS-derived acceleration from airbornetests / M. Wei, K. Schwarz // International Association of Geodesy Symposium G4, IUGG XXI General Assembly. — Boulder, Colorado, 1995.

16 Huang Y. SGA-WZ: A New Strapdown Airborne Gravimeter / Yangming Huang, Arne Vestergaard Olesen, Meiping Wu, Kaidong Zhang // Sensors. — 2012. — No. 12(7).

17 Calvoa M. Time stability of spring and superconducting gravimeters through the analysis of very long gravity records / Marta Calvoa, Jacques Hinderera, Severine Rosata, Hilaire Legrosa, Jean-Paul Boya, Bernard Ducarmec, Walter Zürnd // Journal of Geodynamics. — 2014. — No. 80. — P. 20–33.

18 Agostino G.D. The new IMGC-02 transportable absolute gravimeter: measurement apparatus and applications in geophysics and volcanology / G. Agostino, S. Desogus, A. Germak, C. Origlia, D. Quagliotti, G. Berrino, G. Corrado, V. Derrico, G. Ricciardi // Annals of geophysics. — 2008. — No. 51(1). — P. 39–40.

19 Roussela C. Integration of a strapdown gravimeter system in an autonomous underwater vehicle / C. Roussela, J. Verduna, J. Calia, M. Maiab // The International Archives of the Photogrammetry, Remote Sensing and Spatial Information Sciences. — 2015. — No XL-5/W5. — P. 199–206.

20 CG-5 Autograv Gravity Meter. 08.01.2023. — [Electronic resource]. — Access mode: https://scintrexltd.com/download/cg-5-operation-manual/.

21 Струнный гравиметр «Graviton-M». — 18.07.2017. — [Электронный ресурс]. — Режим доступа: http://www.aerogeo.ru/index.php?option=com_content&view=category&layout=blog&id=25&Itemid=17&lang.

22 Aerogravimetr GT-2A. — [Electronic resource]. — 18.07.2017. — Access mode: http://www.aerogeo.ru/index.php?option=com_content&view=category&layout=blog&id=25&Itemid=17&lang=ru.

23 Бержицкий В.Н. Инерциально-гравиметрический комплекс МАГ–1 (GT–1A). Опыт разработки и результаты летных испытаний / В.Н. Бержицкий, В.Н. Ильин, Е.Б. Савельев, Ю.Л. Смоллер, С.Ш. Юрист, Ю.В. Болотин, А.А. Голован, Н.А. Парусников, Г.В. Попов, М.В. Чичинадзе // Гироскопия и навигация. — 2002. — № 3 (38). — С. 104–116.

24 Мобильный гравиметр «Чекан–АМ». — 26.01.2017. — [Электронный ресурс]. — Режим доступа: http://www.elektropribor.spb.ru/ru/rprod6-1.html.

25 TAGS–6. — 26.01.2023. — [Электронный ресурс]. — Режим доступа: http://www.microglacoste.com/tags-6.php.

26 Пат. № 109746. Авіаційна гравіметрична система для вимірювань аномалій прискорення сили тяжіння / О. М. Безвесільна, А.Г. Ткачук, Л.О. Чепюк // Опубл. 25.09.2015, Бюл. № 18.

27 Заявка на изобретение №а2012 11163 Украина, МРК G01V 7/06. Авиационная гравиметрическая система для изменения аномалий ускорения силы тяжести / Е.Н. Безвесильная, А.Г. Ткачук. — Заявл. 26.09.2012.

28 Авиационная гравиметрическая система для измерения аномалий ускорения силы тяжести. Патент №105122 Украина: МРК G01V 7/00 / Е.Н. Безвесильная, А.Г. Ткачук, К.С. Козько. — Заявл. 01.04.13. Опубликовано 25.12.13. Бюлл. № 24. — 5 с.

29 Патент 2253882, Россия, МПК G 01 V 7/02. Гравиметр / А.П. Быков, О.Е. Енина, В.П. Кулеш, Л.М. Москалик.

30 Патент 548820, Россия, МПК G 01 V 7/02. Гравиметр / В.Б. Брагинский, В.П. Матюнин. — Заявл. 10.11.74. — Опубл. 28.02.77. — Бюлл. № 8.

31 Патент 1121639, РФ, МПК G 01 V 7/12. Гравиметр / Е.И. Попов, В.П. Матюнин, А.Б. Манукин, В.Н. Конешов, Л.К. Железняк, Г.А. Гусев. — Заявл. 22.06.82. — Опубл. 30.10.84.

Е.Н. Безвесельна, Ю.В. Киричук, М.С. Гриневич, Т.А. Толочко

Жаңа екі каналды трансформер гравиметрінің жұмысындағы бұзылған діріл үдеуі параметрлерінің әсерін модельдеу

Мақалада автоматтандырылған авиациялық гравиметриялық жүйенің жаңа екі арналы трансформаторлық гравиметрі қарастырылған, оның дәлдігі бүгінгі күні белгілі гравиметрлерден жоғары. Оның дизайны сипатталған. Жаңа екі арналы трансформаторлық гравиметрдің жұмысына бұзылатын діріл үдеуі параметрлерінің әсері модельденді. Екі арналы трансформаторлық гравиметрдің жұмысына аса қолайсыз резонанстық жағдайлар үшін жиіліктер мен қоздырғыш үдеулердің амплитудаларының әсері ЭЕМ көмегімен зерттелді. Өйткені бүгінгі күні екі арналы трансформаторлық гравиметрді авиациялық гравиметриялық жүйенің гравиметрі ретінде қолдану мүмкіндігі мен арнайы мақсатта зерттеуге арналған ғылыми, теориялық және практикалық жұмыстар жоқ. Трансформатордың гравиметрі магнит тізбегінен, жылжымалы арматурадан, бастапқы қоздыру орамынан және екі бірдей секциясы бар қайталама шығыс орамынан тұратын сезімтал элементті қамтиды. Екінші реттік орамның екі секциясы бір-біріне қарама-қарсы жалғанған, ал қозғалмалы якорь қозғалтқышқа қосылады, ол белгілі бір мерзімде якорьді төмен түсіреді және магниттік контур бойымен жоғары көтеріледі, ал қозғалтқышты басқару кернеуінің көзіне қосылған коммутациялық құрылғы басқарады, ал екінші реттік шығыс орамасынан шығатын сигнал шығыс сигналының калькуляторының кірісіне беріледі, онда шығыс сигналы пайда болады, ол гравитациялық үдеудің екі еселенген мәніне пропорционалды. Трансформаторлық гравиметр ұшу аппаратының бортынан гравитациялық үдеу векторының тік құрамдас өлшеу құралдарына жатады және оны геодезия, геофизика саласында, атап айтқанда, Жер шарының жетуі қиын аудандарында тіректік гравиметриялық желіні қалыптастыру кезінде, сондай-ақ ұшақтар мен зымыран жасауда қолдануға болады. Трансформаторлық гравиметр ұшу аппаратында орналасқан авиациялық гравиметриялық жүйенің құрамына кіреді.

Кілт сөздер: екі арналы трансформаторлық гравиметр, қоздырушы әрекет, резонанстық режимдер, бәсеңдету, гравитациялық үдеу.

Е.Н. Безвесильная, Ю.В. Киричук, М.С. Гриневич, Т.А. Толочко

Моделирование влияния параметров возмущающих вибрационных ускорений на работу нового двухканального трансформаторного гравиметра

Рассмотрен новый двухканальный трансформаторный гравиметр автоматизированной авиационной гравиметрической системы, точность которого выше известных сегодня гравиметров. Описана его конструкция. Проведено моделирование влияния параметров возмущающих вибрационных ускорений на работу нового двухканального трансформаторного гравиметра. Исследовано с помощью ЭВМ влияние частот и амплитуд возмущающих ускорений для наиболее неблагоприятных резонансных случа-

ев на работу двухканального трансформаторного гравиметра. Ведь сегодня отсутствуют научно-теоретические и практические работы, посвященные исследованиям возможности и целесообразности использования в качестве гравиметра АГС двухканального трансформаторного гравиметра. Трансформаторный гравиметр содержит чувствительный элемент, состоящий из магнитопровода, подвижного якоря, первичной обмотки возбуждения и вторичной выходной обмотки, имеющей две одинаковые секции. Две секции вторичной обмотки соединены последовательно-встречно, а подвижный якорь соединен с двигателем, который с определенным периодом опускает якорь вниз и поднимает вверх по магнитопроводу, причем двигателем управляет устройство переключения, подключенное к источнику напряжения управления, а выходной сигнал со вторичной выходной обмотки подается на вход устройства вычисления выходного сигнала, где генерируется выходной сигнал, пропорциональный удвоенному значению гравитационного ускорения. Трансформаторный гравиметр относится к средствам измерения вертикальной составляющей вектора гравитационного ускорения с борта летательного аппарата и может использоваться в области геодезии, геофизики, в частности, при формировании опорных гравиметрических сеток труднодоступных районов Земного шара, а также в авиа- и ракетостроении. Трансформаторный гравиметр входит в состав авиационной гравиметрической системы, размещённой на летательном аппарате.

Ключевые слова: двухканальный трансформаторный гравиметр, возмущающее воздействие, резонансные режимы, демпфирование, гравитационное ускорение.

References

1 Bezvesilnaia, E.N. (2007). Aviatsionnye gravimetricheskie sistemy i gravimetry [Aviation gravimetric systems and gravimeters]. Zhytomyr: ZHDTU [in Russian].

2 Bykovsky, A.V., & Polynkov, A.V. (2013). K voprosu o razrabotke malogabaritnogo aerogravimetra [On the issue of developing a small-sized aerogravimeter]. *Vestnik Moskovskogo gosudarstvennogo tekhnicheskogo universiteta imeni N.E. Baumana — Bulletin of the Moscow State Technical University named after N.E. Bauman*, 2 (14), 32–41 [in Russian].

3 Hirnyak, Yu.V. (2008). Mikroelektromekhanicheskie sistemy v sovremennom priborostroenii [Microelectromechanical systems in modern instrumentation]. *Izmeritelnaia tekhnika i metrologiia — Measuring technique and metrology*, 69, 97–102 [in Russian].

4 Bezvesilnaya, E.N. (2019). Preobrazovateli fizicheskikh velichin. Tekhnicheskie sredstva avtomatizatsii [Converters of physical quantities. Technical automation equipment]. Textbook with the stamp of SUZP. Kiev: NPO «Prioritety» [in Russian].

5 Bezvesilnaya, E.N., Tkachuk, A.G., & Khilchenko, T.V. (2016). *Aviatsionnaia gravimetricheskaia sistema dlia izmereniia anomalii uskoreniia sily tiazhesti [Aviation gravimetric system for measuring gravity acceleration anomalies]*. Patent № 113038, State University Zhytomyr Polytechnic [in Russian].

6 Huang, Y., Olesen, A.V., Wu, M., & Zhang, K. (2012). SGA-WZ: A New Strapdown Airborne Gravimeter [Text]. *Sensors, Vol. 12*, Issue 12, P. 9336–9348. doi: 10.3390/s120709336.

7 Tkachuk, A.G., & Bezvesilna, E.N. (2020). *Transformatornyi gravimetr [Transformer gravimeter]*. Patent № 142824, Zhytomyr Polytechnic State University [in Russian].

8 Samotokin, B.B. (2001). *Lektsii po teorii avtomaticheskogo upravleniia [Lectures on the theory of automatic control]*. Zhytomyr: SYZP [in Russian].

9 Bezvesilnaya, E.N. (2007). *Aviatsionnye gravimetricheskie sistemy i gravimetry [Aviation gravimetric systems and gravimeters]*. Zhytomyr: SYZP [in Russian].

10 Roussel, C., Verdun, J., Cali, J., & Maia, M. (2015). Integration of a strapdown gravimeter system in an autonomous underwater vehicle. *ISPRS — International Archives of the Photogrammetry, Remote Sensing and Spatial Information Sciences, Vol. XL-5/W5*, 199–206. doi: 10.5194/isprsarchives-xl-5-w5-199-2015.

11 Bykovsky, A.V., Polynkov, A.V., & Arsenyev, V.D. (2013). Aerogravimetricheskii metod izmereniia gravitatsionnykh anomalii [Aerogravimetric method for measuring gravitational anomalies]. *Aviakosmicheskoe pribrostroenie — Aerospace instrumentation*, 12, 11–19 [in Russian].

12 Bezvesilna, E., Korobiichuk, I., Tkachuk, A., Praczukowska, A., & Khylchenko, T. (2016). Two-channel MEMS gravimeter for the automated aircraft gravimetric system. *Systems, Control and Information Technology Warsaw*, 481-488.

13 Gramert, W.R. (1995). Third generation aero gravity system. *International Association of Geodesy Symposium G4, IUGG XXI General Assembly.* Boulder, Colorado.

14 Harrison, J.C., MacQueen, J.D., Rauhut, A.C., & Cruz, J.Y. (1995). The LST Airborne Gravity System. *International Association of Geodesy Symposium G4, IUGG XXI General Assembly.* Boulder, Colorado.

15 Wei, M., & Schwarz, K. (1995). Analysis of GPS-derived acceleration from airbornetests. *International Association of Geodesy Symposium G4, IUGG XXI General Assembly*. Boulder, Colorado.

16 Huang, Y., Olesen, Arne Vestergaard, Wu, Meiping, & Zhang, Kaidong (2012). SGA-WZ: A New Strapdown Airborne Gravimeter. *Sensors*, 12(7).

17 Calvoa, M., Hinderera, Jacques, Rosata, Severine, Legrosa, Hilaire, Boya, Jean-Paul, Ducarmec, Bernard, & Zürnd, Walter (2014). Time stability of spring and superconducting gravimeters through the analysis of very long gravity records. *Journal of Geodynamics*, 80, 20–33.

18 Agostino, G.D., Desogus, S., Germak, A., Origlia, C., Quagliotti, D., Berrino, G., Corrado, G., Derrico, V., & Ricciardi, G. (2008). The new IMGC-02 transportable absolute gravimeter: measurement apparatus and applications in geophysics and volcanology. *Annals of geophysics*, 51(1), 39–40.

19 Roussela, C., Verduna, J., Calia, J., & Maiab, M. (2015). Integration of a strapdown gravimeter system in an autonomous underwater vehicle. *The International Archives of the Photogrammetry, Remote Sensing and Spatial Information Sciences*, №XL-5/W5, 199–206.

20 CG-5 Autograv Gravity Meter. 08.01.2023. Retrieved from https://scintrexltd.com/download/cg-5-operation-manual/.

21 Strunnyi gravimetr «Graviton-M» [String gravimeter "Graviton-M"] (18.07.2016) / AO «GNPP Aerogeofizika». Retrieved from http://www.aerogeo.ru/index.php?option=com_content&view=category&layout=blog&id=25&Itemid=17&lang=ru.

22 Aerogravimetr GT-2A (18.07.2016). Retrieved from http://www.aerogeo.ru/index.php?option=com_content&view=category&layout=blog&id=25&Itemid=17&lang=ru.

23 Berzhitskii, V.N., Ilin, V.N., Savelev, E.B., Smoller, Yu.L., Yurist, S. Sh., Bolotin, Yu.V., Golovan, A.A., Parusnikov, N.A., Popov, G.V., & Chichinadze, M.V. (2002). Inertsialno-gravimetricheskii kompleks MAG–1 (GT–1A). Opyt razrabotki i rezultaty letnykh ispytanii [Inertial gravimetric complex MAG-1 (GT-1A). Development experience and flight test results]. *Giroskopiia i navigatsiia — Gyroscopy and navigation*, 3 (38), 104–116 [in Russian].

24 Mobilnyi gravimetr «Chekan–AM» [Mobile gravimeter Chekan-AM] (26.01.2017). Retrieved from http://www.elektropribor.spb.ru/ru/rprod6-1.html. [in Russian].

25 TAGS-6 (26.01.2017). Retrieved from http://www.microglacoste.com/tags-6.php.

26 Bezvesilnaya, E.N., Tkachuk, A.G., & Chepjuk, L.O. (2015). *Aviatsiina gravimetrychna systema dlia vymiriuvan anomalii pryskorennia syly tiazhinnia.* Patent № 109746 Ukrain.

27 Bezvesilnaya, E.N., & Tkachuk, A.G. (2012). *Aviatsionnaia gravimetricheskaia sistema dlia izmeneniia anomalii uskoreniia sily tiazhesti* [*Aviation gravimetric system for changing gravity acceleration anomalies]*. Patent № 11163 Ukrain.

28 Bezvesilnaya, E.N., Tkachuk, A.G., & Kozko, K.S. (2013). *Aviatsionnaia gravimetricheskaia sistema dlia izmeneniia anomalii uskoreniia sily tiazhesti* [*Aviation gravimetric system for measuring gravity acceleration anomalies]*. Patent № 105122 Ukraine.

29 Bykov, A.P., Enina, O.E., Kulesh, V.P., & Moskalik, L.M. (1979). *Gravimetr.* Patent № 2253882 Russia [in Russian].

30 Braginskiy, V.B., & Matyunin, V.P. (1977). *Gravimetr*. Patent № 548820, Russia [in Russian].

31 Popov, E.I., Matyunin, V.P., Manukin, A.B., Koneshov, V.N., Zheleznyak, L.K., & Gusev, G.A. (1984). *Gravimetr*. Patent № 1121639 RF [in Russian].

DOI 10.31489/2023PH4/38-49

UDC 533.15:536.25

O.V. Fedorenko[2], V.N. Kossov[1*], S.A. Krasikov[1], M. Zhaneli[1], T. Seydaz[1]

[1]*Abai Kazakh National Pedagogical University, Almaty, Kazakhstan;*
[2] *al-Farabi Kazakh National University, Almaty, Kazakhstan*
[*]*Corresponding authors e-mail*: kosov_vlad_nik@list.ru

Numerical modelling of multi-component mass transfer regimes in four-component gas systems

For argon and carbon dioxide, which are part of the tetra-component gas mixture He + Ar + CO2 – N2 and are the heaviest compared to other components, graphs of the behavior of the concentration of these components at different points of the diffusion channel and time intervals are presented. To simulate convective flows in the four-component mixture under consideration, the Flow Simulation computer package included in the SolidWorks engineering design system was used. The equations are solved by the finite volume method using the standard k – ε turbulence model and with initial and boundary conditions. Indicated, that obtained distributions change nonlinearly both in time and along the length of the diffusion channel. In this case, there is a change in the diffusion process to a convective one, which is due to the nonlinearity in the distribution of the components concentration, which is connected with the imbalance of mechanical equilibrium. It was found that the most significant change in the behavior of the concentrations of heavy-weight components occurs within 120 s. This time interval coincides with the appearance of two contrasting areas on the graphs, namely, the formation of a developed convective flow. An enhancement in the time of the numerical experiment showed that the concentration of the component with the maximal molar mass remains practically unchanged. This behavior of the concentration of heavy-weight components is characteristic of the effect when the mixture is enriched in the heavy-weight component. An analysis of the streamlines on the plots of concentration distributions showed that vortices of various scales interacting with each other and leading to a pulsating mixing regime are formed along the length of the channel. It has been established that the presence of large-scale vortices determines the preferential migration of the components with the maximal molar mass.

Keywords: gas mixtures, diffusion, instability, convection, concentration distribution, anomalous component separation, numerical modeling, finite volume method.

Introduction

Multicomponent diffusion in gas systems differs from ordinary binary diffusion occurring under isothermal conditions in that new phenomena arise in multicomponent mixtures due to the mutual influence of the components on each other and confirmed by experimental studies and from the analysis of the Stefan-Maxwell equations [1]. There are the following phenomena (special mixing modes), such as a reverse diffusion, osmotic diffusion and diffusion barrier [2], as well as the onset of the mechanical equilibrium instability of the mixture, which is caused by the distinction in the interdiffusion coefficients of the miscible components [3, 4]. An essential nonlinearity along the channel length of the distributions of the concentrations of heavy components can lead to the appearance of convective instability under isothermal conditions, which follows from the results of numerical studies [5]. As a further matter, if some conditions are formed in the system, then nonmonotonicity with both a minimum and a maximum is also possible in the mixture density distribution, which can cause gravitational convection that is not observed during diffusion at a constant temperature [6].

Analysis of the stability of isothermal ternary gas mixtures carried out within the bounds of the Boussinesq approximation [7] showed that the transfer from the diffusion mode to the convection one is possible in both situations when the mixture density reduces with altitude and when the density gradient has the opposite direction [8]. Nevertheless, the proposed approach has a number of limitations that do not allow one to describe the onset time of the unstable regime and the evolution of convection currents.

Experimental research on the diffusion of steam mixtures of solutions into an inactive gas [3], as well as blending in ternary gaseous mixtures at various compounds and pressures [4, 9], showed that convection currents are observed. These currents cause a synergistic effect, resulting in an essential acceleration of the mixing process of the system's components. Also in [4, 9], the preferred migration of the component with the maximal molar mass was found, which is an unusual phenomenon for diffusion processes. Sometimes, the

pulsating nature of the mixing was also recorded. The results obtained in [3, 4, 9], which showed the possibility of enriching the resulting mixture with a constituent having the maximal molar mass, are also of practical importance since they can be implemented in combined approaches relating to the growth of the selective features of a given component [10, 11]. Including those based on the use of membranes [12, 13] and convective separation mechanisms [14, 15]. At the same time, experimental and numerical studies of combined mass transfer in isothermal four-component systems are episodic. Consequently, it is extremely important to conduct studies aimed at clarifying the separation mechanisms in gas mixtures consisting of several components, as well as correctly assessing the parameters that determine the transition from one mixing mode to another. These issues play a significant role in both applied and fundamental problems related to mass carry.

The main objective of this paper is to create a numerical model for the analysis of various modes of multicomponent mass transfer in a tetra-component gaseous mixture He + Ar + CO_2 – N_2. A feature of this system is the selected composition, which approximately provides the condition of the zero density gradient of the mixture. The distributions of concentrations of argon and carbon dioxide over time and along the length of a vertical flat diffusion channel at elevated pressure under isothermal conditions have been obtained and analyzed.

Mathematical description of the occurrence of convective flows in a quaternary gas mixture

The study of mass transfer in systems consisting of more than two components is possible due to the use of the Navier-Stokes equation, as well as equations describing the conservation of energy, momentum, and mass in a given medium. Moreover, when modeling mass transfer in multicomponent gas systems, not only the equations of state of the fluid components are taken into account, but also empirical relationships that consider the dependence of the viscosity and thermal conductivity of each component on temperature. Averaging the effect of turbulence on flow parameters on a small time scale is used in modeling convective flows in the Navier-Stokes equation. In addition, the introduction of the corresponding time derivatives makes it possible to take into account large-scale temporal changes averaged over a small time scale of the components of the gas-dynamic parameters of the flow [16]. The Navier-Stokes equations, which are used to represent convective flows, have extra variables that describe Reynolds stresses. Additional equations that describe the transport of turbulence kinetic energy and its dissipation in the framework of the *k*-*ε* turbulence model are utilized to completely close this system of equations [17]. This set of equations, which takes into consideration unsteady spatial flow, comprises mass, momentum, and energy conservation equations [16], can be presented as:

$$\frac{\partial \rho}{\partial t} + \frac{\partial}{\partial x_i}\left(\rho u_i\right) = 0, \quad i = 1, 2, 3 \tag{1}$$

$$\frac{\partial\left(\rho u_i\right)}{\partial t} + \frac{\partial}{\partial x_j}\left(\rho u_i u_j - \tau_{ij}\right) + \frac{\partial p}{\partial x_i} = S_i, \quad j = 1, 2, 3, i \neq j \tag{2}$$

$$\frac{\partial(\rho E)}{\partial t} + \frac{\partial}{\partial x_i}\left(\left(\rho E + p\right)u_i + q_i - \tau_{ij}u_j\right) = S_i u_i, \tag{3}$$

$$E = U + \frac{u^2}{2}, \tag{4}$$

where ρ is the fluid density, u_i or u_j is the flow rate, t is the time, p is the fluid pressure, q_j is the diffusion heat flux, τ_{ij} is the viscous shear stress tensor (the subscripts mean the summation in three coordinate directions), E is the total energy of unit mass of current medium, U is the specific internal energy of the medium, S_i is the external mass forces due to the gravitational action $S_i = S_i^{gravity}$ ($S_i^{gravity} = -\rho g_i$) acting on unit mass of the current medium along the coordinate directions x_i, g_i is the component of the gravitational acceleration in the x_i coordinate direction.

The viscous shear stress tensor for Newtonian fluids is calculated as:

$$\tau_{ij} = \mu\left(\frac{\partial u_i}{\partial x_j} + \frac{\partial u_j}{\partial x_i} - \frac{2}{3}\delta_{ij}\frac{\partial u_l}{\partial x_l}\right) - \frac{2}{3}\rho k\delta_{ij}, \tag{5}$$

where k is the kinetic energy of turbulence, δ_{ij} is the Kronecker delta function ($\delta_{ij} = 1$ at $i = j$; $\delta_{ij} = 0$ at $i \neq j$), $\mu = \mu_l + \mu_t$, μ_l is the dynamic viscosity coefficient, and μ_t is the turbulent viscosity coefficient. When using the $k - \varepsilon$ turbulence model, the turbulent viscosity coefficient μ_t is determined through the parameters of the kinetic energy of turbulence k and the dissipation rate of this energy ε:

$$\mu_t = f_\mu \frac{C_\mu \rho k^2}{\varepsilon}, \tag{6}$$

where $C_\mu = 0.09$ is the empirical constant defining the turbulent viscosity, $f_\mu = \left[1 - \exp\left(-0.025R_y\right)\right]^2\left(1 + \frac{20.5}{R_T}\right)$ is the damping function, $R_y = \frac{\rho\sqrt{k}y}{\mu_l}$ is the Reynolds number, where y is the distance from the wall surface, $R_T = \frac{\rho k^2}{\mu_l \varepsilon}$ is the turbulent Reynolds number.

The following equations make it possible to determine the parameters of the turbulent kinetic energy k and the dissipation rate of this energy ε:

$$\frac{\partial \rho k}{\partial t} + \frac{\partial}{\partial x_j}\left(\rho u_j k\right) = \frac{\partial}{\partial x_j}\left(\left(\mu_l + \frac{\mu_t}{\sigma_k}\right)\frac{\partial k}{\partial x_j}\right) + S_k, \tag{7}$$

$$\frac{\partial \rho \varepsilon}{\partial t} + \frac{\partial}{\partial x_j}\left(\rho u_j \varepsilon\right) = \frac{\partial}{\partial x_j}\left(\left(\mu_l + \frac{\mu_t}{\sigma_\varepsilon}\right)\frac{\partial \varepsilon}{\partial x_j}\right) + S_\varepsilon, \tag{8}$$

where $S_\varepsilon = C_{\varepsilon 1}\frac{\varepsilon}{k}\left(f_1 \tau_{ij}^R \frac{\partial u_i}{\partial x_j} + \mu_t C_B P_B\right) - C_{\varepsilon 2} f_2 \frac{\rho \varepsilon^2}{k}$, $S_k = \tau_{ij}^R \frac{\partial u_i}{\partial x_j} - \rho\varepsilon + \mu_l P_B$,

$P_B = -\frac{g_i}{\sigma_B}\frac{1}{\rho}\frac{\partial \rho}{\partial x_i}$ is the generation of turbulent kinetic energy due to repulsive force, $\tau_{ij}^R = \mu_t\left(\frac{\partial u_i}{\partial x_j} + \frac{\partial u_j}{\partial x_i} - \frac{2}{3}\delta_{ij}\frac{\partial u_l}{\partial x_l}\right) - \frac{2}{3}\rho k\delta_{ij}$, $\sigma_R = 0.9$ is the turbulent Prandtl constant for energy, $C_R = 1$ is the constant determining the degree of impact of the repulsive force on ε at $P_R \succ 0$ and $C_R = 0$ at $P_R \leq 0$, $f_1 = 1 + \left(\frac{0.05}{f_\mu}\right)^3$, $f_2 = 1 - \exp\left(-R_T^2\right)$, $C_{\varepsilon 1} = 1.44$ is the empirical constants of the model for the generation term of the equation for ε, $C_{\varepsilon 2} = 1.92$ is the empirical constants of the model for the dissipation term of the equation for ε, $\sigma_k = 1$ and $\sigma_\varepsilon = 1.3$ are the Prandtl numbers for the turbulent kinetic energy k and the energy dissipation rate ε.

To simulate the diffusion heat flow, an equation is used that has the following form:

$$q_i = -\left(\frac{\mu_l}{\mathrm{Pr}} + \frac{\mu_t}{\sigma_c}\right)c_p \frac{\partial T}{\partial x_i}, \qquad i = 1, 2, 3 \tag{9}$$

where T is the temperature of the fluid medium, c_p is the specific heat capacity at constant pressure, Pr is the Prandtl number, $\sigma_c = 0.9$ is the Prandtl turbulence number.

To study the diffusion of components in multicomponent gas mixtures, equations are used that describe the change in the concentration of each component in space:

$$\frac{\partial \rho c_i}{\partial t} + \frac{\partial}{\partial x_j}\left(\rho u_j c_i\right) = \frac{\partial}{\partial x_j}\left(\left(D_{ij} + D_{ij}^t\right)\frac{\partial c_i}{\partial x_j}\right),\ i, j = 1, 2, \ldots N, \tag{10}$$

where D_{ij}, D_{ij}^t is the molecular and turbulent diffusion coefficients, which according to the Fick's law, so that $D_{ij} = D \cdot \delta_{ij}$, $D_{ij}^t = \delta_{ij} \cdot \frac{\mu_t}{\sigma}$, where D is the interdiffusion coefficient, σ is the turbulent Schmidt number, c_i is the concentration of the i-th component of mixture $\left(\sum_{i=1}^{N} c_i = 1\right)$, N is the number of components in mixture.

To find a solution to the system of equations (1)-(10), the following boundary conditions are taken into account, which complement the problem posed and ensure the accuracy of the result obtained:

$$u_i\big|_n = 0,\ u_i\big|_t = 0,\ \left.\frac{\partial u_i}{\partial x_i}\right|_n = 0,\ \left.\frac{\partial c_i}{\partial x_j}\right|_n = 0, \tag{11}$$

where n and t are the normal and tangent directions in relation to the wall.

To study the processes in a separating diffusion apparatus, the system of equations (1)–(10) is solved using the finite volume method and a special Flow Simulation package built into the SolidWorks engineering design system. The formulation of the problem included setting the initial and boundary conditions, which ensured the accuracy and reliability of the results obtained.

To confirm the effectiveness of the described mathematical model, the results of a numerical simulation of convective flows in a binary gas mixture at different inclination angles of the diffusion channel are presented in [18]. The calculation results are in qualitative agreement with the experimental data for isothermal binary gas mixtures.

The outcomes of the numerical simulations conducted on a quaternary gaseous mixture

Figure 1 shows a model of a representative two-flask apparatus simulated using SolidWorks [19]. This model for various forms of the diffusion channel can be used to simulate diffusion and convective mass transfer, as well as various features that arise when gases are mixed. The calculations were carried out for a flat vertical channel. The considered flat channel had the following characteristics: length L = 0.165 m, thickness $a = 6 \cdot 10^{-3}$ m, and width $b = 30 \cdot 10^{-3}$ m. A non-dimensional mesh with the following dimensions 8 × 34 × 8 was used in the computations.

Our focus is on studying the mixing process for a system that consists of helium, argon, and carbon dioxide that is diffusing into pure nitrogen. During the numerical simulation, the top flask of the diffusion cell was stocked with a mixture comprising of 0.36 He + 0.33 Ar + 0.31 CO_2, whereas the bottom flask was stocked with pure nitrogen. Before the chemical element, its concentration in mole fractions is indicated. The pressure and temperature of the experiment were p_{abs} = 0.6 MPa and T = 298.0 K, and the mixing time interval was 0 – 180 s.

For argon in the quasi-stationary mixing mode, at integrated relationship is obtained that describes the change in its concentration with time. This dependence is shown in Figure 2. In accordance with Figure 2, the amount of argon diffused for 120 s is maximum. During this time, the amount of transferred argon has changed by more than 8 times that is not observed during diffusion. Apparently, under these conditions, the mechanism of the preferential migration of the components with the maximal molar mass is implemented. Subsequent growth of the mixing time does not lead to a synergistic increase in the transfer intensity, which allows assuming that the current has a convective type of flow. A similar behavior is observed for carbon dioxide.

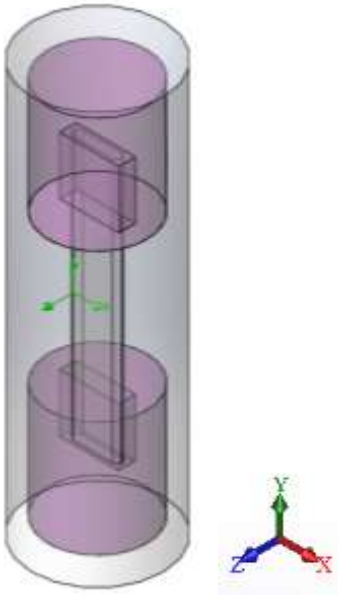

Figure 1. Pattern of a diffusive unit

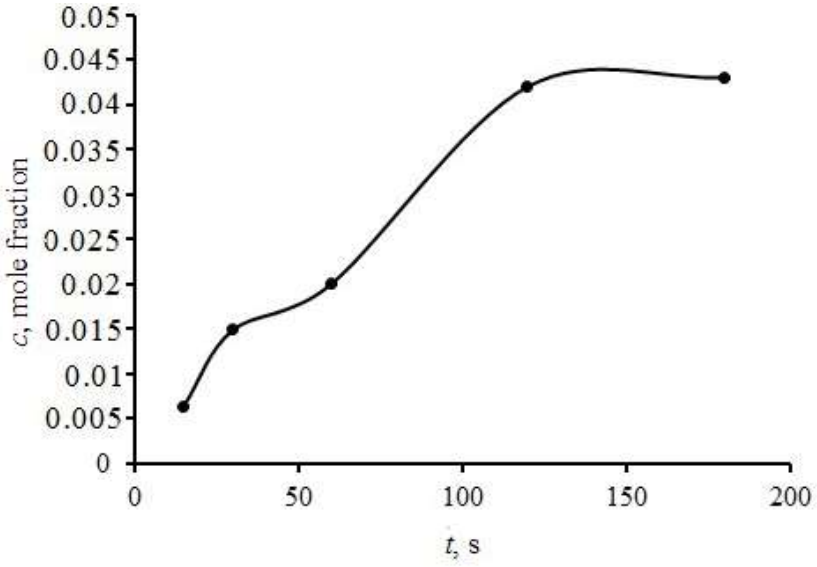

Figure 2. Time-dependence of the amount of argon diffused into nitrogen

Figures 3-7 display how the average concentration of carbon dioxide varies according to the channel altitude and how the concentrations are distributed at different times. Calculations have shown that an analogous picture is realized for argon.

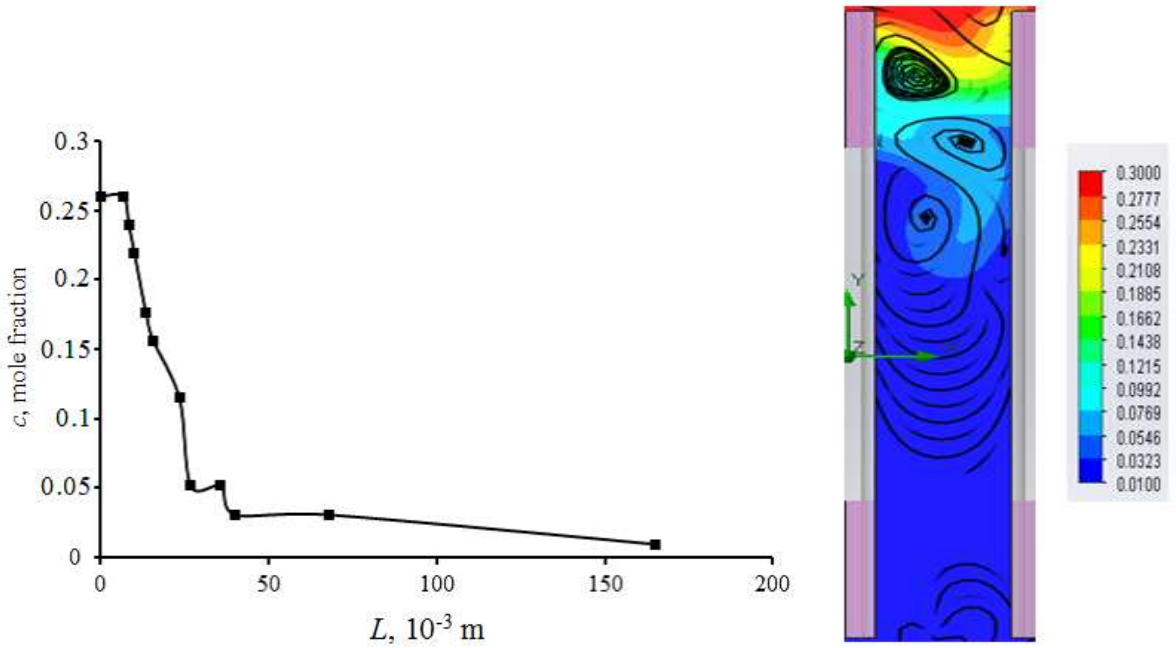

(a) (b)

Figure 3. Length-dependence of the amount of carbon dioxide (a) and pattern displaying the behavior of carbon dioxide (b) for the time moment of 15 s

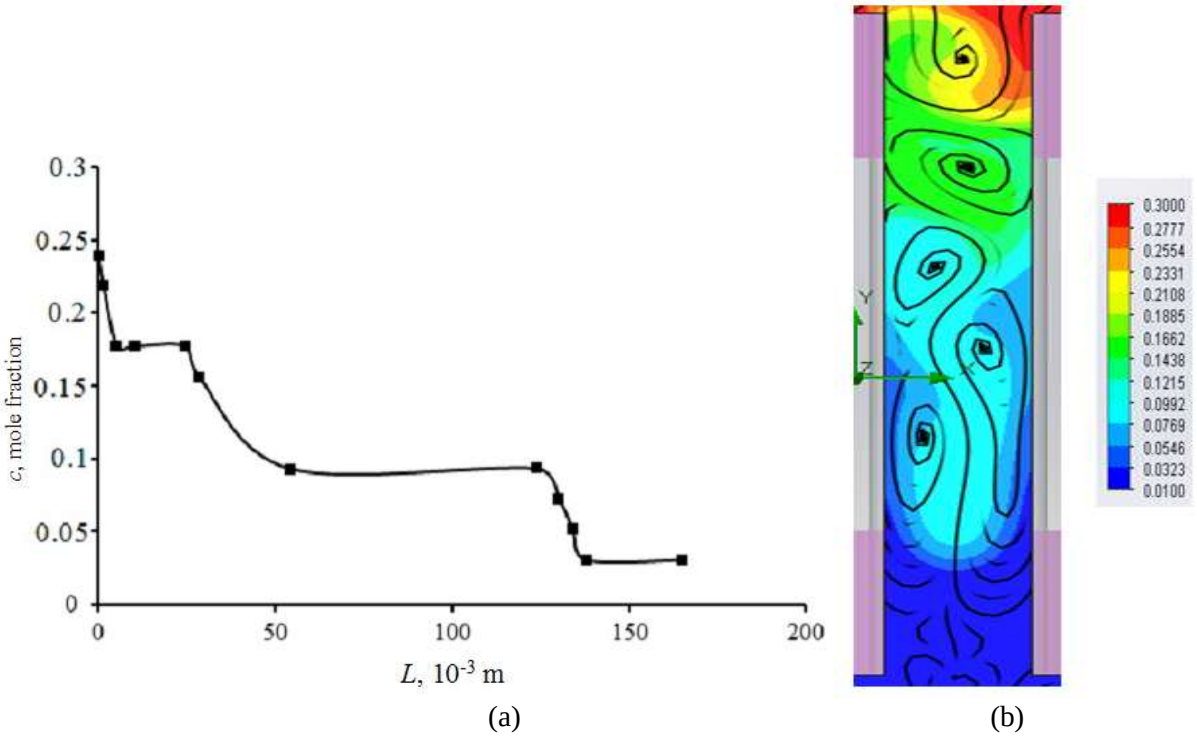

(a) (b)

Figure 4. Length-dependence of the amount of carbon dioxide (a) and pattern displaying the behavior of carbon dioxide (b) for the time moment of 30 s

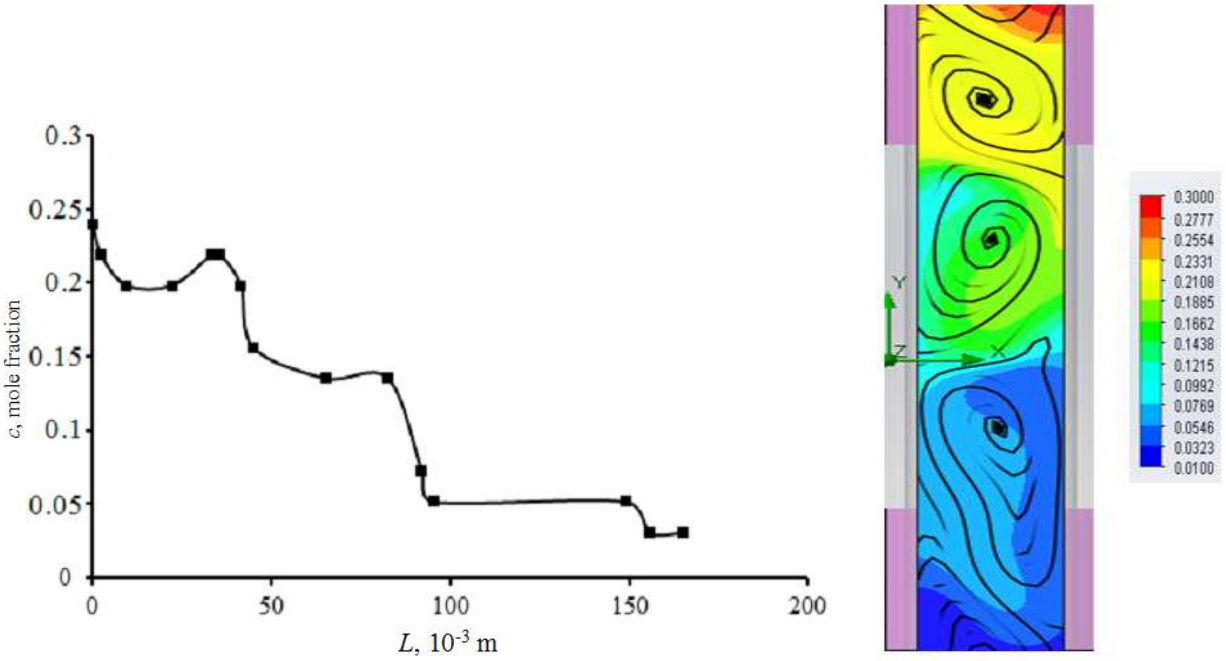

(a) (b)

Figure 5. Length-dependence of the amount of carbon dioxide (a) and pattern displaying the behavior of carbon dioxide (b) for the time moment of 60 s

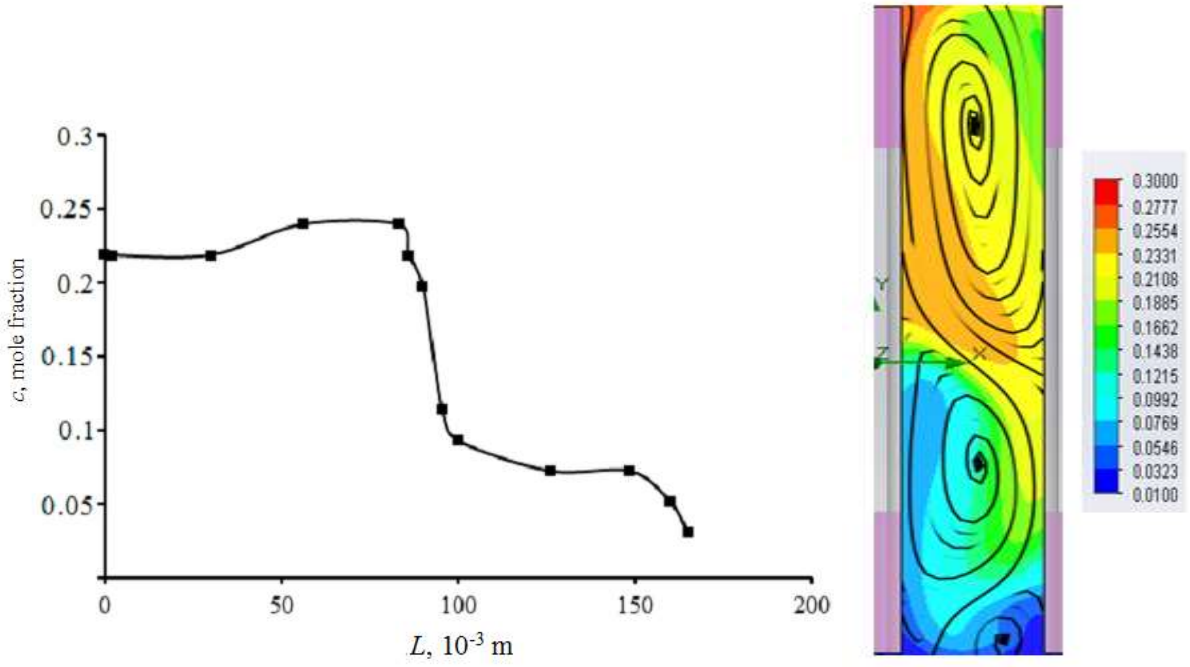

(a) (b)

Figure 6. Length-dependence of the amount of carbon dioxide (a) and pattern displaying the behavior of carbon dioxide (b) for the time moment of 120 s

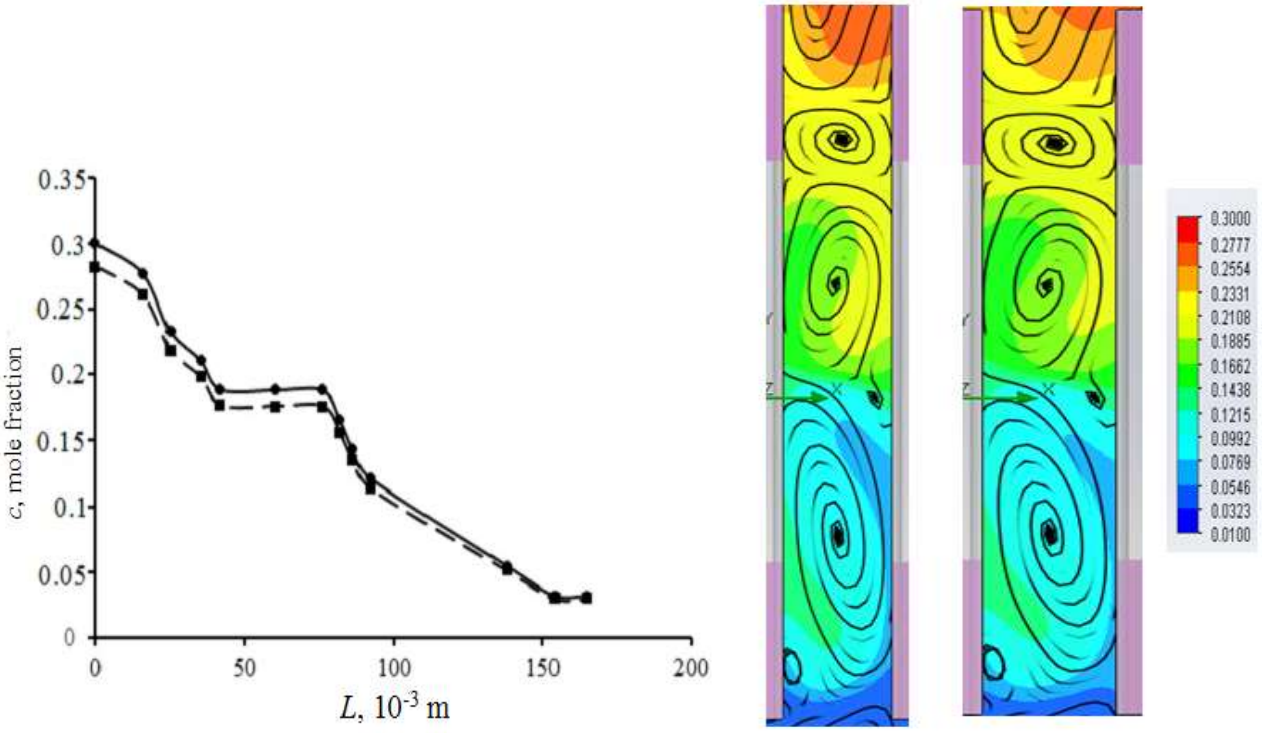

(a) (b) (c)

Figure 7. Length-dependence (a) of the amount of carbon dioxide (■) and argon (●), and pattern displaying the behavior of carbon dioxide (b) and argon (c) for the time moment of 180 s

According to Figure 3, at a length of 0.0268 – 0.0357 m of the diffusion channel, there is a region in which the CO_2 concentration is 0.051 mole fractions. On the diagram, this concentration corresponds to the formation of a vortex, which is blurred along the channel length. An increase in time to t = 30 s (Fig. 4) and t = 60 s (Fig. 5) corresponds to the situation when several regions with a constant content of CO_2 concentration are formed in the channel. In this case, the number of vortices formed along the length of the channel decreases from four to two. At the time t = 120 s (Fig. 6), at a length of the diffusion channel of 0.056 – 0.083 m, the greatest transfer of carbon dioxide concentration is observed, which corresponds to the formation of two competing regions on the diagrams, i.e., developed convective flow. A further increase in time to t = 180 s (Fig. 7) is characterized by the behavior of the concentrations of heavy components similar to that shown in Figure 3. However, the difference lies in the fact that the concentrations remain constant at a greater distance along the length of the diffusion channel. The appearance of a new convective regime is indicated by an increase in vortices along the length of the channel.

The following unique features of convective mass transfer that occur in a quaternary gaseous system can be discovered through the study of the obtained data:

1 The non-linear distribution of the concentrations of the components with the maximal molar mass in a quaternary gaseous system indicates the possibility of an instability of the mechanical equilibrium of the system, which leads to a transition from the diffusion mode of mixing to the convective one.

2 The appearance of closed streamlines should be taken into account to determine if the mixing mode has changed. A chaotic formation structure is observed during the initial stages of mixing. Vortices of different sizes gradually develop, and their interaction can lead to the appearance of a pulsating mixing mode.

3 The initial stage of mixing results in the preferential migration of components, which is explained by an increase in the concentration of gases with the maximal molar mass. This process can be due to the presence of large-scale vortices, which facilitate the forward movement of these components. Their subsequent disappearance leads to the stabilization of the transfer.

Conclusions

Numerical modeling of the partial mass transfer of the four-component mixture 0.36 He + 0.33 Ar + 0.31 CO_2 – N_2 at elevated pressure and room temperature showed that the variation in the diffusion coefficients of the components might cause a shift in the "diffusion – convection" modes in the system. Convective instability in the mixture arises because the distribution of concentrations of components with higher molecular weight along the diffusion channel is not linear. The main indicator of the transfer through the separation boundary of kinetic regimes is the appearance of closed streamlines. In their presence, the diffusion regime loses stability. For the considered mixture under given thermophysical conditions, the time of stability loss is estimated to be on the order of a second. Priority transmission of the component with the largest molar mass is feasible with unstable mixing. The emergence of large-scale vortices is connected with this regime.

Acknowledgements

The Committee of Science of the Ministry of Science and Higher Education of the Republic of Kazakhstan provided financial assistance for this work (project AP14870237).

References

1 Dil'man V.V. Specific Features of Multicomponent Diffusion / V.V. Dil'man, O.A. Kashirskaya, V.A. Lotkhov // Theoretical Foundations of Chemical Engineering. — 2010. — Vol. 44, No. 4. — P. 379-383. https://doi.org/10.1134/S0040579510040032

2 Kaminskii V.A. Special Modes of Three-Component Diffusion in gases / V.A. Kaminskii // Russian Journal of Physical Chemistry A. — 2011. — Vol. 85, No. 12. — P. 2203-2208. https://doi.org/10.1134/S0036024411120156

3 Dil'man V.V. Instability in Unsteady-state Evaporation of Binary Solutions into an Inert Gas / V.V. Dil'man, D.A. Lipatov, V.A. Lotkhov, V.A. Kaminskii // Theoretical Foundations of Chemical Engineering. — 2005. — Vol. 39, No. 6. — P. 566-572. https://doi.org/10.1007/s11236-005-0118-0

4 Kosov V.N. Separation of components during isothermal mixing of ternary gas systems under free-convection conditions / V.N. Kosov, V.D. Seleznev, Yu.I. Zhavrin // Technical Physics. — 1997. — Vol. 42, No. 10. — P. 1236-1237. https://doi.org/10.1134/1.1258905

5 Aleksandrov O.E. The exact solution of the equation for diffusion of a three-component mixture through a capillary / O.E. Aleksandrov // Technical Physics. — 2001. — Vol. 46, No. 11. — P. 1367–1370. https://doi.org/10.1134/1.1418497

6 Kosov V.N. Inversion of the density gradient and the diffusion "gate" in isothermal mixing of gases / V.N. Kosov, Y.I. Zhavrin, V.D. Seleznev // Technical Physics. — 1998. — Vol. 43, No. 5. — P. 488–492. https://doi.org/10.1134/1.1259026

7 Cherkasov S.G. Limitations of the Boussinesq Model on the Example of Laminary Natural Convection of Gas between Vertical Isothermal Walls / S.G. Cherkasov, A.V. Anan'ev, L.A. Moiseeva // High Temperature. — 2018. — Vol. 56, No. 6. — P. 878–883. https://doi.org/10.1134/S0018151X18060081

8 Kosov V.N. Instability of mechanical equilibrium during diffusion in a three-component gas mixture in a vertical cylinder with a circular cross section / V.N. Kosov, O.V. Fedorenko, Y.I. Zhavrin, V. Mukamedenkyzy // Technical Physics. — 2014. — Vol. 59, No. 4. — P. 482–486. https://doi.org/10.1134/S1063784214040161

9 Kosov V.N. Changing Diffusion–Convection Modes in Ternary Mixtures with a Diluent Gas / V.N. Kosov, O.V. Fedorenko, M.K. Asembaeva, V. Mukamedenkyzy // Theoretical Foundations of Chemical Engineering. – 2020. – Vol. 54, No. 2. – P. 289–296. https://doi.org/10.1134/S0040579520020086

10 Kudinov A.N. Features of selective mass transfer in hybrid membrane-sorption systems / A.N. Kudinov, I.M. Kurchatov, N.I. Laguntsov // Theoretical Foundations of Chemical Engineering. — 2014. — Vol. 48, No. 4. — P. 352–359. https://doi.org/10.1134/S0040579514040204

11 Семенов А.П. Извлечение процесса пропан-бутановой фракции из углеводородных газовых смесей с помощью процесса образования газовых гидратов / А.П. Семенов, А.С. Викторов, А.Б. Берберов, А.С. Волков, В.А. Винокуров // Технологии нефти и газа. — 2012. — Т. 82. № 5. — С. 24–32.

12 Budd P.M. Gas separation membranes from polymers of intrinsic micro porosity / P.M. Budd, K.J. Msayb, C.E. Tattershal, B.S. Ghanem, K.J. Reynolds, N.B. McKeown, D. Fritsch // Journal of Membrane Science. — 2005. — Vol. 251, No. 1-2. — P. 263-269. https://doi.org/10.1016/j.memsci.2005.01.009

13 Liu S.L. Recent progress in the design of advanced PEO-containing membranes for CO_2 removal / S.L. Liu, L. Shao, M.L. Chua, C.H. Lau, H. Wang, S. Quan // Progress in Polymer Science. — 2013. — Vol. 38, No. 7. — P. 1089-1120. https://doi.org/10.1016/j.progpolymsci.2013.02.002

14 Демин В.А. Конвективные сепараторы / В.А. Демин // Прикладная физика. — 2013. — № 4. — С. 60–67. — [Электронный ресурс].— Режим доступа: https://applphys.orion-ir.ru/appl-13/13-4/PF-13-4-60.pdf

15 Malyshkina M.M. The procedure for investigation of the efficiency of purification of natural gases in a supersonic separator / M.M. Malyshkina // High Temperature. — 2010. — Vol. 48, No. 2. — P. 244–250. https://doi.org/10.1134/S0018151X10020161

16 Алямовский А.А. Solid Works 2007/2008. Компьютерное моделирование в инженерной практике / А.А. Алямовский, А.А. Собачкин, Е.В. Одинцов, А.И. Харитонович, Н.Б. Пономарев. — СПб.: БХВ-Петербург, 2008. — 1040 с.

17 Shih T.-H. A new k-ε eddy-viscosity model for high Reynolds number turbulent flows / T.-H. Shih, W.W. Liou, A. Shabbir, Z. Yang, J. Zhu // Computers & Fluids. — 1995. — Vol. 24, No 3. — P. 227-238. http://dx.doi.org/10.1016/0045-7930(94)00032-T

18 Косов В.Н. Численное моделирование возникновения конвективных течений при квазистационарном смешении в бинарных газовых смесях при различных углах наклона диффузионного канала / В.Н. Косов, С.А. Красиков, О.В. Федоренко // Вестн. Моск. гос. обл. ун-та. Сер. Естественные науки. — 2018. — № 2. — С. 134–142.

19 Nezovitina N.A. Dependence of the thermodiffusion constant of a mixture of two gases on the addition of a third gas to it / N.A. Nezovitina, A.F. Bogatyrev, O.A. Makeenkova // J. Eng. Phys. and Thermophys. — 2016. — Vol. 89, No. 3. — P. 733-740. https://doi.org/10.1007/s10891-016-1433-5

О.В. Федоренко, В.Н. Косов, С.А. Красиков, М. Жанели, Т. Сейдаз

Төрт компонентті газ жүйелеріндегі көп компонентті масса тасымалдау режимдерін сандық модельдеу

Төрт компонентті He + Ar + CO2 – N2 газ қоспасының құрамына кіретін және басқа компоненттермен салыстырғанда ең ауыр болып табылатын аргон және қостотықты көмірқышқыл газы үшін диффузиялық каналдың әртүрлі нүктелерінде және уақытша аралықтардағы осы компоненттердің концентрациясы тәртібінің өзгеру графиктері берілген. Қарастырылып отырған төрт компонентті қоспадағы конвективті ағындарды модельдеу үшін *SolidWorks* инженерлік жобалау жүйесіне енгізілген *Flow Simulation* компьютерлік пакеті пайдаланылды. Теңдеулер стандартты $k-\varepsilon$ турбуленттілік моделін қолданып, сондай-ақ бастапқы және шекаралық шарттарды белгілей отырып, ақырлы көлем әдісімен шешілді. Алынған үлестірулер уақыт бойынша да, диффузиялық каналдың ұзындығы бойынша да сызықтық емес өзгеретіні көрсетілген. Концентрацияны үлестірудің бұл сызықтық емес әрекеті механикалық тепе-теңдіктің тұрақсыздығымен байланысты, бұл өз кезегінде жүйенің диффузиялық процестен конвективті процеске ауысуына әкеледі. Қарастырылып отырған ауыр компоненттер үшін концентрацияның ең үлкен өзгерісі 120 с ішінде байқалады, бұл эпюраларда екі бәсекелес аймақтың пайда болуына, яғни дамыған конвективті ағынға сәйкес келеді. Сандық эксперимент ұзақтығының одан әрі ұлғаюы ең үлкен молекулалық салмағы бар компоненттердің концентрациясының шамалы өзгеруіне әкеледі, бұл қоспаны ауыр компонентпен байыту эффектісіне сәйкес. Концентрациялардың үлестіру эпюраларындағы ток сызықтарын талдау, каналдың ұзындығы бойынша әр түрлі масштабтағы өзара әрекеттесетін құйындар түзіліп, пульсациялық араластыру режиміне әкелетінін көрсетті. Кең ауқымды құйындардың болуы ең үлкен молекулалық салмағы бар компоненттің басым тасымалдануына әкелетіні анықталды.

Кілт сөздер: газ қоспалары, диффузия, тұрақсыздық, конвекция, концентрацияның үлестіруі, компоненттердің қалыптан тыс бөлінуі, сандық модельдеу, ақырлы көлем әдісі.

О.В. Федоренко, В.Н. Косов, С.А. Красиков, М. Жанели, Т. Сейдаз

Численное моделирование режимов многокомпонентного массопереноса в четырехкомпонентных газовых системах

Для аргона и двуокиси углерода, входящих в состав четырехкомпонентной газовой смеси He + Ar + CO_2 – N_2 и являющихся наиболее тяжелыми по сравнению с другими компонентами, приведены графики изменения поведения концентрации этих компонентов в различных точках диффузионного канала и временных интервалах. Для моделирования конвективных течений в рассматриваемой четырехкомпонентной смеси использовался компьютерный пакет Flow Simulation, входящий в систему инженерного проектирования SolidWorks. Уравнения решаются методом конечных объемов с использованием стандартной *k–ε* модели турбулентности и с заданием начальных и граничных условий. Показано, что полученные распределения изменяются нелинейно как по времени, так и по длине диффузионного канала. Такое нелинейное поведение распределений концентраций связано с неустойчиво-

стью механического равновесия, что, в свою очередь, приводит к переходу системы от диффузионного процесса к конвективному. Установлено, что для рассматриваемых тяжелых компонентов наибольшее изменение концентрации наблюдается в течение 120 с, что соответствует образованию на эпюрах двух конкурирующих областей, то есть развитому конвективному течению. Дальнейшее увеличение продолжительности численного эксперимента приводит к незначительному изменению концентрации компонентов с наибольшим молекулярным весом, что соответствует эффекту обогащения смеси тяжелым компонентом. Анализ линий тока на эпюрах распределений концентраций показал, что по длине канала образуются взаимодействующие между собой вихри различных масштабов, приводящие к пульсационному режиму смешения. Установлено, что наличие крупномасштабных вихрей обусловливает приоритетный перенос компонентов с наибольшим молекулярным весом.

Ключевые слова: газовые смеси, диффузия, неустойчивость, конвекция, распределение концентрации, аномальное разделение компонентов, численное моделирование, метод конечных объемов.

References

1 Dil'man, V.V., Kashirskaya, O.A., & Lotkhov, V.A. (2010). Specific Features of Multicomponent Diffusion. *Theoretical Foundations of Chemical Engineering*, *44*(4), 379-383.

2 Kaminskii, V.A. (2011). Special Modes of Three-Component Diffusion in gases. *Russian Journal of Physical Chemistry A*, *85*(12), 2203-2208.

3 Dil'man, V.V., Lipatov, D.A., Lotkhov, V.A., & Kaminskii, V.A. (2005). Instability in Unsteady-state Evaporation of Binary Solutions into an Inert Gas. *Theoretical Foundations of Chemical Engineering*, *39*(6), 566-572.

4 Kosov, V.N., Seleznev, V.D., & Zhavrin, Yu.I. (1997). Separation of components during isothermal mixing of ternary gas systems under free-convection conditions. *Technical Physics*, *42*(10), 1236–1237.

5 Aleksandrov, O.E. (2001). The exact solution of the equation for diffusion of a three-component mixture through a capillary. *Technical Physics*, *46*(11), 1367–1370.

6 Kosov, V.N., Zhavrin, Y.I., & Seleznev, V.D. (1998). Inversion of the density gradient and the diffusion “gate” in isothermal mixing of gases. *Technical Physics*, *43*(5), 488–492.

7 Cherkasov, S.G., Anan’ev, A.V., & Moiseeva, L.A. (2018). Limitations of the Boussinesq Model on the Example of Laminary Natural Convection of Gas between Vertical Isothermal Walls. *High Temperature*, *56*(6), 878–883.

8 Kosov, V.N., Fedorenko, O.V., Zhavrin, Y.I., & Mukamedenkyzy, V. (2014). Instability of mechanical equilibrium during diffusion in a three-component gas mixture in a vertical cylinder with a circular cross section. *Technical Physics*, *59*(4), 482–486.

9 Kosov, V.N., Fedorenko, O.V., Asembaeva, M.K., & Mukamedenkyzy, V. (2020). Changing Diffusion–Convection Modes in Ternary Mixtures with a Diluent Gas. *Theoretical Foundations of Chemical Engineering*, *54*(2), 289–296.

10 Kudinov, A.N., Kurchatov, I.M., & Laguntsov, N.I. (2014). Features of selective mass transfer in hybrid membrane-sorption systems. *Theoretical Foundations of Chemical Engineering*, *48*(4), 352–359.

11 Semenov, A.P., Viktorov, A.S., Berberov, A.B., Volkov, A.S., & Vinokurov, V.A. (2012). Izvlechenie protsessa propan-butanovoi fraktsii iz uglevodorodnykh gazovykh smesei s pomoshchiu protsessa obrazovaniia gazovykh gidratov [Extraction of the process of propane-butane fraction from hydrocarbon gas mixtures using the process of formation of gas hydrates]. *Tekhnologii nefti i gaza — Technologies of oil and gas*, *82* (5), 24–32 [in Russian].

12 Budd, P.M., Msayb, K.J., Tattershal, C.E., Ghanem, B.S., Reynolds, K.J., McKeown, N.B., & Fritsch, D. (2005). Gas separation membranes from polymers of intrinsic micro porosity. *Journal of Membrane Science*, *251*(1-2), 263-269.

13 Liu, S.L., Shao, L., Chua, M.L., Lau, C.H., Wang, H., & Quan, S. (2013). Recent progress in the design of advanced PEO-containing membranes for CO_2 removal. *Progress in Polymer Science*, *38*(7), 1089-1120.

14 Demin, V.A. (2013). Konvektivnye separatory [Convective separators]. *Prikladnaia fizika — Applied Physics*, *4*, 60–67 [in Russian].

15 Malyshkina, M.M. (2010). The procedure for investigation of the efficiency of purification of natural gases in a supersonic separator. *High Temperature*, *48*(2), 244–250.

16 Alyamovsky, A.A., Sobachkin, A.A., Odintsov, E.V., Kharitonovich, A.I., & Ponomarev, N.B. (2008). *Kompiuternoe modelirovanie v inzhenernoi praktike [Computer modeling in engineering practice]*. Saint Petersburg: BHV-Petersburg [in Russian].

17 Shih, T.-H., Liou, W.W., Shabbir, A., Yang, Z., & Zhu, J. (1995). A new k-ε eddy-viscosity model for high Reynolds number turbulent flows. *Computers & Fluids*, *24*(3), 227-238.

18 Kosov, V.N., Krasikov, S.A., & Fedorenko, O.V. (2018). Chislennoe modelirovanie vozniknoveniia konvektivnykh techenii pri kvazistatsionarnom smeshenii v binarnykh gazovykh smesiakh pri razlichnykh uglakh naklona diffuzionnogo kanala [Numerical modeling of the occurrence of convective flows during quasi-stationary mixing in binary gas mixtures

at different angles of inclination of the diffusion channel]. *Vestnik Moskovskogo gosudarstvennogo oblastnogo universiteta. Seriia Yestestvennye nauki — Bulletin of the Moscow State Regional University. Series of "Natural Sciences"*, 2, 134–142 [in Russian].

19 Nezovitina, N.A., Bogatyrev, A.F., & Makeenkova, O.A. (2016). Dependence of the thermodiffusion constant of a mixture of two gases on the addition of a third gas to it. *J. Eng. Phys. and Thermophysics*, *89*(3), 733-740.

DOI 10.31489/2023PH4/50-56

UDC538.915

A.M. Sultanov[1], A.A. Abdukarimov[1*], M.Z. Kufian[2]

[1]Namangan Engineering and Technology Institute, Namangan, Uzbekistan;
[2]University of Malaya, Kuala lumpur. Malaysia.
[*]Corresponding authors e-mail: abdullaziz.abdukarimov@ mail.ru

Development of technology for creating high-voltage $p^0 – n^0$ junctions based on GaAs

An optimal solution has been found to the problem of obtaining p0-n0 junctions based on lightly doped GaAs layers with high values of electrical parameters and specified thicknesses of base layers to create ultra-fast high-voltage pulsed three-electrode switches with a photon injection mechanism of minority charge carriers. A technology has been developed for the formation of high-voltage, powerful subnano-second photonic injection switches based on gallium arsenide and its solid solutions. The dependence of the current rise time, switching voltage and switching stability relative to the control pulse of high-voltage photonic injection switches in a wide current and frequency mode of their operation, its sensitivity to various external influences, as well as dependence on the thickness of the p0-layer, on the transmission coefficient, on breakdown voltage U_{probe} of the high-voltage p^0-n^0 junction. The carried out studies and the obtained results indicate the prospects of using the developed high-voltage pulsed semiconductor devices in picosecond optoelectronics for pumping high-power laser and LED structures.

Keywords: Liquid-phase epitaxy (LPE), heterostructures, high-voltage p^0-n^0 transition, Hall effect, background doping, solution-melt.

Introduction

As is known, to create subnano- and picosecond photon-injection switches based on GaAs and AlGaAsheterostructures, the main need is:

1. Determination of the optimal temperature-time regime for the reproducible production of an n^+-p^0-n^0 transistor structure with a high-voltage p^0-n^0 junction, in liquid-phase epitaxy (LPE), formed due to background doping with specified parameters and the creation of subnano-second powerful switches based on them.

2. Study of the influence of the main technological factors: the temperature of the onset of crystallization tn.cr., the thickness of the solution-melt h, the hydrogen flow rate F, the static turn-on voltages U_{on}, the control current I_{up}., and the dynamic parameters ― current rise time, turn-on delay time relative to the control impulse, the stability of switching-on-switching structures [1-5].

Conducting research on the creation of high-power high-voltage switching device structures based on lightly doped gallium arsenide is associated with the need to search for alternative principles for switching electrical power in the subnano- and picosecond time ranges. Since modern laser, accelerator and location technology, thermonuclear energy, picosecond spectroscopy of liquids and solids, topography, radio engineering, digital technology and a number of areas of converter technology require the creation of semiconductor switches of this power range, which have the traditional advantages of semiconductor devices: long service life, reliability, high efficiency and, which is extremely important for a number of applications, resistance to external influences (radiation, temperature) and instant readiness for operation.

Due to the need for location technology, defense, digital technology, two new switching principles have been developed ― using a control plasma layer and using a delayed shock-ionization wave, which made it possible to increase the power switched by devices in the nanosecond range by almost two to three orders of magnitude and in the picosecond range by almost four orders of magnitude [6–8].

The speed, the magnitude of the absolute and specific power switched by semiconductor devices largely depends on the processes of filling the region with electron-hole plasma, which has a high resistance in the initial state and blocks the applied external voltage. Such a region is the region of the space charge, depleted by the strong field of the reverse-shifted p-n junction.

Powerful semiconductor devices developed on the basis of silicon, such as pulse sharpeners of diode, transistor and thyristor types, operating on the principle of switching using a delayed shock-ionization wave, required the development of new circuitry, a new direction of research using new materials, primarily GaAs and heterostructures on its basis [9, 10].

Currently, epitaxial methods for obtaining single-crystal layers are widely used for the manufacture of various semiconductor devices. Epitaxial growth methods make it possible to combine in time the process of crystallization of a semiconductor material and the production of a device structure. Gas-transport, molecular-beam and liquid-phase epitaxy have received the main distribution.

When developing high-voltage diodes, transistors and thyristors, it is necessary to use GaAs with a concentration of the main charge carriers of~10^{15} cm^{-3}or less. A fairly common technology for obtaining such a material is LPE, carried out in a quartz container with forced cooling of a solution-melt of GaAs in Ga [11–13]. This method, in comparison with other methods for growing epitaxial layers, makes it possible to obtain efficiently injecting junctions. This is due to the fact that, when GaAs is grown by this method, the internal quantum yield of radioactive recombination is much higher than when GaAs is grown from stoichiometric melts [14, 15]. This opens up the possibility of an unconventional approach to the design of high-voltage devices based on heterostructures. In addition, this method has the following advantages over gas-transport and molecular epitaxy: simplicity of equipment, higher growth rates, the possibility of reducing the impurity background, etc. The physicochemical foundations of LPE are well described in a number of monographs [16–18].

Methods

LPE is an oriented crystallization of single-crystal layers of semiconductor materials from solutions of these materials. There are several methods of epitaxial growth from a solution-melt: growth from a limited volume and growth from a semi-limited volume of a solution-melt. The method of growing epitaxial layers from a limited volume of a solution-melt has received the main distribution.

Under conditions of crystallization from limited volumes of solutions-melts, both a significantly higher reproducibility of obtaining layers with a given thickness is achieved compared to crystallization from semi-limited volumes, as well as a higher degree of their planarity. In addition, the growth of layers from a limited volume of a solution-melt makes it possible to control the crystallization rates and conduct the process under conditions closer to quasi-equilibrium.

Thanks to the development of technology for obtaining high-voltage p-n junctions based on lightly doped GaAs, it became possible to create pulsed transistors and thyristors based on GaAs-AlGaAsheterostructures. Studies have shown the prospect of using photon-injection mechanisms of coupling between p-n junctions in high-voltage multilayer structures, the possibility of switching high powers by three-electrode semiconductor devices in the subnano-second range of durations [9].

Therefore, the improvement of the main parameters and characteristics (increasing the operating voltage, improving the speed, reproducibility and dependence of the temperature effect, radiation) of switches is associated with an understanding of the technological processes for the formation of high-voltage p-n structures, the choice of the optimal geometry and the search for new designs [10, 13].

The analysis of the literature data shows [1, 13, 16-19] that the production of lightly doped GaAs layers and the formation of high-voltage p-n junctions in the process of growth have not been clarified, the nature of residual impurities is not entirely clear, the influence of technological factors on the electrical properties has not been studied, which makes it difficult to create high-voltage switches with subnano- and picosecond speed.

The static and impulse characteristics of such device structures obtained under various technological conditions have not been studied at all.

The aim of our work is to obtain high-voltage p-n junctions based on lightly doped GaAs layers, to study the influence of technological factors on their main dynamic parameters and characteristics, to create powerful photon-injection pulse switches based on them with subnano- and picosecond speed, to elucidate the possibility of increasing the power of the switched gallium arsenide transistors and thyristors in the subnano-second range.

Experimental

The proposed technologies for obtaining high-voltage p-n junctions based on lightly doped GaAs allowed the creation of pulsed transistors and thyristors based on GaAs-AlGaAsheterostructures. We have optimized technologies for obtaining high-voltage p-n junctions based on lightly doped GaAs layers and creating subnano- and picosecond speed photon-injection switches based on the principle of photon transfer of no equilibrium charge carriers. The main attention is paid to the features of obtaining device structures, the influence of technological factors on the static and dynamic parameters of switching structures in the mode of high currents and voltages.

Liquid-phase epitaxy is the method of growing epitaxial layers from a limited volume of a solution-melt to obtain and fabricate device structures. Under conditions of crystallization from limited volumes of solutions-melts, both a significantly higher reproducibility of obtaining layers with a given thickness is achieved compared to crystallization from semi-limited volumes, as well as a higher degree of their planarity. In addition, this method makes it possible to control the crystallization rates, conduct the process under conditions closer to quasi-equilibrium, and obtain "pure" and doped layers of high-quality p-n junctions and multilayer device structures with specified electrophysical parameters with sufficiently high reproducibility.

The main problem in creating subnano- and picosecond switches based on GaAs is to obtain layers with a given thickness of the base regions and a low dopant concentration. A study was made of the influence of technological factors on the properties of epitaxial layers and p^0-n^0 junctions.

To ensure the optimal impurity distribution profile in a quartz container, from a limited volume of an arsenic melt solution in gallium on n^+ - GaAs substrates oriented in the [100] plane, p^0- and n^0- GaAs layers with specified thicknesses were grown, which are the basic regions of the structure. The position of the p-n transition, the concentration profile in the p^0- and n^0-layers, the thickness of the p^0-region in depending on the conditions for the formation of an impurity background in the solution-melt were obtained in advance planned limits. The lifetime of minority charge carriers (NCC) is an important dynamic characteristic of a semiconductor device. In lightly doped GaAs, the NCC lifetime is determined mainly by the concentration of deep levels. Its value in lightly doped regions of transistor and thyristor structures was determined by measuring the dissipation time of the charge accumulated in these regions and was 50–500 ns. Such a scatter in the values of the CC lifetime is due to the concentration and capture cross section of uncontrollably introduced recombination centers. The concentration of carriers in the p0- and n0- regions ranged from 1.0 10^{15} cm^{-3} to $0.1 \cdot 10^{15}$ cm^{-3}, the mobility of charge carriers was, $\mu_n = (5 - 6) \cdot 10^3$ cm^2 / V·s in the n^0-layer and μ_p = (400 – 450) cm^2/V·s at 300 K. The charge carrier mobilities were determined by measuring the Halle effect in the grown epitaxial layers [19].

The thickness of the n^0-layer, exceeding the dimensions of the space-charge layer at zero mixing of the p-n junction, was (30–35) μm and provided the possibility of effective separation of electron-hole pairs created by absorbed radiation. The control of the position of the p-n transition, the estimation of the size of the space charge region was carried out by a method based on the observation of the electro-optical effect in gallium arsenide during the passage of plane polarized infrared light through the crystal.

For the efficient operation of thyristors and transistors, the thickness of the p^0-part should be as small as possible, therefore, for them manufacturing can only be used n^+- p^0-n^0 structures with certain thicknesses p^0 - areas that provide high transfer coefficient values. Defined temperature dependence of p^0-layer on temperature the beginning of crystallization (Fig. 1), and coefficients segregation of fine acceptor and donor impurities the level of concentration and the degree of compensation [19].

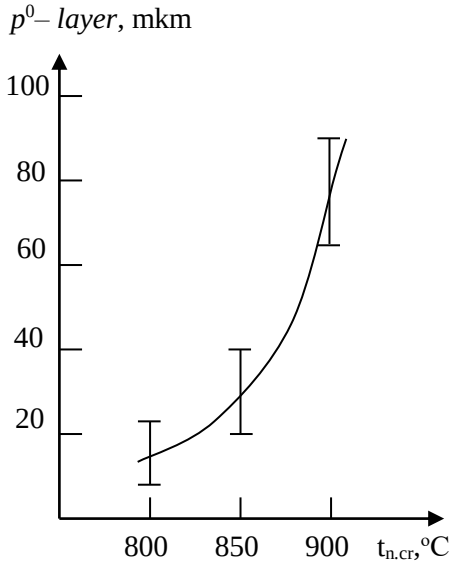

Figure 1. DependenceK of the thickness of the p^0-layer on temperature.

In order to optimize the growth technology and the design of thyristors, the dependences of the transfer coefficients of structures on the thickness of the low-resistance part of the p^0-region and on temperature were studied (Fig. 2).

It can be seen that the transfer coefficient α of transistor n^+- p^0- n^0 structures drops sharply already at a thickness p^0 = 30 μm regardless of the temperature on set crystallization. At the same time, the thickness of the high-resistance parts hi ― areas up to hi-120 μm do not have a significant impact on the value transmission coefficients.

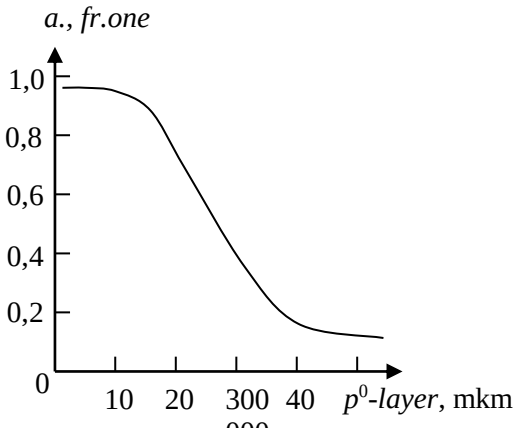

Figure 2. The dependence of the transfer coefficient on the thickness p^0 – layer.

In the region of low values of α and large thicknesses of p^0 ― layer, there is a connection between α and production technology. It can be seen that the choice of liquid phase annealing is preferable, which is justified due to the higher values of the transfer coefficient. This is especially important for technological control of p^0. Figure 3 shows dependence of the transfer coefficient n^+-p^0-n^0 structures on temperature. It can be seen that α decreases with increasing temperature.

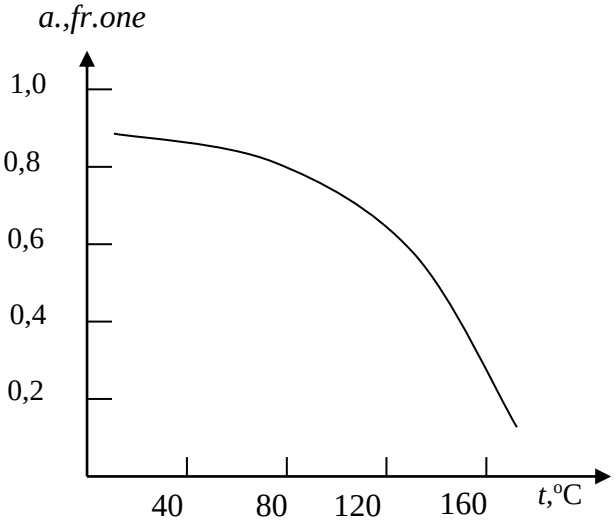

Figure 3. The dependence of the transfer coefficient n^+-p^0-n^0 structure on temperature.

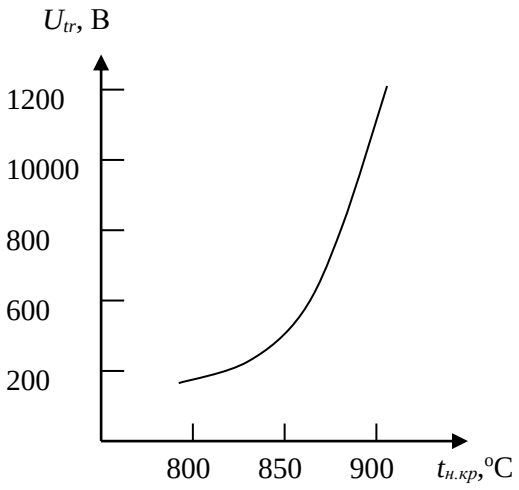

Figure 4. The dependence of $U_{tr.}$ high voltage p^0-n^0 transition on temperature

The decrease in α with increasing temperature can be explained by the temperature dependence of the capture cross section G^A_n and G^B_n, which increase in this temperature range by factors of 5 and 20, respectively.

The effect of temperature at the beginning of crystallization and growth technology on the breakdown voltages ($U_{trial.}$) of a high-voltage p^0-n^0 junction was studied in n^+-p^0-n^0 structures for the possibility of obtaining maximum voltages at the collector junction (Fig. 4). The breakdown voltages increased significantly when p-n junctions turned out to be displaced from the metallurgical boundary and formed during growth. From Figure 4 it can be seen that the values of U_{trial} increase when using a higher temperature, the onset of crystallization. The growth of U_{trial} is explained. A decrease in the carrier concentration gradient in the region of the p-n junction. However, with an increase in the temperature of the onset of crystallization, the transfer coefficient of the resulting n^+-p^0-n^0 structures decreases. In high-voltage p^0-n^0 junctions, the allowable voltages are determined by the impurity concentration gradient in the space charge region (SCR) of the junction and the thickness of the n^0 region. Therefore, the carrier concentration gradient and the thickness of the n^0 region determine the breakdown voltages of the p–n junction. The use of semiconductor structures based on A3B5 is associated with the possibility of a significant increase in performance, which is due to higher mobilities and short lifetimes of minority charge carriers (NCCs). The estimates made by the authors of [19] show that, due to the significantly shorter lifetime of the NCC in gallium arsenide high-voltage devices, it is possible to reduce the total duration of the power switching process by at least an order of magnitude compared to silicon ones. The first experimental results also testify to the high potential capabilities of key devices. For example, for gallium arsenide thyristors of a traditional design, which has three p-n junctions (collector and two emitter) interacting with minor charge carriers, the following record parameters were achieved when switched on through the control circuit: rise time no more than ― 10 ns, turn-on delay relative to the control pulse ― 100 ns at an operating voltage of up to 1000 V and a pulsed current of 100 ― 120 A.

Conclusions

Thus, the above features of obtaining lightly doped layers and p-n junctions based on them show a real possibility of creating high-speed pulse transistors and thyristors. Optimization of the technology for obtaining high-voltage p-n junctions based on lightly doped GaAs layers, development of new principles for the generation and transport of charge carriers in semiconductor structures based on materials with a high proportion of radiative recombination made it possible to obtain high-voltage three-electrode switches with subnano-second turn-on times. The studies carried out and the results achieved indicate broad prospects for the use of gallium arsenide and its solid solutions in the development of high-speed transistors and thyristors with a photon-injection coupling mechanism between p-n junctions.

References

1 Alferov, Zh.I., Grekhov, I.V., & Korolkov, V.I. (1987). Formation of high-voltage voltage drops in the picosecond range on gallium arsenide diodes. *Letters to JTF, Vol. 13*(18), 1089-1093.

2 Alferov, Zh.I., Andreev, V.M., Korolkov, V.I., Portnoy, E.L., & Tretyakov, D.N. (1968). Injection properties of heterojunctions n (AlxGa1-xAs) - p (GaAs). *FTP*, 2.

3 Soldatenkov, F.Yu. (2011). Subnanosecond switches based on heterojunctions in the GaAs (InGaAs)-AlGaAs cuctem. *Doctor's thesis*. Russia. St. Petersburg. Physics-Technical Institute named after A.F. Ioffe.

4 Alferov, Zh.I., & Korolkov, V.I. (1986). Electrically Controlled Three-Electrode High-Voltage Subnanosecond Switches Based on Multilayer GaAs – AlGaAsHeterostructure. *Letters to ZhTF, Vol. 12*(21), 1281-1285.

5 Bowers, H.C. (1967). Space-charge-induced negative resistance in avalanche diodes. IEEE Trans/ EI.Devices, ED. 15.

6 Solovieva, E.V., Milvidsky, M.G., Sabanova, L.D., Berman, L.V., Kolobova, G.A., Sharonov, B.N., Morgulis, L.M., & Surf, J. (1977). The role of impurities and defects in the formation of properties of undoped gallium arsenide layers. *Growth and doping of semiconductor crystals and films,* Part 11, 248-252. Novosibirsk: Science.

7 Ya, L. (1979). Distribution of impurities in large area gallium arsenide structures grown by liquid epitaxy. Materials of the report. At the All-Union Coordinators. *Meeting Sections "Semiconductor. Heterostructures"*, 66-73. Tallinn.

8 Voitovich, V., & Dumanevich, A. (2009). How to replace SiC Schottky diodes. *Power Electronics*, 5.

9 Grekhov, I.V., & Serezhkin, Yu.N. (1980). Avalanche breakdown of the p-n junction in semiconductors. *L., energy*, 151 p.

10 Grekhov, I.V., & Smirnova, I.A. (1985). Semiconductor Powerful Subnanosecond Switches with a Long Hold Time. *Letters to ZhTF, Vol. 11*(15), p. 901.

11 Hur, J.H., Hadirad, P., Hummel, S.G., Dzusko, K.M., Dfrkus, P.D., Fetterman, H.R., & Gundersen, M.A. (1990). GaAs-Based Opto-Thyristor for Pulsed Poneer Applications. *Electron's devices, Vol. 37*(12), 2520-2525.

12 Kyurenyan, A.S. (1975). Investigation of impact ionization and avalanche breakdown in high-voltage p-n junctions. *Extended abstract of candidate's thesis.* Moscow, All-Russian Electrotechnical Institute named after V.I. Lenin.

13 Ya, L. (1979). Distribution of impurities in large area gallium arsenide structures grown by liquid epitaxy. *Materials of the report. At the All-Union Coordinators. Meeting Sections "Semiconductor. Heterostructures"*. Tallinn, 66-73.

14 Vainshtein, S.N., Yuferev V.S., Kostamovaara J.T., Kulagina, M.M., & Moilanen, H.T. (2010). Significant Effect of Emitter Area on the Efficiency, Stability and Reliability of Picosecond Switching in a GaAs Bipolar Transistor Structure. *IEEE Transactions on Electron Devices, Vol 57*(4).

15 Sarkat, T., & Mazumder, S.K. (2007). Epitaxial Desingn of Direct Optically Controlled GaAs/AlGaAs –based Heterostructure Lateral Superjunction Power Device for Fast Repetitive Switching. *IEEE Transactions on Electron Devise, Vol. 54*(3).

16 Mamatkarimov, O.O., Khamidov, R., & Abdukarimov, A.A. (2019). The relative current change, concentration, and carrier mobility in silicon samples doped nickel and at pulse hydrostatic pressure. *Materials Today: Proceedings 17,* 442–445.

17 Voitovich, V., Gordeev, A., & Dumanevich, A. (2009). GaAs - diodes for PFC, SMPS, UPS, IPM Solar Inverters and replacement of synchronous rectifiers. *2 Power Electronics*, 6.

18 Karimov, M., Makhkamov, Sh., Makhmudov, Sh.A., Muminov, R.A., Rakhmatov, A.Z., Sulaymanov, A.A., & Tursunov, N.A. (2010). Peculiarities of influence of radiation defects on photoconductivity of silicon irradiated by fast neutrons. *Applied Solar Energy, Allerton Press, Inc., Vol. 46*(4), 298-300.

19 Zadiranov, Yu.M., Korolkov, V.I., Ponomarev, S.I., Rozhkov, A.V., & Tsvilev, G.I. (1987). High-voltage impulse thyristors based on lightly alloyed gallium arsenide. *JTF. Vol. 57*(4), 771-777.

А.М. Султанов, А.А. Абдукаримов, М.З. Куфиан

GaAs негізіндегі жоғары вольтты $p^0 – n^0$ өтулерін құрудың технологиясын дамыту

Негізгі емес заряд тасымалдаушылардың фотонды-инъекциялық механизмі бар аса тез әсер ететін жоғары вольтты импульсті үш электродты коммутаторды жасау үшін электрфизикалық параметрлердің жоғары мәндері және берілген базалық қабаттардың қалыңдығы бар GaAs әлсіз легирленген қабаттары негізінде p0-n0 өтулерін алудың оңтайлы шешімі табылды. Галлий арсениді және оның қатты ерітінділері негізінде жоғары вольтты, қуатты субнаносекундтық фотонды инъекциялық қосқыштарды қалыптастыру технологиясы әзірленді. Токтың өсу уақытының, кернеуді қайта қосу және қайта қосудың тұрақтылығы оларды пайдалануда кең ток және жиілік режиміндегі жоғары вольтты фотонды-инжекциялық коммутаторлардың басқару импульсіне тәуелділігі, оның әртүрлі сыртқы әсерлерге сезімталдығы, сондай-ақ p^0-қабатының қалыңдығына, беріліс коэффициентіне, жоғары вольтты p^0-n^0 өтулерінде U сынамасының тесілуі кернеуге байланысты екендігі зерттелді. Жүргізілген зерттеулер мен алынған нәтижелер жоғары қуатты лазерлік және жарықдиодты құрылымдарды айдау үшін пикосекундтық оптоэлектроникада әзірленген жоғары вольтты импульстік жартылай өткізгіш құрылғыларды пайдалану перспективаларын көрсетеді.

Кілт сөздер: сұйық фазалық эпитаксис (LPE), гетероқұрылымдар, жоғары вольтты p^0-n^0 өтулері, Холл эффектісі, фондық легирлеу, ерітінді-балқыма.

А.М. Султанов, А.А. Абдукаримов, М.З. Куфиан

Разработка технологии создания высоковольтных p^0–n^0-переходов на основе GaAs

Найдено оптимальное решение проблемы получения p^0–n^0-переходов на основе слаболегированных слоев GaAs с высокими значениями электрофизических параметров и заданными толщинами базовых слоев для создания сверхбыстродействующих высоковольтных импульсных трехэлектродных коммутаторов с фотонно-инжекционным механизмом неосновных носителей заряда. Разработана технология формирования высоковольтных мощных субнаносекундных фотонно-инжекционных коммутаторов на основе арсенида галлия и его твердых растворов. Изучена зависимость времени нарастания тока, напряжения переключения и стабильности переключения относительно импульса управления высоковольтных фотонно-инжекционных коммутаторов в широком токовом и частотном режиме их эксплуатации, ее чувствительность к различным внешним воздействиям, а также зависимости от толщины p^0-слоя, от коэффициента передачи, от напряжения пробоя U проб высоковольтного p^0–n^0-перехода. Проведенные исследования и полученные результаты указывают на перспективность применения разработанных высоковольтных импульсных полупроводниковых приборов в пикосекундной оптоэлектронике для накачки мощных лазерных и светодиодных структур.

Ключевые слова: жидкофазная эпитаксия, гетероструктуры, высоковольтный p^0–n^0-переход, эффект Холла, фоновое легирование, раствор–расплав.

DOI 10.31489/2023PH4/57-64

UDC 536.4:519.688

P. Saidakhmetov[1*], I. Piyanzina[2], G. Baiman[1], O. Nedopekin[2], D. Tayurskii[2]

[1]*M.O. Auezov South Kazakhstan University, Shymkent, Kazakhstan;*
[2]*Kazan Federal University, Kazan (Volga Region), Russia*
[*]*Corresponding authors e-mail*: *timpf_ukgu@mail.ru*

The glass transition temperature investigation of polymers by molecular dynamic simulations

In this paper, the process of glass transition is studied, the theory of which is not fully developed. Computer modeling can be used to understand the theory of this phenomenon. The glass transition temperature is influenced by a large number of polymer parameters: cooling rate, pressure, presence of diluent, structural features, etc. We are considering a number of different polymers to test the ability of the pcff+ force field to determine the glass transition temperature. The effect of tactility, composition, pressure and the presence of a diluent on the glass transition temperature of polymers will be shown using molecular dynamics (MD) and pcff+ force-field modeling. The effect of tact was studied using the use of atactic, isotactic and syndiotactic poly(methyl methacrylate) and atactic, isotactic and syndiotactic polypropylene. The LAMMPS code integrated into the MedeA computing environment was used to simulate the molecular dynamics of polymers. The calculation of the glass transition temperature at different cooling rates is closely related to the balanced initial systems. Due to the inability of current atomistic simulations to achieve the required cooling rates, as in experiments, the gap was not sharp and quite obvious. The data obtained show that the pcf+ force field describes tactics quite effectively and gives differences in the glass transition temperature for different types of tact. For polymers diluted with CO_2, the glass transition temperature decreases almost linearly, which is in good agreement with the experiment. As expected, the pressure increases the glass transition temperature. However, at high pressure, the slope fracture disappears, and the determination of Tg becomes extremely difficult. The simulated annealing process will be applied to a set of polymers to obtain graphs of the specific volume versus temperature and determine the glass transition temperature.

Keywords: cooling rate, pressure, glass transition temperature, pcff+, molecular dynamics simulations.

Introduction

The glass transition temperature (T_g) is one of the most important parameters in amorphous polymer manufacturing [1]. Moreover, this parameter is essential in the selection of materials for various applications. In general, polymers with T_g below room temperature define elastomers, and polymers with T_g above room temperature define rigid, structural polymers [2].

Unfortunately, the glass transition phenomenon is not completely understood [3]. There is no theory which can fully explain observed behavior of polymers [4]. The computer simulations could help to show the link between the bulk properties and intermolecular forces [5] and bring us closer to understanding this phenomenon.

It is well known that T_g is affected by a wide range of polymer parameters. External variables include cooling rate, pressure, presence of diluent; structural features include molecular weight, composition, crystallinity, copolymerization, branching, cross-linking, stiffness, geometric factors etc.

In the present work we investigate a set of different polymers in order to test the ability of pcff+ force-field for the glass transition temperature determination. The tacticity effect was investigated using atactic, isotactic and syndiotactic poly(methyl methacrylate) (a-PMMA, i-PMMA and s-PMMA) and atactic, isotactic and syndiotactic polypropylene (a-PP, i-PP and s-PP). The pressure was applied for two polymer systems: polyvinyl chloride (PVC) and polystyrene (PS). In order to get the composition effect on T_g polyamide 6 and polyamide 66 (PA6 and PA66), poly(methyl methacrylate), poly(methyl acrylate) and poly(ethyl methacrylate) (PMMA, PMA and PEMA), poly(p-phenylene ox-ide) and polyethylene terephthalate (PPO and PET) have been investigated. The last one is the CO_2 effect on PPO's glass transition temperature.

Methods and materials

The LAMMPS code [6] integrated into MedeA computational environment [7] was used to simulate molecular dynamics of polymers. The major advantage of this software is the time spent for the calculation. At first a single repeat unit was built and relaxed. In order to construct polymer chain and amorphous cell the

Polymer Builder and Amorphous Materials Builder of MedeA environment respectively were used. Each polymer chain in this study was possessed by 100 repeat units. The head-tail orientation was used. The amorphous cell was represented by one polymer chain at 298.2 K. In Figure 1 a single repeat unit, polymer chain and amorphous cell of PPO as example are presented. For all simulations the pcff+ force-field was used, which is based on the pcff+ force-field [8]. The pcff+ force-field was constructed to work with wide range of polymers [5]. Ten randomly built amorphous cells were used to represent the phase space for each polymer.

The MD simulations were carried out firstly in the NVT ensemble at initial T=298 K and final T=300 K with a t=1 fs integration time step and in the Berendsen [9] thermostat. A relaxation annealing was carried out in the following way: the system was firstly heated to high temperature and then slowly cooled down. This process has been carried out using NPT ensemble with t=1 fs integration time step. Also, the Berendsen thermostat and barostat were considered to keep the system at prescribed temperatures and pressures. The non-bonded interactions have been computed using Ewald summation method [10] and nonbond cut-off equal to 9.5 Angstrom. The simulated dilatometry [11] was used with the heating rate equal to 3 10^{13} K/min, i.e., the system was firstly heated up by 50 K step with 100 ps duration time; and with the cooling rate equal to 7.5 10^{12} K/min, i.e., the system was cooled down then by 25 K step with 200 ps duration time. For each temperature the specific volume i.e., the inverse density, was reported. Then, averaging over all configurations was performed. The linear averaging was applied for beginning and the tail of obtained sequence (without the central part) and the break of the slope yielded the T_g. The linear fitting was performed using analysis of coefficient of determination (lines with minimum coefficient were taken). To compare the results for various polymers we used the same procedure for T_g extraction for all polymers.

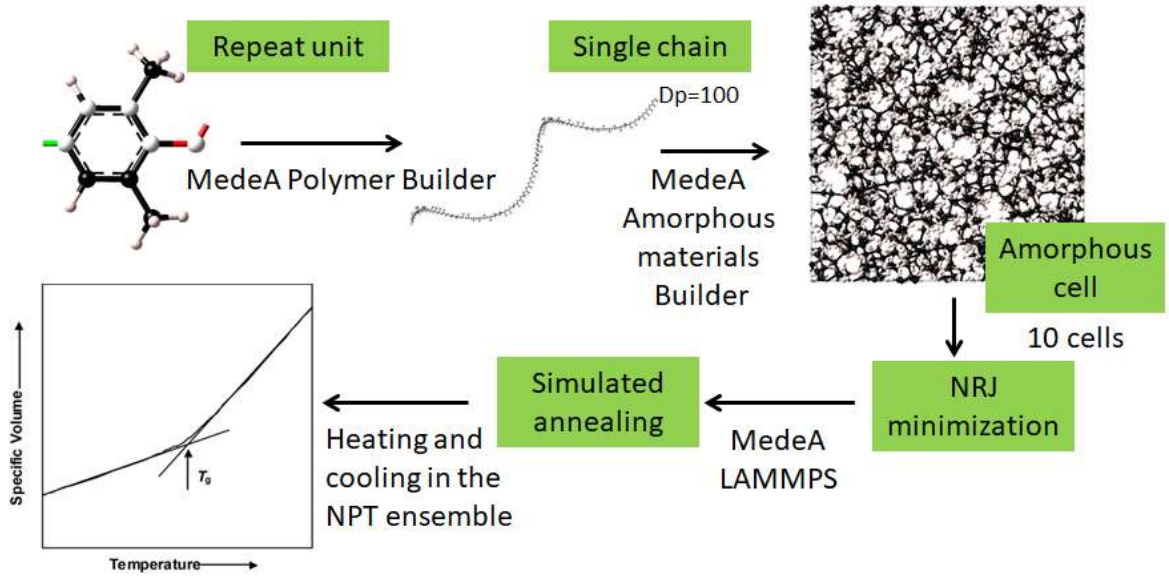

Figure 1. Stages of amorphous cell construction and T_g determination used in the present study.

Results and discussion

Tacticity effect

In the present work, three types of PMMA tacticities were considered: isotactic (i-PMMA), atactic (a-PMMA) and syndiotactic (s-PMMA). Results are presented in Figure 2. The specific volume versus temperature of PP in atactic, isotactic and syndiotacticities have been calculated as well. Results are presented in the Figure 2. The glass transition temperatures of all tacticities were obtained close to each other and a little bit higher than experimental temperatures extracted numbers are listed in Table 1. Pcff+ force-field describes tacticity quite well. However, T_g values determined for PMMA and PP are higher than the experimental values by 20-35% and 1-3%, respectively. That can be explained by the fact that LAMMPS program uses classical principles to simulate molecular dynamics. For some polymers this is important (as for PMMA), but for some it is not (as for PP).

Table 1

Experimental [12-14] and calculated using pcff+ force-field glass transition temperatures in Kelvin for atactic (a-PP), isotactic (i-PP) and syndiotactic (s-PP) polypropylene as well as isotactic, atactic and syndiotactic poly(methyl methacrylate) (i-PMMA, a-PMMA, s-PMMA).

	Calc, K	Exp, K
a-PP	275	260-266
i-PP	280	265-272
s-PP	275	266-268
i-PMMA	527	388
a-PMMA	470	378
s-PMMA	503	323

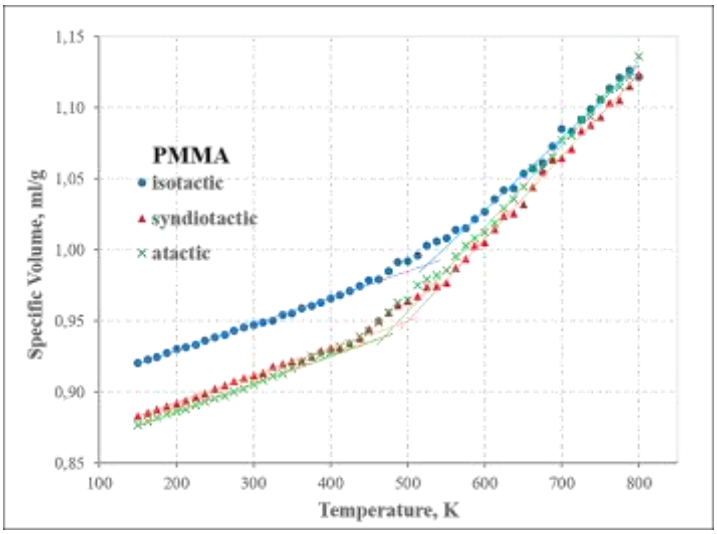

Figure 2. Calculated specific volume vs. temperature of PMMA in different tacticities

Composition effect

The thermal volumetric expansion coefficient indicates how the polymers volume will evolve when facing a change of temperature. For this study, coefficients were calculated for both glassy and liquid states of considered polymers using obtained specific volume versus temperature graphs and following formula:

$$\alpha = \frac{1}{V_{sp}}\left(\frac{\partial V_{sp}}{\partial T}\right)_{\rho} = \frac{1}{\rho},$$

where V_{sp} is a specific volume at given temperature, is a density of a polymer at a given temperature.

Simulated thermal expansion coefficients are reported versus experimental expansion coefficients for all considered polymers in Figure 3. Generally, the experimental coefficient of thermal expansion should be higher. One may notice that for PP there is better agreement than for the rest of the polymers. This can be explained by the fact that the PP has a simpler structure and, therefore, the calculations for it are more accurate.

Simulated T_g are reported versus experimental values for all considered polymers in Figure 4. It should be noted that PVC and PP have the best accordance with experimental values; PS, PPO and PMA have moderate agreement, and PET, PA6 and PA66 have the worse agreement. PVC and PP have the simplest and similar structure. PS and PPO have benzene ring and structure that is more complex. PET and both polyamides,

have the most complex structure and long repeat units. Talking about polyamides in should be mentioned that PEMA has the biggest T_g among considered polyacrylates due to the longest sidechain. On the contrary, PMA has the smallest T_g. The PMMA polymer has the middle T_g. The big discrepancy from experimental value for the PEMA could be due to complex structure in comparison with PMMA and PMA.

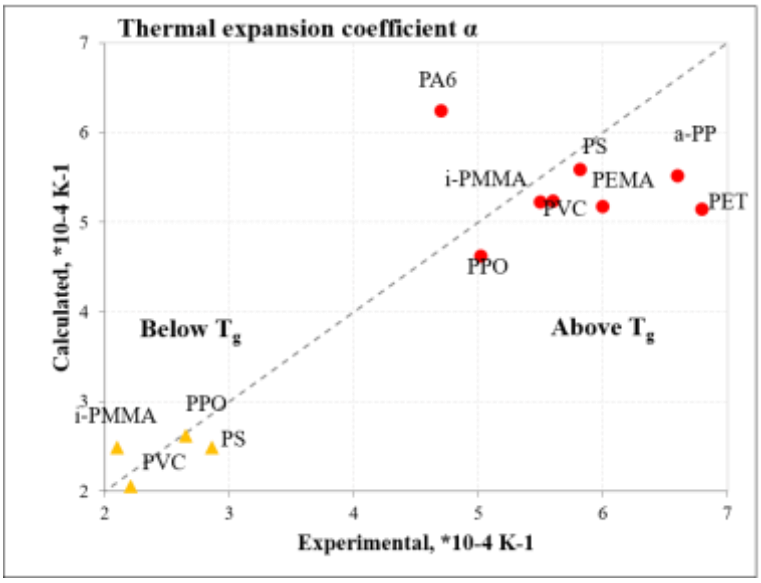

Figure 3. The simulated thermal expansion coefficients for liquid state at 300K versus experimental data from Ref. [15]. The experimental equivalence line is also displayed.

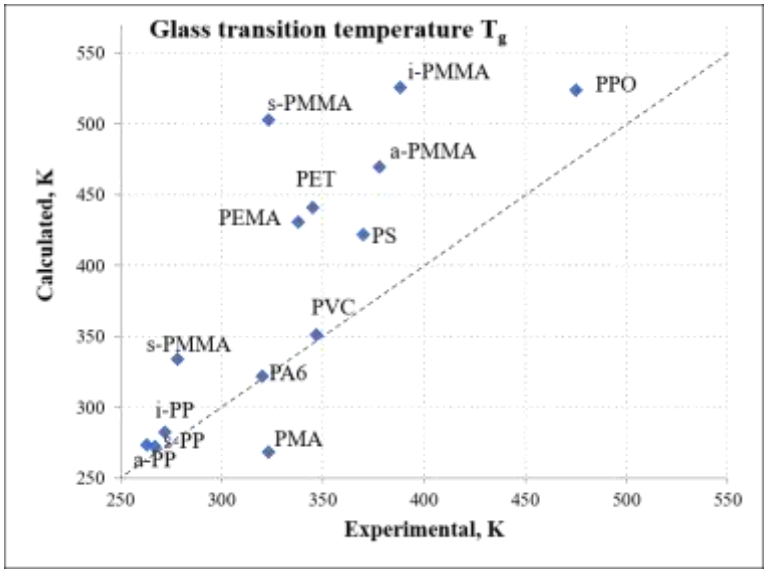

Figure 4. The simulated glass transition temperature versus experimental data from Ref. [15]. The experimental equivalence (dashed) line is also displayed.

Pressure effect

To investigate the pressure effect on T_g the calculations for PVC, PPO and PS were performed under 0, 60 and 100 MPa. Specific volume versus temperature graph for PVS is presented in Figure 5. Experimental values have been taken from [16, 17].

When the pressure goes up it becomes very difficult to determine T_g. With the high pressure, the curve corresponding to glassy state and experimental curve in the glassy state become closer. Extracted T_g at each pressure are presented in the Table 2 and linear relationship between experimental and simulated T_g can be

identified. It could be assumed, that adding more configurations could improve the representation of curves and make determination of T_g more accurate.

Calculations under pressure were done for PS and PVC as well. Extracted values are collected in Table 2. As shown in the table the difference of T_g between 0-60 MPa and 60-100 MPa for both polymers are good predicted despite the low molecular dynamic duration time during calculations.

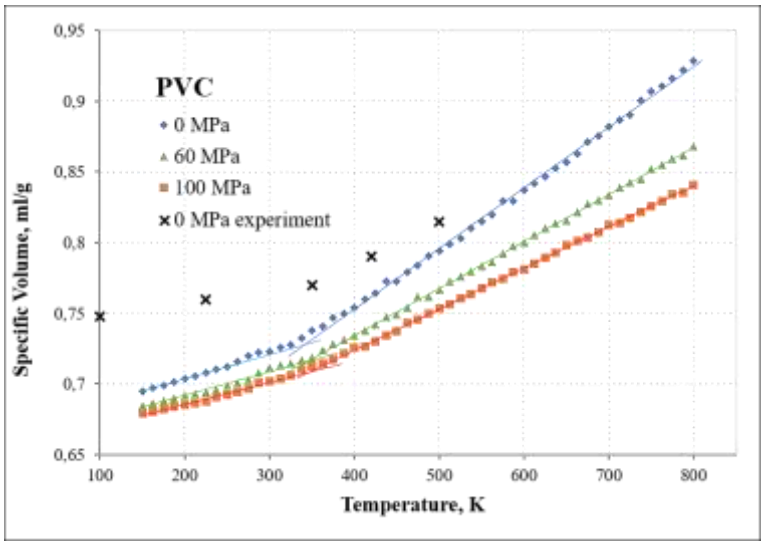

Figure 5. Calculated specific volume vs. temperature for PVC at the indicated pressures. Solid lines are linear fitting. Experimental data from [17].

Table 2

Experimental [16, 17] and calculated using pcff+ forcefield glass transition temperatures in Kelvin for atactic PVC, PPO and PS for indiated pressures.

		0 MPa	60 MPa	100 MPa
PVC	Calc.	345	360	370
	Exp.	347	368	377
PPO	Calc.	525	550	570
	Exp.	475	505	525
PS	Calc.	370	395	415
	Exp.	420	440	460

Presence of diluent

For most polymers, the carbon dioxide (CO_2) can significantly change the mobility of the polymer melt and cause a reduction of T_g by tens of degrees [18, 19]. In the present study CO_2 molecules were added into the Poly (2, 6-dimethyl-1, 4-phenylene oxide) (PPO) in different concentration.

Considering the fact that molecular weight of PPO with degree of polymerization of 100 equal to 1916.7 g/mole, the concentration of CO_2 was evaluated using formula:

$$\frac{N*M(CO_2)}{M(PPO)},$$

where N is number of CO_2 molecules in the amorphous cell of polymer, M(CO_2) is molecular weight of CO_2, M(PPO) is molecular weight of PPO.

In Figure 6 the glass transition temperature has been plotted versus concentration of carbon dioxide. We can conclude that the glass transition temperature almost linearly decreases with the amount of carbon dioxide. From the qualitative point of view obtained results agree well with experimental data taken from

Ref. [20], from the qualitative point of view there is upward shift of calculated curve for around 80 K, which could be understood in terms of fast cooling during MD simulations.

		0 MPa	60 MPa	100 MPa
PVC	Calc.	345	360	370
	Exp.	347	368	377
PPO	Calc.	525	550	570
	Exp.	475	505	525
PS	Calc.	370	395	415
	Exp.	420	440	460

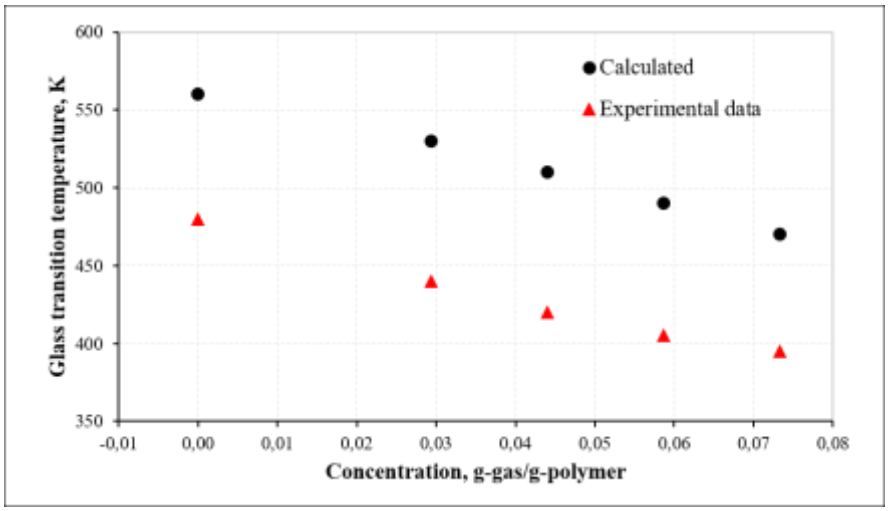

Figure 6. The calculated and experimental [20] glass transition temperature of PPO with CO_2 at various concentration

Conclusion

The computation of T_g at different cooling rates must be intimately associated with equilibrated initial systems. The break was not sharp and sufficiently obvious because of inability of present atomistic simulations achieve necessary cooling rates as in the experiments.

According to the data obtained, we can conclude that the pcff+ force-field describes tacticity quite effectively. We see differences in the glass transition temperature for different types of tacticities.

The atomic simulation was also successfully applied for polymers diluted by CO_2. In this case, adding CO_2 molecules into polymer system decreases the glass transition temperature almost linearly and this behavior agrees well with experiment. As was expected we have shown that the pressure increases T_g. However, when the pressure is high the break of the slope vanishes and determination of T_g becomes extremely difficult.

References

1 Erber, M., Tress, M., & Eichhorn, K. J. (2014). Glass transition of polymers with different architectures in the confinement of nanoscopic films. *Ellipsometry of Functional Organic Surfaces and Films*, 63-78.

2 Han, J., Gee, R. H., & Boyd, R. H. (1994). Glass transition temperatures of polymers from molecular dynamics simulations. *Macromolecules, 27*(26), 7781-7784. https://doi.org/10.1021/ma00104a036

3 McKenna, G. B., & Simon, S. L. (2002). Handbook of thermal analysis and calorimetry, *3*, 49-109.

4 Ebewele, R. O. (2000). *Polymer science and technology*. CRC press.

5 Soldera, A. (1998). Comparison between the glass transition temperatures of the two PMMA tacticities: A molecular dynamics simulation point of view. Wiley Online Library, 133, 21-32.

6 Plimpton, S, Crozier, P, & Thompson, A. (2007). LAMMPS-large-scale atomic/molecular massively parallel simulator. Sandia National Laboratories, 18, 43.

7 Materials Design Inc. Retrieved from http://www.materialsdesign. com/

8 Sun, H., Mumby, S.J., Maple, J.R., & Hagler, A.T. (1995). Ab initio calculations on small molecule analogs of polycarbonates. *The Journal of Physical Chemistry, 99*(16), 5873-5882. https://doi.org/10.1021/j100016a022

9 Berendsen, H.J., Postma, J.V., Van Gunsteren, W.F., DiNola, A.R.H.J., & Haak, J.R. (1984). Molecular dynamics with coupling to an external bath. *The Journal of chemical physics, 81*(8), 3684-3690. https://doi.org/10.1063/1.448118

10 Ewald, P. (1921). Die Berechnung optischer und elektrostatischer Gitterpotentiale. *Ann. Phys.* 361, 253. https://doi.org/10.1002/andp.19213690304

11 Rigby, D., & Roe, R.J. (1987). Molecular dynamics simulation of polymer liquid and glass. I. Glass transition. *The Journal of chemical physics, 87*(12), 7285-7292. https://doi.org/10.1063/1.453321

12 Brandrup, J., Immergut, E.H., Grulke, E.A., Abe, A., & Bloch, D.R. (1989). Polymer handbook, "Wiley: New York". NY, USA.

13 Supaphol, P., & Spruiell, J.E. (2000). Thermal properties and isothermal crystallization of syndiotactic polypropylenes: Differential scanning calorimetry and overall crystallization kinetics. *Journal of applied polymer science, 75*(1), 44-59. https://doi.org/10.1002/(SICI)1097-4628(20000103)75:1<44::AID-APP6>3.0.CO;2-1

14 Ashby, M.F., & Cebon, D. (2005). Materials selection in mechanical design. *MRS Bull, 30*(12), 995. https://doi.org/10.1557/mrs2005.264

15 Mark, J.E. (Ed.). (2007). *Physical properties of polymers handbook* (Vol. 1076, p. 825). New York: springer.

16 Schneider, H., Rudolf, B., Karlou, K., & Cantow, H.J. (1994). Pressure influence on the glass transition of polymers and polymer blends. *Polymer Bulletin, 32*(5-6), 645. https://doi.org/10.1007/BF00973914

17 Abu-Sharkh, B.F. (2001). Glass transition temperature of poly(vinylchloride) from molecular dynamics simulation: explicit atom model versus rigid CH_2 and CHCl groups model. *Computational and Theoretical Polymer Science, 11*(1), 29. https://doi.org/10.1016/S1089-3156(99)00070-7

18 Handa, Y.P., Capowski, S., & O'Neill, M. (1993). Compressed-gas-induced plasticization of polymers. *Thermochimica acta, 226*, 177-185. https://doi.org/10.1016/0040-6031(93)80219-Z

19 O'Neill, M., & Handa, Y. (1994). On the plasticization of poly(2,6-dimethyl phenylene oxide) by CO_2. *J. Polym. Sci. B Polym. Phys., 32*, 2549-2553. https://doi.org/10.1002/polb.1994.090321512.

20 Sato, Y., Takikawa, T., Yamane, M., Takishima, S., & Masuoka, H. (2002). Solubility of carbon dioxide in PPO and PPO/PS blends. *Fluid Phase Equilibria, 194*, 847-858. https://doi.org/10.1016/S0378-3812(01)00687-2

П. Саидахметов, И. Пиянзина, Г. Байман, О. Недопекин, Д. Таюрский

Молекулалық-динамикалық модельдеу әдісімен полимерлердің шынылану температурасын зерттеу

Мақалада шынылау процесі зерттелген, себебі оның теориясы толық дамымаған. Берілген құбылыстың теориясын түсіну үшін компьютерлік модельдеуді қолдануға болады. Шыны температурасына полимерлердің көптеген параметрлері әсер етеді: салқындату жылдамдығы, қысым, еріткіштің болуы, құрылымдық ерекшеліктері және т.б. Біз pcff+ қуат өрісінің шыны температурасын анықтау қабілетін тексеру үшін бірқатар әртүрлі полимерлерді қарастырамыз. Полимерлердің шынылану температурасына тактильділік, құрамы, қысымы және еріткіштің болуының әсері молекулалық динамика (MD) және pcff+ force-field өрісінің модельдеулері арқылы көрсетілген. Тактикалық әсері атактикалық, изотактикалық және синдиотактикалық полиді(метилметакрилат), сонымен қатар атактикалық, изотактикалық және синдиотактикалық полипропиленді қолдану арқылы зерттелді. Полимерлердің молекулалық динамикасын модельдеу үшін MedeA есептеу ортасына біріктірілген LAMMPS коды қолданылды. Әртүрлі салқындату жылдамдығындағы шынының температурасын есептеу теңдестірілген бастапқы жүйелермен тығыз байланысты. Ағымдағы атомдық модельдеулердің эксперименттердегідей қажетті салқындату жылдамдығына қол жеткізуге қабілетсіздігіне байланысты үзіліс жеткілікті түрде өткір немесе айқын болмады. Алынған деректер pcff+ күш өрісі тактиканы жеткілікті тиімді сипаттайтынын және тактиканың әртүрлі түрлері үшін шыны ауысу температурасының айырмашылығын беретінін көрсетеді. CO2 сұйылтылған полимерлер үшін шыны ауысу температурасы дерлік сызықты түрде төмендейді, бұл тәжірибемен жақсы сәйкес келеді. Күтілгендей, қысым шыны ауысу температурасын арттырады. Бірақ жоғары қысымда көлбеу қисаюы жойылып, Tg анықтау өте қиынға соғады. Температураға қарсы нақты көлемнің сызбаларын алу және шыны ауысу температурасын анықтау үшін полимерлер жиынтығына имитациялық жасыту процесі қолданылады.

Кілт сөздер: салқындату жылдамдығы, қысым, шыны температурасы, pcff+, молекулалық динамикалық модельдеу.

П. Саидахметов, И. Пиянзина, Г. Байман, О. Недопекин, Д. Таюрский

Исследование температуры стеклования полимеров методом молекулярно-динамического моделирования

В статье изучен процесс стеклования, теория которой не разработана полностью. Компьютерное моделирование можно использовать для понимания теории данного явления. На температуру стеклования оказывает влияние большое количество параметров полимеров: скорость охлаждения, давление, присутствие разбавителя, структурные особенности и т.д. Мы рассматриваем ряд различных полимеров для проверки способности силового поля *pcff+* по определению температуры стеклования. Влияние тактильности, состава, давления и присутствия разбавителя на температуру стеклования полимеров будет показано с помощью моделирования молекулярной динамики (MD) и *pcff+ force-field*. Эффект тактичности был изучен с помощью применения атактического, изотактического и синдиотактического поли(метилметакрилата) и атактического, изотактического и синдиотактического полипропилена. Для моделирования молекулярной динамики полимеров использовался код *LAMMPS*, интегрированный в вычислительную среду *MedeA*. Расчет температуры стеклования при различных скоростях охлаждения тесно связан с уравновешенными исходными системами. Из-за неспособности нынешних атомистических симуляций достичь необходимых скоростей охлаждения, как в экспериментах, разрыв не был резким и достаточно очевидным. Полученные данные показывают, что силовое поле *pcff+* достаточно эффективно описывает тактику и дает различия в температуре стеклования для разных типов тактичности. Для полимеров, разбавленных CO_2, температура стеклования снижается почти линейно, что хорошо согласуется с экспериментом. Как и ожидалось, давление увеличивает температуру стеклования. Однако при высоком давлении излом наклона исчезает, и определение Tg становится крайне затруднительным. Имитированный процесс отжига будет применен к набору полимеров, чтобы получить графики зависимости удельного объема от температуры и определить температуру стеклования.

Ключевые слова: скорость охлаждения, давление, температура стеклования, *pcff+*, молекулярно-динамическое моделирование.

DOI 10.31489/2023PH4/65-75

UDC 539.3

V.N. Ukrainets, S.R. Girnis, K.T. Makashev, V.T. Stanevich

Toraighyrov University, Pavlodar, Kazakhstan
(E–mail: vitnikukr@mail.ru, girnis@mail.ru, makashevkuanysh10@gmail.com, svt_18@mail.ru
**Corresponding authors e-mail: vitnikukr@mail.ru*

Dynamic response of unsupported and supported cavities in an elastic half-space under moving normal and torsional loads

This study explores the impact of uniformly moving normal and torsional loads along an infinitely long circular cylindrical cavity, situated within a half-space (body), on the behavior of the elastic half-space. The cavity is either unreinforced or reinforced by a thin-walled elastic shell. To describe the motion of the body and the shell, dynamic equations of elasticity theory in the Lamé potentials and equations of the classical shell theory are used, respectively. The equations are represented in coordinate systems moving together with the loads (cylindrical or Cartesian). The method of integral Fourier transform is used to determine the stress-strain state (SSS) of the half-space. The solution to this problem considers waves reflected from the boundary of the half-space, which occur during the movement of loads, instead of assuming the body is an elastic space like similar works. The results of numerical experiments are presented, illustrating the influence of the shell on the deformed state of the half-space boundary under the action of axisymmetric normal and shear loads, which are uniformly applied within a certain range and move at a constant speed.

Keywords: elastic half-space, body, cavity, cylindrical shell, moving load, velocity, displacement, stress.

Introduction

Lately, there has been a noticeable increase in studying the dynamic behavior of various engineering and structural systems due to the diverse types of moving loads they encounter. Such problems arise in the calculation of aerodromes under the influence of moving aircraft, tunnels, and underground pipelines under the influence of transport loads (loads that occur during the movement of intratunnel transport and the transportation of solid materials, liquids, and gases through pipelines) and so on. The rapid progress in modern technology, computational mathematics, and computer technologies has played a crucial role in stimulating this growing interest.

In the context of the tunnel and underground main pipeline dynamics subjected to transportation loads, the research typically focuses on model problems addressing the effect of a load on a cylindrical shell (the surface of the cavity if the tunnel is unsupported) situated within an elastic body. The load uniformly moves along the inner surface of the shell along its generatrix. In the case of deep placement of these structures, the body represents an elastic space, while in the case of shallow placement, it is an elastic half-space. Model problems of the tunnel and deep-buried transportation pipeline dynamics under the influence of transportation loads have been examined in numerous scientific studies. The number of publications dedicated to this issue is relatively small in the case of shallow placement of these structures due to the more complex nature of the problem formulation. Recent years have seen a notable increase in published works that deserve recognition [1–6]. In these studies, numerical investigations of the SSS of the body were conducted for the case when a normal moving load of various types acts on the cylindrical shell or the cavity surface. In articles [7, 8] similar investigations were conducted for the case of a normal axisymmetric load [7] and an axisymmetric torsional load [8] acting on an extremely long thin-walled circular cylindrical shell positioned in an elastic space. To describe the motion of both the body and the shell, the dynamic equations of elasticity theory and the equations of the classical theory of shells were used, represented in the moving cylindrical coordinate system. In [7], when the speed of the load's movement was subsonic, the Fourier transformation was applied to the moving axial coordinate for solving the problem. Dynamic equations of the theory of elasticity and classical shell theory equations were used to describe the motion of the body and shell, respectively. These equations were presented in a moving cylindrical coordinate system. In article [7], Fourier transformation was used to solve the problem, while in article [8], Fourier or Laplace transformation was applied with respect to the moving coordinate.

The present article provides a solution to the problem of the combined action of moving normal and torsional loads on an infinitely long thin-walled circular cylindrical shell or cavity surface in an elastic inertial half-space. Such action occurs during the rotational movement of cleaning devices in an underground pipeline [9], and it can also arise due to the inequality of dynamic loads transmitted to each of the rails laid in a cylindrical tunnel [10], whether supported by a shell or unsupported. In contrast to [7, 8] and similar works, the moving loads in this article can have an arbitrary form. Additionally, when solving the problem, the influence of waves reflected from the boundary of the half-space, which arise during the movement of loads, is taken into account.

Methods

The study is based on assumptions and equations of elasticity theory. To solve the problem, the method of integral Fourier transform is used. This allows us to consider moving loads distributed along the shell's axis according to an arbitrary law and obtain the final expression of the solution without the need for summation.

Problem formulation and solution

Let's consider a homogeneous and isotropic body in Cartesian x, y, z and cylindrical r, θ, z coordinate systems, which have a common origin occupying a fixed position in space. The body is a linear elastic half-space ($x = h$), with its boundary free from loads and parallel to the z-axis. The body contains an elongated circular cylindrical cavity with a radius of R, the axis of which coincides with the x-axis (Fig. 1). The surface of the cavity can be rigidly connected to a thin shell with a thickness of h_0. Since the shell has a small thickness, we will assume that it contacts the body along its middle surface (Fig. 2). We will use the following notation for the physicomechanical properties of the body and shell materials. Poisson's ratio: ν (for the body), ν_0 (for the shell); shear modulus: μ (for the body), μ_0 (for the shell); density: ρ (for the body), ρ_0 (for the shell).

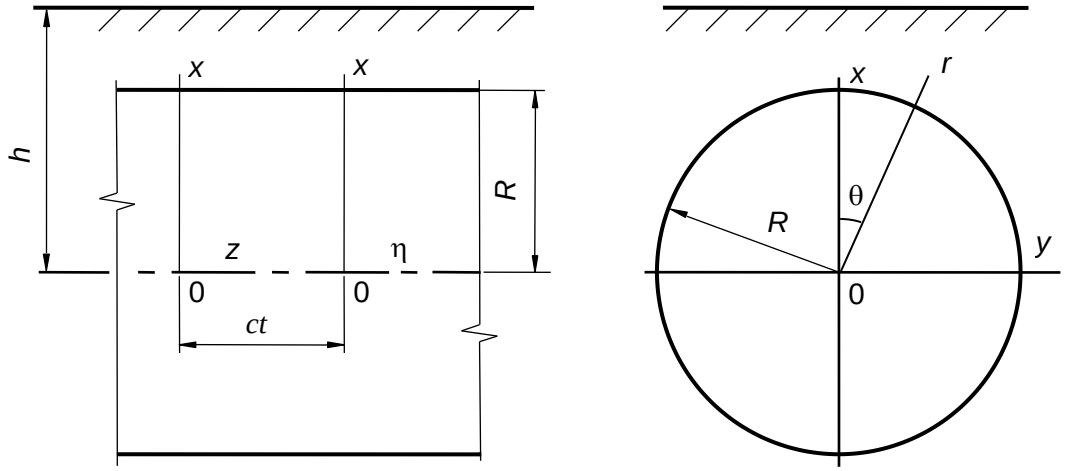

Figure 1. Half-space containing a circular cavity

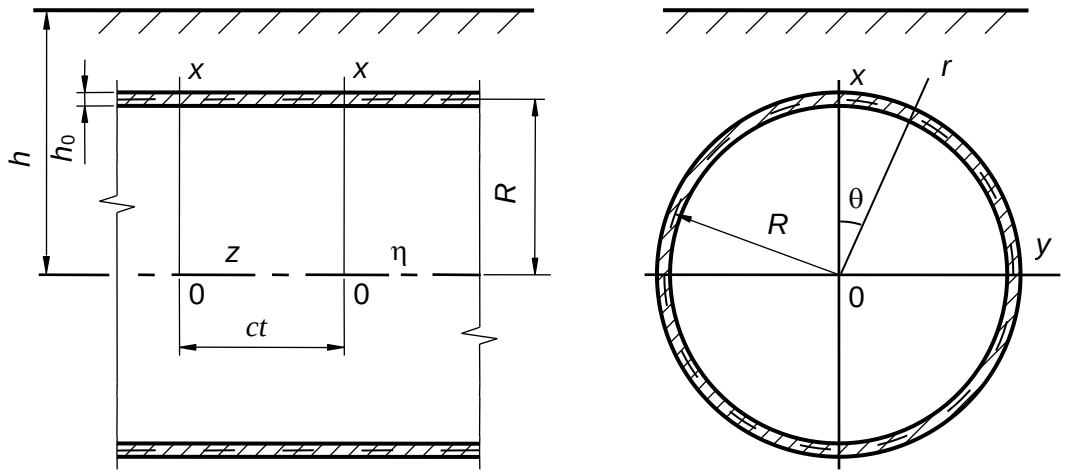

Figure 2. Half-space containing a circular shell

Figures illustrate normal and tangential (torsional) loads moving along the *z*-axis at a constant speed *c*, either on the surface of the cavity (Fig. 1) or the shell (Fig. 2), sharing common points of application and identical characteristics. The ensuing analysis aims to ascertain the SSS of the body.

To solve the problem, we will use coordinate systems moving together with the load: Cartesian $(x, y, \eta = z - ct)$ and cylindrical $(r, \theta, \eta = z - ct)$. In these coordinate systems, the motion of the body and the shell will be described by equations (1) and (2), respectively. [1, 2]:

$$\left(M_p^{-2} - M_s^{-2}\right)\text{grad div}\,\mathbf{u} + M_s^{-2}\nabla^2\mathbf{u} = \partial^2\mathbf{u}/\partial\eta^2\,, \tag{1}$$

where $M_p = c/c_p$, $M_s = c/c_s$ – Mach numbers; $c_s = \sqrt{\mu/\rho}$, $c_p = \sqrt{(\lambda+2\mu)/\rho}$ – the speeds of propagation of compression-expansion and shear waves in the body, $\lambda = 2\mu\nu/(1-2\nu)$; ∇^2 – Laplace operator, **u** – the displacement vector of the elastic body.

$$\begin{aligned}
&\left[1 - \frac{(1-\nu_0)\rho_0 c^2}{2\mu_0}\right]\frac{\partial^2 u_{0\eta}}{\partial\eta^2} + \frac{1-\nu_0}{2R^2}\frac{\partial^2 u_{0\eta}}{\partial\theta^2} + \frac{1+\nu_0}{2R}\frac{\partial^2 u_{0\theta}}{\partial\eta\partial\theta} + \frac{\nu_0}{R}\frac{\partial u_{0r}}{\partial\eta} = -\frac{1-\nu_0}{2\mu_0 h_0}q_\eta,\\
&\frac{1+\nu_0}{2R}\frac{\partial^2 u_{0\eta}}{\partial\eta\partial\theta} + \frac{(1-\nu_0)}{2}\left(1 - \frac{\rho_0 c^2}{\mu_0}\right)\frac{\partial^2 u_{0\theta}}{\partial\eta^2} + \frac{1}{R^2}\frac{\partial^2 u_{0\theta}}{\partial\theta^2} + \frac{1}{R^2}\frac{\partial u_{0r}}{\partial\theta} = \frac{1-\nu_0}{2\mu_0 h_0}(P_\theta - q_\theta),\\
&\frac{\nu_0}{R}\frac{\partial u_{0\eta}}{\partial\eta} + \frac{1}{R^2}\frac{\partial u_{0\theta}}{\partial\theta} + \frac{h_0^2}{12}\nabla^2\nabla^2 u_{0r} + \frac{(1-\nu_0)\rho_0 c^2}{2\mu_0}\frac{\partial^2 u_{0r}}{\partial\eta^2} + \frac{u_{0r}}{R^2} = -\frac{1-\nu_0}{2\mu_0 h_0}(P_r - q_r),
\end{aligned} \tag{2}$$

where q_j and u_{0j} – the response of the body and the displacements of points on the mid-surface of the shell (when $r = R$ $q_j = \sigma_{rj}$, where σ_{rj} – the stresses in the points of the body), $j = \eta, \theta, r$; $P_\theta(\theta, \eta)$ and $P_r(\theta, \eta)$ – the intensity of the torsional and normal load.

Let's express the vector **u** based on the Lamé potentials φ_j (j = 1, 2, 3) [11]

$$\mathbf{u} = \text{grad}\,\varphi_1 + \text{rot}(\varphi_2\mathbf{e}_\eta) + \text{rot rot}(\varphi_3\mathbf{e}_\eta), \tag{3}$$

where $\mathbf{e}_\eta$ – the unit vector of the axis η.

Using (1) and (3) we obtain:

$$\nabla^2\varphi_j = M_j^2\,\partial^2\varphi_j/\partial\eta^2\,,\ j = 1, 2, 3\,. \tag{4}$$

Here $M_1 = M_p$, $M_2 = M_3 = M_s$.

Let's represent the components of the SSS of the body using Lamé potentials φ_j.

The components of vector **u** (3) in Cartesian (5) and cylindrical (6) moving coordinate systems:

$$\begin{aligned}
u_x &= \frac{\partial\varphi_1}{\partial x} + \frac{\partial\varphi_2}{\partial y} + \frac{\partial^2\varphi_3}{\partial x\partial\eta},\\
u_y &= \frac{\partial\varphi_1}{\partial y} - \frac{\partial\varphi_2}{\partial x} + \frac{\partial^2\varphi_3}{\partial y\partial\eta},\\
u_\eta &= \frac{\partial\varphi_1}{\partial\eta} + m_s^2\frac{\partial^2\varphi_3}{\partial\eta^2};
\end{aligned} \tag{5}$$

$$\begin{aligned}
u_r &= \frac{\partial\varphi_1}{\partial r} + \frac{1}{r}\frac{\partial\varphi_2}{\partial\theta} + \frac{\partial^2\varphi_3}{\partial\eta\partial r},\\
u_\theta &= \frac{1}{r}\frac{\partial\varphi_1}{\partial\theta} - \frac{\partial\varphi_2}{\partial r} + \frac{1}{r}\frac{\partial^2\varphi_3}{\partial\eta\partial\theta},\\
u_\eta &= \frac{\partial\varphi_1}{\partial\eta} + m_s^2\frac{\partial^2\varphi_3}{\partial\eta^2}.
\end{aligned} \tag{6}$$

By applying Hooke's law and considering equations (5) and (6), we can derive the formulas for the components of the stress tensor in both Cartesian (7) and cylindrical (8) coordinates

$$\sigma_{\eta\eta} = (2\mu + \lambda M_p^2)\frac{\partial^2\varphi_1}{\partial\eta^2} + 2\mu m_s^2\frac{\partial^3\varphi_3}{\partial\eta^3},$$

$$\sigma_{yy} = \lambda M_p^2\frac{\partial^2\varphi_1}{\partial\eta^2} + 2\mu\left(\frac{\partial^2\varphi_1}{\partial y^2} - \frac{\partial^2\varphi_2}{\partial x\partial y} + \frac{\partial^3\varphi_3}{\partial y^2\partial\eta}\right),$$

$$\sigma_{xx} = \lambda M_p^2\frac{\partial^2\varphi_1}{\partial\eta^2} + 2\mu\left(\frac{\partial^2\varphi_1}{\partial x^2} + \frac{\partial^2\varphi_2}{\partial x\partial y} + \frac{\partial^3\varphi_3}{\partial x^2\partial\eta}\right),$$

$$\sigma_{x\eta} = \mu\left(2\frac{\partial^2\varphi_1}{\partial\eta\partial x} + \frac{\partial^2\varphi_2}{\partial y\partial\eta} + (1+m_s^2)\frac{\partial^3\varphi_3}{\partial\eta^2\partial x}\right), \tag{7}$$

$$\sigma_{\eta y} = \mu\left(2\frac{\partial^2\varphi_1}{\partial y\partial\eta} - \frac{\partial^2\varphi_2}{\partial x\partial\eta} + (1+m_s^2)\frac{\partial^3\varphi_3}{\partial y\partial\eta^2}\right),$$

$$\sigma_{xy} = 2\mu\left(\frac{\partial^2\varphi_1}{\partial x\partial y} - \frac{\partial^2\varphi_2}{\partial x^2} - \frac{m_s^2}{2}\frac{\partial^2\varphi_2}{\partial\eta^2} + \frac{\partial^3\varphi_3}{\partial x\partial y\partial\eta}\right);$$

$$\sigma_{\eta\eta} = (2\mu + \lambda M_p^2)\frac{\partial^2\varphi_1}{\partial\eta^2} + 2\mu m_s^2\frac{\partial^3\varphi_3}{\partial\eta^3},$$

$$\sigma_{\theta\theta} = \lambda M_p^2\frac{\partial^2\varphi_1}{\partial\eta^2} + \frac{2\mu}{r}\left(\frac{1}{r}\frac{\partial^2\varphi_1}{\partial\theta^2} + \frac{\partial\varphi_1}{\partial r} + \frac{1}{r}\frac{\partial\varphi_2}{\partial\theta} - \frac{\partial^2\varphi_2}{\partial r\partial\theta} + \frac{1}{r}\frac{\partial^3\varphi_3}{\partial\theta^2\partial\eta} + \frac{\partial^2\varphi_3}{\partial r\partial\eta}\right),$$

$$\sigma_{rr} = \lambda M_p^2\frac{\partial^2\varphi_1}{\partial\eta^2} + 2\mu\left(\frac{\partial^2\varphi_1}{\partial r^2} + \frac{1}{r}\frac{\partial^2\varphi_2}{\partial\theta\partial r} - \frac{1}{r^2}\frac{\partial\varphi_2}{\partial\theta} + \frac{\partial^3\varphi_3}{\partial r^2\partial\eta}\right),$$

$$\sigma_{r\eta} = \mu\left(2\frac{\partial^2\varphi_1}{\partial\eta\partial r} + \frac{1}{r}\frac{\partial^2\varphi_2}{\partial\theta\partial\eta} + (1+m_s^2)\frac{\partial^3\varphi_3}{\partial\eta^2\partial r}\right), \tag{8}$$

$$\sigma_{\eta\theta} = \mu\left(\frac{2}{r}\frac{\partial^2\varphi_1}{\partial\theta\partial\eta} - \frac{\partial^2\varphi_2}{\partial r\partial\eta} + \frac{(1+m_s^2)}{r}\frac{\partial^3\varphi_3}{\partial\theta\partial\eta^2}\right),$$

$$\sigma_{r\theta} = 2\mu\left(\frac{1}{r}\frac{\partial^2\varphi_1}{\partial\theta\partial r} - \frac{1}{r^2}\frac{\partial\varphi_1}{\partial\theta} - \frac{\partial^2\varphi_2}{\partial r^2} - \frac{m_s^2}{2}\frac{\partial^2\varphi_2}{\partial\eta^2} + \frac{1}{r}\frac{\partial^3\varphi_3}{\partial r\partial\eta\partial\theta} - \frac{1}{r^2}\frac{\partial^2\varphi_3}{\partial\eta\partial\theta}\right).$$

Applying the Fourier transformation in η to equations (4), we obtain

$$\nabla_2^2\varphi_j^* - m_j^2\xi^2\varphi_j^* = 0, \quad j = 1, 2, 3, \tag{9}$$

where $\varphi_j^*(r,\theta,\xi) = \int_{-\infty}^{\infty}\varphi_j(r,\theta,\eta)e^{-i\xi\eta}d\eta$, $m_j^2 = 1 - M_j^2$, $m_1 \equiv m_p, m_2 = m_3 \equiv m_s$, ∇_2^2 – two-dimensional Laplace operator.

Applying the Fourier transform to (5) – (8) in η, we obtain expressions for the transformants of displacements u_l^* and stresses σ_{lm}^* in Cartesian ($l,m = x,y,\eta$) and cylindrical ($l,m = r,\theta,\eta$) coordinates, represented by φ_j^*.

Let's impose a constraint on the speed of load movement, assuming it is less than the shear wave velocity in the body, i.e. $c < c_s$. Then $M_s < 1$ ($m_s > 0$), and the solutions of equations (9) can be represented as follows

$$\varphi_j^* = \Phi_j^{(1)} + \Phi_j^{(2)}. \tag{10}$$

Here $\Phi_j^{(1)} = \sum_{n=-\infty}^{\infty} a_{nj}K_n(k_j r)e^{in\theta}$, $\Phi_j^{(2)} = \int_{-\infty}^{\infty} g_j(\xi,\zeta)\exp\left(iy\zeta + (x-h)\sqrt{\zeta^2 + k_j^2}\right)d\zeta$, $K_n(kr)$ – MacDonald functions, $k_j = m_j\xi$; a_{nj}, $g_j(\xi,\zeta)$ – unknown functions and coefficients to be determined, $j = 1, 2, 3$.

In the Cartesian coordinates, the expressions for the transformants of potentials (10) will take the form:

$$\varphi_j^* = \int_{-\infty}^{\infty}\left[\frac{e^{-xf_j}}{2f_j}\sum_{n=-\infty}^{\infty}a_{nj}\Phi_{nj} + g_j(\xi,\zeta)e^{(x-h)f_j}\right]e^{iy\zeta}d\zeta\,. \qquad (11)$$

Here $f_j = \sqrt{\zeta^2 + k_j^2}, \Phi_{nj} = \left(\frac{\zeta + f_j}{k_j}\right)^n$, $j = 1, 2, 3.$

Let's express the functions $g_j(\xi,\zeta)$ by the coefficients a_{nj} ($j = 1, 2, 3$). To accomplish this, we will consider (11) and utilize the boundary conditions when $x = h$:

$$\sigma_{xx}^* = \sigma_{xy}^* = \sigma_{x\eta}^* = 0\,.$$

Extracting coefficients of $e^{iy\zeta}$ and equating them to zero, we derive a system of three algebraic equations from which we can deduce

$$g_j(\xi,\zeta) = \frac{1}{\Delta_*}\sum_{l=1}^{3}\Delta_{jl}^* e^{-hf_l}\sum_{n=-\infty}^{\infty}a_{nl}\Phi_{nl}\,. \qquad (12)$$

Here $\Delta_* = \left(2\rho_*^2 - \beta^2\right)^2 - 4\rho_*^2\sqrt{\rho_*^2 - \alpha^2}\sqrt{\rho_*^2 - \beta^2}$,

$$\Delta_{11}^* = \frac{\Delta_*}{2\sqrt{\rho_*^2 - \alpha^2}} - \frac{\left(2\rho_*^2 - \beta^2\right)^2}{\sqrt{\rho_*^2 - \alpha^2}}, \Delta_{12}^* = -2\zeta\left(2\rho_*^2 - \beta^2\right), \Delta_{13}^* = 2\xi\left(2\rho_*^2 - \beta^2\right)\sqrt{\rho_*^2 - \beta^2},$$

$$\Delta_{21}^* = -\frac{M_s^2}{m_s^2}\Delta_{12}^*, \quad \Delta_{22}^* = -\frac{\Delta_{**}}{2\sqrt{\rho_*^2 - \beta^2}}, \quad \Delta_{23}^* = -4\xi\zeta\frac{M_s^2}{m_s^2}\sqrt{\rho_*^2 - \alpha^2}\sqrt{\rho_*^2 - \beta^2},$$

$$\Delta_{31}^* = -\frac{\Delta_{13}^*}{m_s^2\xi^2}, \quad \Delta_{32}^* = \frac{\Delta_{21}^*}{\beta^2}, \quad \Delta_{33}^* = -\frac{\Delta_{**}}{2\sqrt{\rho_*^2 - \beta^2}} + \frac{\left(2\rho_*^2 - \beta^2\right)^2}{\sqrt{\rho_*^2 - \beta^2}},$$

$$\alpha = M_p\xi, \quad \beta = M_s\xi, \quad \rho_*^2 = \xi^2 + \zeta^2, \quad \Delta_{**} = \left(2\rho_*^2 - \beta^2\right)^2 - 4\rho_{**}^2\sqrt{\rho_*^2 - \alpha^2}\sqrt{\rho_*^2 - \beta^2},$$

$$\rho_{**}^2 = \xi^2 + \left(2/m_s^2 - 1\right)\zeta^2.$$

As demonstrated in [1], the determinant $\Delta_*(\xi,\zeta) \neq 0$ for $c < c_R$, where c_R – the Rayleigh surface wave velocity in the half-space [11].

When $c < c_R$, the expressions (11), taking into account (12), will have the following form

$$\varphi_j^* = \int_{-\infty}^{\infty}\left[\frac{e^{-xf_j}}{2f_j}\sum_{n=-\infty}^{\infty}a_{nj}\Phi_{nj} + e^{(x-h)f_j}\sum_{l=1}^{3}\frac{\Delta_{jl}^*}{\Delta_*}e^{-hf_l}\sum_{n=-\infty}^{\infty}a_{nl}\Phi_{nl}\right]e^{iy\zeta}d\zeta\,. \qquad (13)$$

Substituting (13) into the expressions for u_l^* and σ_{lm}^* presented in the Cartesian ($l, m = x, y, \eta$) coordinates, we obtain:

$$u_l^* = \int_{-\infty}^{\infty}\sum_{j=1}^{3}\left(T_{lj}^{(1)}F_{nj}^{(1)} + T_{lj}^{(2)}F_{nj}^{(2)}\right)e^{i(y\zeta+\xi\eta)}d\zeta,$$

$$\frac{\sigma_{lm}^*}{\mu} = \int_{-\infty}^{\infty}\sum_{j=1}^{3}\left(S_{lmj}^{(1)}F_{nj}^{(1)} + S_{lmj}^{(2)}F_{nj}^{(2)}\right)e^{i(y\zeta+\xi\eta)}d\zeta\,.$$

Here:

$$F_{nj}^{(1)} = \frac{e^{-xf_j}}{2f_j}\sum_{n=-\infty}^{n=\infty}a_{nj}\Phi_{nj}, \quad F_{nj}^{(2)} = e^{(x-h)f_j}\sum_{k=1}^{3}\frac{\Delta_{jk}^*}{\Delta_*}e^{-hf_k}\sum_{n}a_{nk}\Phi_{nk}\,,$$

$$T_{x1}^{(1)} = -T_{x1}^{(2)} = -f_1, \quad T_{x2}^{(1)} = T_{x2}^{(2)} = -\zeta, \quad T_{x3}^{(1)} = -T_{x3}^{(2)} = f_3\xi\,,$$

$T_{y1}^{(1)} = T_{y1}^{(2)} = i\zeta, \quad T_{y2}^{(1)} = -T_{y2}^{(2)} = if_2, \quad T_{y3}^{(1)} = T_{y3}^{(2)} = -i\xi\zeta$,

$T_{\eta 1}^{(1)} = T_{\eta 1}^{(2)} = i\xi, \quad T_{\eta 2}^{(1)} = T_{\eta 2}^{(2)} = 0, \quad T_{\eta 3}^{(1)} = T_{\eta 3}^{(2)} = -im_s^2\xi^2$,

$S_{xx1}^{(1)} = S_{xx1}^{(2)} = n_2 + 2(f_1^2 - \xi^2 m_p^2), \quad S_{xx2}^{(1)} = -S_{xx2}^{(2)} = 2\zeta f_2, \quad S_{xx3}^{(1)} = S_{xx3}^{(2)} = -2f_3^2\xi$,

$S_{yy1}^{(1)} = S_{yy1}^{(2)} = n_2 - 2(\zeta^2 + \xi^2 m_p^2), \quad S_{yy2}^{(1)} = -S_{yy2}^{(2)} = -2f_2\zeta, \quad S_{yy3}^{(1)} = S_{yy3}^{(2)} = 2\xi\zeta^2$,

$S_{\eta\eta 1}^{(1)} = S_{\eta\eta 1}^{(2)} = n_2 - 2n_1, \quad S_{\eta\eta 2}^{(1)} = S_{\eta\eta 2}^{(2)} = 0, \quad S_{\eta\eta 3}^{(1)} = S_{\eta\eta 3}^{(2)} = 2m_s^2\xi^3$,

$S_{xy1}^{(1)} = -S_{xy1}^{(2)} = -2f_1\zeta i, \quad S_{xy2}^{(1)} = S_{xy2}^{(2)} = -(f_2^2 + \zeta^2)i, \quad S_{xy3}^{(1)} = -S_{xy3}^{(2)} = 2f_3\xi\zeta i$,

$S_{\eta y1}^{(1)} = S_{\eta y1}^{(2)} = -2\xi\zeta, \quad S_{\eta y2}^{(1)} = -S_{\eta y2}^{(2)} = -\xi f_2, \quad S_{\eta y3}^{(1)} = S_{\eta y3}^{(2)} = n_2\zeta$,

$S_{x\eta 1}^{(1)} = -S_{x\eta 1}^{(2)} = -2f_1\xi i, \quad S_{x\eta 2}^{(1)} = S_{x\eta 2}^{(2)} = -\xi\zeta i, \quad S_{x\eta 3}^{(1)} = -S_{x\eta 3}^{(2)} = n_2 f_3 i$,

$n_1 = (1 + m_p^2)\xi^2, \quad n_2 = (1 + m_s^2)\xi^2$.

To represent the transforms of potentials (7) in the cylindrical coordinate system, we will use the relationship [12]

$$\exp\left(iy\zeta + (x-h)\sqrt{\zeta^2 + k^2}\right) = \sum_{n=-\infty}^{\infty} I_n(kr)e^{in\theta}\left(\frac{\zeta + \sqrt{\zeta^2 + k^2}}{k}\right)^n e^{-h\sqrt{\zeta^2+k^2}}.$$

Here $I_n(kr)$ – modified Bessel functions.

Then

$$\varphi_j^* = \sum_{n=-\infty}^{\infty}\left(a_{nj}K_n(k_j r) + I_n(k_j r)\int_{-\infty}^{\infty} g_j(\xi,\zeta)\,\Phi_{nj}e^{-hf_j}d\zeta\right)e^{in\theta}.$$

When $c < c_R$, these expressions taking into account (12), will take the form

$$\varphi_j^* = \sum_{n=-\infty}^{\infty}\left(a_{nj}K_n(k_j r) + b_{nj}I_n(k_j r)\right)e^{in\theta}, \tag{14}$$

where $b_{nj} = \sum_{l=1}^{3}\sum_{m=-\infty}^{\infty} a_{ml}A_{nj}^{ml}$, $A_{\eta j}^{ml} = \int_{-\infty}^{\infty}\frac{\Delta_{jl}^*}{\Delta_*}\Phi_{ml}\Phi_{nj}e^{-h(f_l+f_j)}d\zeta$.

By substituting (14) into the expressions for u_l^* and σ_{lm}^* represented in the cylindrical ($l, m = r,\ \theta, \eta$) coordinate system, we obtain

$$u_l^* = \sum_{n=-\infty}^{\infty}\sum_{j=1}^{3}\left[T_{lj}^{(1)}\left(K_n(k_j r)\right)a_{nj} + T_{lj}^{(2)}\left(I_n(k_j r)\right)b_{nj}\right]e^{i(\xi\eta + n\theta)},$$

$$\frac{\sigma_{lm}^*}{\mu} = \sum_{n=-\infty}^{\infty}\sum_{j=1}^{3}\left[S_{lmj}^{(1)}\left(K_n(k_j r)\right)a_{nj} + S_{lmj}^{(2)}\left(I_n(k_j r)\right)b_{nj}\right]e^{i(\xi\eta + n\theta)}.$$

Here:

$T_{r1}^{(1)} = k_1 K_n'(k_1 r), \quad T_{r2}^{(1)} = -\frac{n}{r}K_n(k_2 r), \quad T_{r3}^{(1)} = -\xi k_3 K_n'(k_3 r)$,

$T_{\theta 1}^{(1)} = \frac{n}{r}K_n(k_1 r)i, \quad T_{\theta 2}^{(1)} = -k_2 K_n'(k_2 r)i, \quad T_{\theta 3}^{(1)} = -\frac{n}{r}\xi K_n(k_3 r)i$,

$T_{\eta 1}^{(1)} = \xi K_n(k_1 r)i, \quad T_{\eta 2}^{(1)} = 0, \quad T_{\eta 3}^{(1)} = -k_3^2 K_n(k_3 r)i$,

$S_{rr1}^{(1)} = 2\left(k_1^2 + \frac{n^2}{r^2} - \frac{\lambda M_p^2\xi^2}{2\mu}\right)K_n(k_1 r) - \frac{2k_1 K_n'(k_1 r)}{r}$, $S_{rr2}^{(1)} = \frac{2n}{r^2}K_n(k_2 r) - \frac{2k_2 K_n'(k_2 r)}{r}$,

$S_{rr3}^{(1)} = -2\xi\left(k_3^2 + \frac{n^2}{r^2}\right)K_n(k_3 r) + \frac{2\xi k_3 K_n'(k_3 r)}{r}$,

$$S_{\theta\theta 1}^{(1)} = -2\left(\frac{n^2}{r^2} + \frac{\lambda M_p^2 \xi^2}{2\mu}\right) K_n(k_1 r) + \frac{2k_1 K_n'(k_1 r)}{r},\ S_{\theta\theta 2}^{(1)} = -\frac{2nK_n(k_2 r)}{r^2} + \frac{2nk_2 K_n'(k_2 r)}{r},$$

$$S_{\theta\theta 3}^{(1)} = \frac{2\xi n^2 K_n(k_3 r)}{r^2} - \frac{2\xi k_3 K_n'(k_3 r)}{r},$$

$$S_{\eta\eta 1}^{(1)} = -2\xi^2\left(\frac{1+\lambda M_p^2}{2\mu}\right) K_n(k_1 r),\quad S_{\eta\eta 2}^{(1)} = 0,\quad S_{\eta\eta 3}^{(1)} = 2m_3^2 \xi^3 K_n(k_3 r),$$

$$S_{r\theta 1}^{(1)} = \left(-\frac{2nK_n(k_1 r)}{r^2} + \frac{2nk_1 K_n'(k_1 r)}{r}\right) i,\ S_{r\theta 2}^{(1)} = \left(-\left(k_2^2 + \frac{2n^2}{r^2}\right) K_n(k_2 r) + \frac{2k_2 K_n'(k_2 r)}{r}\right) i,$$

$$S_{r\theta 3}^{(1)} = \left(\frac{2n\xi K_n(k_3 r)}{r^2} - \frac{2n\xi k_3 K_n'(k_3 r)}{r}\right) i,$$

$$S_{\theta\eta 1}^{(1)} = -\frac{2n\xi K_n(k_1 r)}{r},\quad S_{\theta\eta 2}^{(1)} = \xi k_2 K_n'(k_2 r),\quad S_{\theta\eta 3}^{(1)} = \frac{n\xi^2\left(1+m_3^2\right) K_n(k_3 r)}{r},$$

$$S_{r\eta 1}^{(1)} = 2\xi k_1 K_n'(k_1 r) i,\quad S_{r\eta 2}^{(1)} = -\frac{\xi n K_n(k_2 r) i}{r},\quad S_{r\eta 3}^{(1)} = -\xi^2 k_3\left(1+m_3^2\right) K_n'(k_3 r) i;$$

$K_n'(kr) = \dfrac{dK_n(kr)}{d(kr)}$; $T_{lj}^{(2)}$, $S_{lmj}^{(2)}$ are obtained from $T_{lj}^{(1)}$, $S_{lmj}^{(1)}$ by replacing $K_n(k_j r)$ with $I_n(k_j r)$.

To determine the unknown coefficients a_{nj} (j = 1, 2, 3) in the expressions for the transformants of displacements u_l^* and stresses σ_{lm}^*, we will use the boundary conditions at $r = R$:

- for a nonreinforced cavity (Fig. 1)

$$\sigma_{rr}^* = P_r^*(\theta,\xi),\ \sigma_{r\theta}^* = -P_\theta^*(\theta,\xi),\ \sigma_{r\eta}^* = 0, \tag{15}$$

where $P_j^*(\theta,\xi) = \int\limits_{-\infty}^{\infty} P_j(\theta,\eta) e^{-i\xi\eta} d\eta = p_j(\theta) p_j^*(\xi),\ p_j(\theta) = \sum\limits_{n=-\infty}^{\infty} P_{nj} e^{in\theta},\ p_j^*(\xi) = \int\limits_{-\infty}^{\infty} p_j(\eta) e^{-i\xi\eta} d\eta,\ j = r, \theta$;

- for cavity reinforcement with a thin shell (Fig. 2)

$$u_l^* = u_{0l}^*, \tag{16}$$

where $u_{0l}^*(\theta,\xi) = \int\limits_{-\infty}^{\infty} u_{0l}(\theta,\eta) e^{-i\xi\eta} d\eta,\ l = \eta, \theta, r$.

By applying the Fourier transformation to (2) in η and expanding the functions $P_j^*(\theta,\xi)$ and $u_{0l}^*(\theta,\xi)$ ($j = \theta, r$, $l = \eta, \theta, r$) into Fourier series in η, we obtain:

$$\varepsilon_1^2 u_{0n\eta} + \nu_2 n\xi_0 u_{0n\theta} - 2i\nu_0 \xi_0 u_{0nr} = -G_0 q_{n\eta},$$
$$\nu_2 n\xi_0 u_{0n\eta} + \varepsilon_2^2 u_{0n\theta} - 2inu_{0nr} = G_0\left(P_{n\theta} - q_{n\theta}\right),$$
$$2i\nu_0 \xi_0 u_{0n\eta} + 2inu_{0n\theta} + \varepsilon_3^2 u_{0nr} = G_0\left(P_{nr} - q_{nr}\right),$$

where $\varepsilon_1^2 = \alpha_0^2 - \varepsilon_0^2,\quad \varepsilon_2^2 = \beta_0^2 - \varepsilon_0^2,\quad \varepsilon_3^2 = \gamma_0^2 - \varepsilon_0^2,\quad \varepsilon_0^2 = \nu_1 \xi_0^2 M_{s0}^2,\quad \xi_0 = \xi R,$

$\alpha_0^2 = 2\xi_0^2 + \nu_1 n^2,\quad \xi_0 = \xi R,\quad \beta_0^2 = \nu_1 \xi_0^2 + 2n^2,\quad \gamma_0^2 = \chi^2\left(\xi_0^2 + n^2\right)^2 + 2,$

$\nu_1 = 1 - \nu_0, \nu_2 = 1 + \nu_0, M_{s0} = \dfrac{c}{c_{s0}},\ c_{s0} = \sqrt{\dfrac{\mu_0}{\rho_0}}, \chi^2 = \dfrac{h_0^2}{6R^2}, G_0 = -\dfrac{\nu_1 R^2}{\mu_0 h_0}$; P_{nj} and u_{0nl} – the coefficients of decomposition $P_j^*(\theta,\xi)$ and $u_{0l}^*(\theta,\xi)$ in the Fourier series by θ; $q_{nl} = (\sigma_{rl}^*)_n$. When $r = R$, $j = \theta, r$, $l = \eta, \theta, r$.

By solving the last equations with respect to u_{0nl} ($l = \eta, \theta, r$) we find:

$$u_{0n\eta} = G_0 \sum_{j=1}^{3} \frac{\delta_{\eta j}}{\delta_n}\left(P_{nj} - q_{nj}\right),$$

$$u_{0n\theta} = G_0 \sum_{j=1}^{3} \frac{\delta_{0j}}{\delta_n} \left(P_{nj} - q_{nj}\right),$$

$$u_{0nr} = G_0 \sum_{j=1}^{3} \frac{\delta_{rj}}{\delta_n} \left(P_{nj} - q_{nj}\right).$$

Here $\delta_n = (\varepsilon_1\varepsilon_2\varepsilon_3)^2 - (\varepsilon_1\xi_1)^2 - (\varepsilon_2\xi_2)^2 + 2\xi_1\xi_2\xi_3$, $\delta_{\eta 1} = (\varepsilon_2\varepsilon_3)^2 - \xi_1^2$, $\delta_{\eta 2} = D_1$, $\delta_{\eta 3} = iD_2$, $\delta_{\theta 1} = D_1$, $\delta_{\theta 2} = (\varepsilon_1\varepsilon_3)^2 - \xi_2^2$, $\delta_{\theta 3} = iD_3$, $\delta_{r1} = -iD_2$, $\delta_{r2} = -iD_3$, $\delta_{r3} = (\varepsilon_1\varepsilon_2)^2 - \xi_3^2$, $\xi_1 = 2n$, $\xi_2 = 2\nu_0\xi_0$, $\xi_3 = \nu_2\xi_0 n$, $D_1 = \xi_0 n\left(4\nu_0 - \varepsilon_3^2\nu_2\right)$, $D_2 = 2\xi_0\left(\varepsilon_2^2\nu_0 - n^2\nu_2\right)$, $D_3 = 2n\left(\varepsilon_1^2 - \xi_0^2\nu_0\nu_2\right)$; $P_{n1} = P_{m\eta} = 0$, $P_{n2} = P_{n\theta}$, $P_{n3} = P_{nr}$, $q_{n1} = q_{m\eta}$, $q_{n2} = q_{n\theta}$, $q_{n3} = q_{nr}$.

By substituting the respective expressions into the boundary conditions (15) or (16) and equating the coefficients of the series with respect to $e^{in\theta}$, for each value of $n = 0, \pm 1, \pm 2, \ldots$, we obtain a system of linear algebraic equations with the determinant $\Delta_n(\xi, c) \neq 0$, from which we find the coefficients a_{nj} (j = 1, 2, 3). Next, by applying the inverse Fourier transform, we compute the displacements u_l and stresses σ_{lm} (l, m = r, θ, η) in the body. In this case, any numerical method can be used, provided that the determinant $\Delta_n(\xi, c) \neq 0$ for each value of $n = 0, \pm 1, \pm 2, \ldots$. Research on determinants $\Delta_n(\xi, c)$ has demonstrated that for an unsupported cavity (Fig. 1), this requirement can be fulfilled by satisfying the condition $c < c_R$. However, for a supported cavity (Fig. 2), the speed of load movement must be lower than its critical speeds $c < c_{(n)^*}$. The values of the critical speeds $c_{(n)^*}$ are determined from the equations $\Delta_n(\xi, c) = 0$. As studies of these equations based on numerical calculations show, the smallest (lowest) critical speed of the load corresponds to the number n = 0 ($\min c_{(n)^*} = c_{(0)^*}$) [1].

Results and Discussion

As an example, let's consider the circular cylindrical cavity depicted in Figure 1 with a radius of R = 1m in a half-space (h = 2R) with the following physical and mechanical properties: $\nu = 0{,}2$, $\mu = 2{,}532 \cdot 10^9$ Pa, $\rho = 2{,}5 \cdot 10^3$ kg/m^3 ($c_s = 1006{,}4$ m/s, $c_R = 917$ m/s). Along its surface, in the direction of the z-axis, an axisymmetric compressive normal load P_r and an axisymmetric torsional load P_θ of equal intensity, P (Pa), are moving with a constant velocity of c = 100 m/s. The loads are uniformly distributed within the interval $|\eta| \le l_0 = 0{,}2R$. In this case, $P_{0j} = 1$, $P_{nj} = 0$ ($n = \pm 1, \pm 2, \ldots$, $j = \theta, r$), $p_r^*(\xi) = -2P\sin(\xi l_0)/\xi$, $p_\theta^*(\xi) = P\sin(\xi l_0)/\xi$. We select the intensities P of the loads in such a way that for each of them, the total load over the entire length of the loading section $2l_0$ equals the equivalent concentrated radial load with an intensity of $P^{\circ\circ}$ (N/m), i.e. $P = P^{\circ\circ}/2l_0$. Then $p_r^*(\xi) = -P^{\circ\circ}\sin(\xi l_0)/(\xi l_0)$, $p_\theta^*(\xi) = P^{\circ\circ}\sin(\xi l_0)/(\xi l_0)$.

In Figure 3, the vertical $u_x^\circ = u_x\mu/P^\circ$, m ($a$) and horizontal $u_y^\circ = u_y\mu/P^\circ$, m ($b$) (where $P^\circ = P^{\circ\circ}$/m, Pa) displacements of the points of the boundary of the half-space are shown in the xy coordinate plane. Curves 1 are plotted for the case of an unsupported cavity (Fig. 1), while curves 2 are for the case when this cavity is reinforced with a thin cast iron (h_0 = 0,05 m; ν_0 = 0,3, $\mu_0 = 5{,}77 \cdot 10^{10}$ Pa, $\rho_0 = 7{,}2 \cdot 10^3$kg/m^3) shell (Fig. 2).

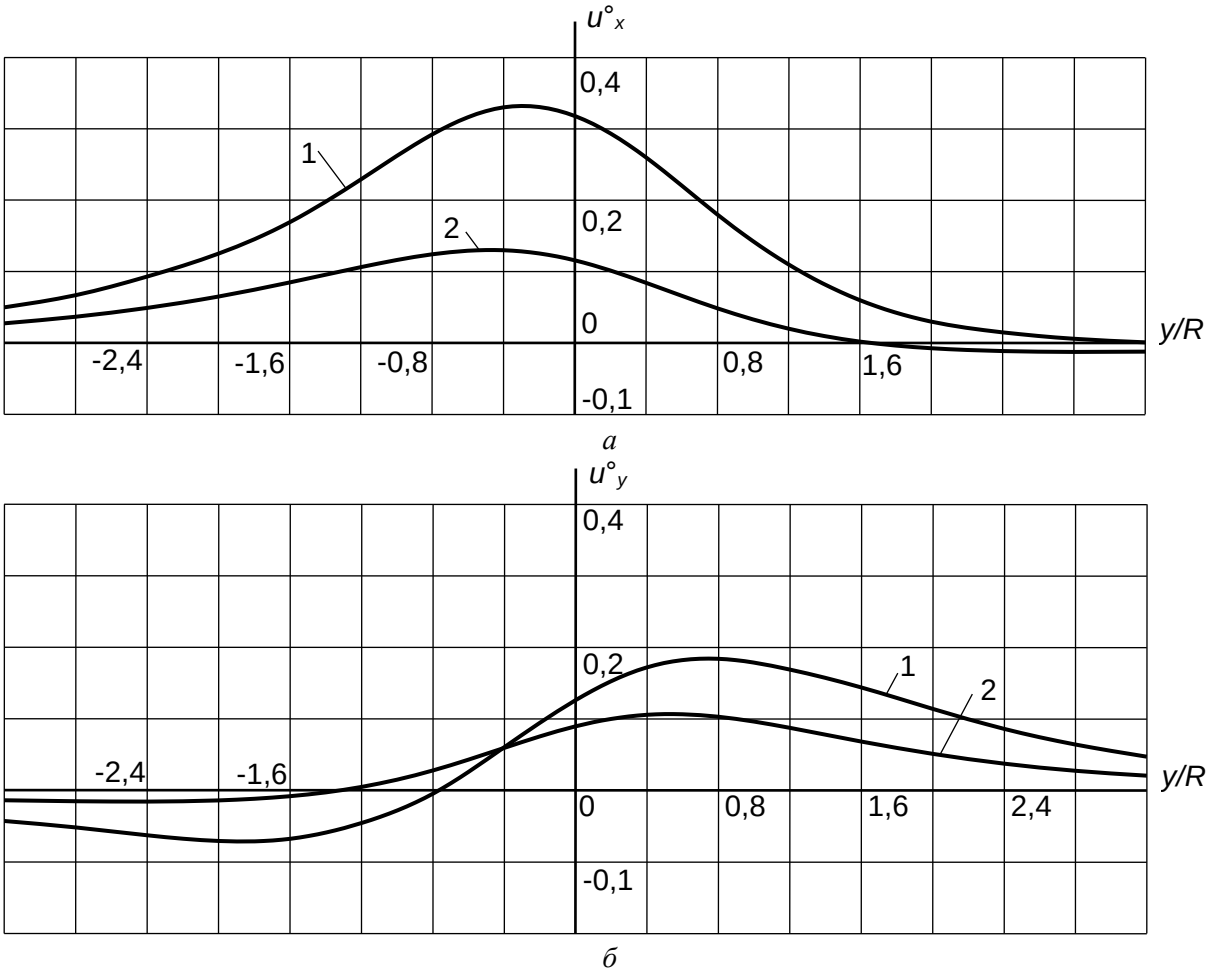

Figure 3. Displacements of points of the boundary of the half-space

From the analysis of the curves, it can be concluded that reinforcing the cavity with a shell leads to a reduction in the dynamic impact of moving loads on the boundary of the half-space.

Conclusion

The problem of the effect of uniformly moving normal and torsional loads along an elongated long circular cylindrical cavity, situated in an elastic half-space (body), on this elastic half-space has been solved. The cavity is either unreinforced or reinforced by a thin-walled elastic shell. Such loading action occurs during the rotational movement of cleaning devices in an underground pipeline and can also arise due to uneven dynamic loads transmitted to each of the rails laid in a cylindrical-shaped tunnel, whether it is supported with a shell or not. When solving the problem, the velocity of load movement is considered to be subsonic. Speed restrictions are imposed: in the case of an unsupported cavity, the speed must be lower than the Rayleigh wave velocity in the half-space, and in the case of a cavity supported by a shell, in addition, the speed must be lower than the critical speeds of the moving loads. In contrast to a similar problem for an elastic space that simulates a deep tunnel, this problem is more complicated, since it becomes necessary to take into account the waves reflected by the boundary of the half-space. In contrast to similar works where the medium is considered as an elastic space, this problem's solution takes into account the effect of waves reflected from the boundary of the half-space, which arise during the movement of loads.

Using the obtained solution and results of numerical experiments, the influence of the shell on the deformed state of the half-space boundary was studied under the action of uniformly applied axisymmetric normal and torsional loads moving at a constant speed within a certain range. The results of the study indicate that reinforcing the cavity with a shell leads to a reduction in the dynamic impact of moving loads on the boundary of the half-space.

References

1 Украинец В.Н. Динамика тоннелей и трубопроводов мелкого заложения под воздействием подвижных нагрузок / В.Н. Украинец. — Павлодар: Изд-во Павлодар. гос. ун-та, 2006. — 123 с.

2 Alexeyeva L.A. Dynamics of an elastic half-space with a reinforced cylindrical cavity under moving loads / L.A. Alexeyeva // International Applied Mechanics. — 2009. — Vol. 45, N 9. — P. 75-85. DOI: 10.1007/s10778-010-0238-z.

3 Coşkun İ. Dynamic Response of a Circular Tunnel in an Elastic Half Space / İ. Coşkun, D. Dolmaseven // Journal of Engineering. — 2017. — Vol. 2017. — 12 p. DOI: 10.1155/2017/6145375.

4 Yuan Z. Benchmark solution for vibrations from a moving point source in a tunnel embedded in a half-space / Z. Yuan, A. Boström, Y. Cai // Journal of Sound and Vibration. — 2017. — Vol. 387. — P. 177-193. DOI: 10.1016/j.jsv.2016.10.016.

5 Zhou Sh. Dynamics of Rail Transit Tunnel Systems / Shunhua Zhou. — Academic Press, 2019. — 276 p.

6 Coşkun İ. Dynamic stress and displacement in an elastic half-space with a cylindrical cavity / İ. Coşkun, H. Enginb, A. Özmutluc // Journal of Shock and Vibration. — 2011. — Vol. 18. — P. 827-838. DOI: 10.1155/2011/904936.

7 Пожуев В.И. Действие подвижной нагрузки на цилиндрическую оболочку в упругой среде / В.И. Пожуев // Строительная механика и расчет сооружений. — 1978. — № 1. — С. 44–48.

8 Пожуев В.И. Действие подвижной скручивающей нагрузки на цилиндрическую оболочку в упругой среде / В.И. Пожуев // Строительная механика и расчет сооружений. — 1984. — № 6. — С. 58–61.

9 Герштейн М.С. Задачи динамики магистральных трубопроводов / М.С. Герштейн, А.Т. Камерштейн, В.И. Прокофьев // Сб.: Расчёт пространственных конструкций. — Вып. 15. — М.: Стройиздат, 1973. — С. 78–86.

10 Дашевский М.А. Прогноз динамических воздействий на сооружения, расположенные вблизи трасс метро / М.А. Дашевский // Строит. механика и расчет сооружений. — 1982. — № 4. — С. 36–40.

11 Новацкий В. Теория упругости / В. Новацкий. — М.: Мир, 1975. — 872 с.

12 Ержанов Ж.С. Динамика тоннелей и подземных трубопроводов / Ж.С. Ержанов, Ш.М. Айталиев, Л.А. Алексеева. — Алма-Ата: Наука, 1989. — 240 с.

В.Н. Украинец, С.Р. Гирнис, К.Т. Макашев, В.Т. Станевич

Серпімді жартылай кеңістіктегі күшейтілмеген және күшейтілген қуысқа қозғалатын қалыпты және бұралу жүктемелерінің әрекеті

Серпімді жартылай кеңістікке (массивке) осы жартылай кеңістікте орналасқан шексіз ұзын дөңгелек цилиндрлік қуыстың жұқа қабырғасының серпімді қабығына бекітілмеген немесе бекітілген бойымен біркелкі қозғалатын қалыпты және бұралу жүктемелерінің әсері зерттелді. Жартылай кеңістік жүктердің әсерінен бос көлденең шекарасы қуыс осіне параллель болады. Жүктердің қозғалу жылдамдығы дыбысқа дейінгі деп қабылданады, яғни жартылай кеңістікте ығысу толқындарының таралу жылдамдығынан аз болады. Массив пен қабықтың қозғалысын сипаттау үшін сәйкесінше Ламе потенциалдарындағы серпімділік теориясының динамикалық теңдеулері және қабық теориясының классикалық теңдеулері пайдаланылған. Теңдеулер жүктемелермен бірге қозғалатын координаттар жүйелерінде (цилиндрлік немесе декарттық) ұсынылған. Жартылай кеңістіктің кернеулі–деформацияланған күйін (КДК) анықтау үшін интегралды Фурье түрлендіру әдісі қолданылады. Массив серпімді кеңістік түрінде ұсынылатын мұндай жұмыстардан айырмашылығы, мұнда есепті шешу кезінде жүктемелердің қозғалысы кезінде пайда болатын жартылай кеңістік шекарасымен шағылысқан толқындардың массивіне әсері ескеріледі. Есепті шешу және әзірленген компьютерлік бағдарламалар негізінде сандық эксперименттер жүргізілді. Сандық эксперименттердің нәтижелері белгілі бір аралықта біркелкі қолданылатын және қалыпты және бұралу жүктемелерінің осимметриялық тұрақты дыбысқа дейінгі және шектен кем қозғалатын жартылай кеңістік шекарасының деформацияланған күйіне қабықтың әсерін көрсететін графиктер түрінде берілген. Осы нәтижелерді талдаудан қуысты қабықпен нығайту қозғалмалы жүктемелердің жартылай кеңістік шекарасына динамикалық әсерінің төмендеуіне әкелетіні шығады.

Кілт сөздер: серпімді жартылай кеңістік, массив, қуыс, цилиндрлік қабық, қозғалмалы жүктеме, жылдамдық, қозғалыс, кернеу.

В.Н. Украинец, С.Р. Гирнис, К.Т. Макашев, В.Т. Станевич

Действие движущихся нормальной и скручивающей нагрузок на неподкреплённую и подкреплённую полость в упругом полупространстве

Исследовано воздействие на упругое полупространство (массив) нормальной и скручивающей нагрузок, равномерно движущихся вдоль неподкрепленной или подкреплённой тонкостенной упругой оболочкой бесконечно длинной круговой цилиндрической полости, находящейся в этом полупространстве. Свободная от действия нагрузок горизонтальная граница полупространства параллельна оси полости. Скорость движения нагрузок принимается дозвуковой, то есть меньше скорости распространения волн сдвига в полупространстве. Для описания движения массива и оболочки используются соответственно динамические уравнения теории упругости в потенциалах Ламе и уравнения классической теории оболочек. Уравнения представляются в перемещающихся вместе с нагрузками системах координат (цилиндрической или декартовой). Для определения напряженно-деформированного состояния полупространства используется метод интегрального преобразования Фурье. В отличие от подобных работ, где массив представляется в виде упругого пространства, здесь при решении задачи учитывается воздействие на массив отраженных границей полупространства волн, возникающих при движении нагрузок. На основе решения задачи и разработанных компьютерных программ проведены численные эксперименты. Результаты численных экспериментов представлены в виде графиков, которые иллюстрируют влияние оболочки на деформированное состояние границы полупространства при действии равномерно приложенных в определенном интервале и движущихся с постоянной дозвуковой и докритической скоростью осесимметричных нормальной и скручивающей нагрузок. Из анализа этих результатов следует, что подкрепление полости оболочкой приводит к снижению динамического воздействия движущихся нагрузок на границу полупространства.

Ключевые слова: упругое полупространство, массив, полость, цилиндрическая оболочка, подвижная нагрузка, скорость, перемещения, напряжения.

References

1 Ukrainets, V.N. (2006). Dinamika tonnelei i truboprovodov melkogo zalozheniia pod vozdeistviem podvizhnykh nagruzok [Dynamics of shallow tunnels and pipelines under the influence of moving loads]. Pavlodar: Izdatelstvo Pavlodarskogo gosudarstvennogo universiteta [in Russian].

2 Alexeyeva, L.A. (2009). Dynamics of an elastic half-space with a reinforced cylindrical cavity under moving loads. *International Applied Mechanics, Vol 45,* 9, 75-85.

3 Coşkun, İ., & Dolmaseven, D. (2017). Dynamic Response of a Circular Tunnel in an Elastic Half Space. *Journal of Engineering, Vol. 2017,* 12 p.

4 Yuan, Z., Boström, A., & Cai, Y. (2017). Benchmark solution for vibrations from a moving point source in a tunnel embedded in a half-space. *Journal of Sound and Vibration, Vol. 387,* 177-193.

5 Zhou, Sh. (2019). Dynamics of Rail Transit Tunnel Systems. Academic Press.

6 Coşkun, İ., Enginb H., & Özmutluc A. (2011). Dynamic stress and displacement in an elastic half-space with a cylindrical cavity. *Journal of Shock and Vibration, Vol. 18*, 827-838.

7 Pozhuev, V.I. (1978). Deistvie podvizhnoi nagruzki na tsilindricheskuiu obolochku v uprugoi srede [The action of a moving load on a cylindrical shell in an elastic medium]. *Stroitelnaia mekhanika i raschet sooruzhenii — Structural Mechanics and Structural Analysis*, 1, 44–48 [in Russian].

8 Pozhuev, V.I. (1984). Deistvie podvizhnoi skruchivaiushchei nagruzki na tsilindricheskuiu obolochku v uprugoi srede [The action of a moving torsional load on a cylindrical shell in an elastic medium]. *Stroitelnaia mekhanika i raschet sooruzhenii — Structural mechanics and calculation of structures*, 6, 58–61 [in Russian].

9 Gershtejn, M.S., Kamershtejn, A.T., & Prokof'ev, V.I. (1973). Zadachi dinamiki magistralnykh truboprovodov [Problems of the dynamics of main pipelines]. In *Raschet prostranstvennykh konstruktsii — Calculation of spatial structures*. Moscow: Stroiizdat, *15, 78–86* [in Russian].

10 Dashevskij, M.A. (1982). Prognoz dinamicheskikh vozdeistvii na sooruzheniia, raspolozhennye vblizi trass [Forecasting dynamic effects on structures located near subway lines]. *Stroitelnaia mekhanika i raschet sooruzhenii — Structural Mechanics and Structural Analysis*, 4, 36–40 [in Russian].

11 Novackij, V. (1975). Teoriia uprugosti [Theory of elasticity]. Moscow: Mir [in Russian].

12 Erzhanov, Zh.S., Ajtaliev, Sh.M., & Alekseeva, L.A. (1989). Dinamika tonnelei i podzemnykh truboprovodov [Dynamics of tunnels and underground pipelines]. Alma-Ata: Nauka [in Russian].

DOI 10.31489/2023PH4/76-81

UDC 669.017.15:621.793.02

Y.Y. Kambarov[1,2*], A.B. Kengesbekov[2], Zh.B. Sagdoldina[3], D.B. Buitkenov[3]

[1]*D. Serikbayev East Kazakhstan Technical University, Ust-Kamenogorsk, Kazakhstan;*
[2]*Plasma Science LLP, Ust-Kamenogorsk, Kazakhstan;*
[3] *S. Amanzholov East Kazakhstan University, Ust-Kamenogorsk, Kazakhstan*
[*]*Corresponding authors e-mail*: *yedilzhan@gmail.com*

Mechanochemical synthesis of AlCoCrFeNi powders via high-energy ball milling

AlCoCrFeNi powders in equimolar ratios were synthesized by mechanochemical synthesis on a high-energy ball milling machine (HEBM). The elemental and phase composition of AlCoCrFeNi powders before and after mechanochemical synthesis were investigated by X-ray phase analysis and scanning electron microscopy with EDS analysis. A preliminary mathematical calculation of the physical parameter responsible for the phase stability of the solid solution valence electron concentration (VEC) showed that the fusion of this system should form the FCC phase. However, the result of XRD analysis showed that during the synthesis a solid solution with FCC and BCC phases was formed. The EDS mapping results of AlCoCrFeNi powders after HEBM showed a homogeneous distribution of elements without macro-segregation. The results presented in this work indicate the formation of a high-entropy alloy of AlCoCrFeNi system in a short time of mechanochemical synthesis. Continuous deformation, fracture and cold welding during mechanochemical synthesis leads to increased diffusion of elements and accounts for the formation of the HEA alloy.

Keywords: high-entropy alloy, mechanochemical synthesis, high-energy ball milling, phase analysis, elemental analysis, particle size distribution.

Introduction

During the last decades, the development of technologies in the field of new materials is moving towards the use of multi-element alloys. This class of metallic compounds is called high-entropy alloys (HEA). HEA consist of five or more elements in equiatomic ratios, where the composition of each element varies from 5 to 35 at. % [1]. The main difference of HEA is the formation of stable thermodynamically stable solid substitution solution mainly with FCC and/or BCC lattice [2]. HEA with a BCC lattice have predominantly high strength and low plasticity, while materials with a FCC lattice have low strength and high plasticity. However, this simple combination of solid solution phases is unlikely to provide the desired matching of strength and ductility without adjusting the phase composition and microstructure. Few literatures mention the effect of simultaneous biphasic (BCC + FCC) on material properties and sometimes the formation of solid solution with HCP lattice. It has been shown that dual phase HEA consisting of FCC and BCC phases are considered to be an effective way to balance strength and ductility.

Mechanical alloying is one of the most effective methods to obtain HEA [3, 4]. Varalakshmi S. and coauthors [5] were the first (2008) to obtain HEA of AlCrCuFeTiZn system exhibiting an BCC structure with crystallite size less than 10 nm using ball milling. Since then, ball milling has become one of the most popular methods to obtain HEA. However, a long mechanical alloying process (usually more than 60 h) is required to obtain HEA powder. It should be noted that many of the apparatuses used in mechanochemical synthesis are designed for milling of matter. HEA synthesis requires apparatuses that generate high energy stress, i.e., a large amount of energy that the working body transfers to the processed substance in the course of mechanical processing in the form of creating defects, to which solid-phase reactions are particularly sensitive. The advantage of using a high-energy ball milling machine for HEA synthesis is in its ability to produce bulk quantities of materials in solid state at room temperature in a short time. In addition, an important parameter in the mechanical synthesis of HEA is the change in temperature, which can determine the nature of the final powder product. If the temperature is high, the associated higher elasticity (higher atomic mobility of atoms) leads to processes leading to reduction (and recrystallization). In such a case, a stable phase is formed, for example, as an intermetallic phase. On the other hand, if the temperature is low, the recovery of defects will be less, and an amorphous (or nanocrystalline) phase is formed [6].

The aim of the present work is to investigate the mechanochemical synthesis of AlCoCrFeNi powders in a high-energy ball milling (HEBM) for 2 h under a controlled temperature regime of 23 °C - 33 °C. The

AlCoCrFeNi system is one of the most widely investigated HEBM systems due to its distinctive thermomechanical properties such as high compressive strength and hardness [7-11].

Experimental

Al, Co, Cr, Fe and Ni powders with purity of 99.7 % and particle sizes of 20-40 μm in equimolar portions were used as starting materials. Mechanical alloying of the powders was carried out in an Emax high-energy ball milling machine (Retsch, Germany) with water cooling for 2 hours at a temperature regime of 23 °C - 33 °C. The acceleration of the balls was 1500 rpm. The mass ratio of the balls to the mass of the loading (powder) was 10:1. The powders were pre-mixed at a ball mill speed of 300 rpm for 15 minutes.

Phase analysis of the synthesized powders was carried out on an X'Per PRO diffractometer, using CuKα-radiation. The microstructure and elemental composition of the synthesized powders were investigated on a TESCAN MIRA3 scanning electron microscope. The particle size distribution of the powders before and after mechanical alloying was analyzed using a laser particle size analyzer (Winner 2005 A Laser Particle Size Analyzer).

Results and Discussion

To predict the formation of solid solutions in the AlCoCrFeNi system, we used the basic parameters of the HEA calculation [6] based on the Hume-Rothery rules, i.e., taking into account the composition-weighted terms for differences in atomic radii (δr) and average valence electron concentration (VEC), using data from Table.

The calculation formulas for the parameters are as follows:

$$\delta r = 100\%\sqrt{\sum c_i(1 - r_i/\bar{r})^2}, \quad (1)$$

where c_i – content (at. %) *i*- th element in the alloy, r_i – tomic radius of the *i*- th element in the alloy, $\bar{r} = \sum c_i r_i$- average atomic radius of the alloy.

$$VEC = \sum_{i=1}^{n} c_i \, (VEC)_i, \quad (2)$$

where (VEC)*i* is a valence electron concentration.

T a b l e

Properties of the elements under consideration [7]

Elements	Atomic number	Structure	Radius, pm	T_m, K	VEC	Pauling EN
Al	13	FCC	143.70	933	13	1.61
Co	27	FCC	125.10	1768	9	1.88
Cr	24	BCC	124.91	2180	6	1.66
Fe	26	BCC	124.12	1811	8	1.83
Ni	28	FCC	124.59	1728	10	1.91

The atomic size difference (δr) for our composition is 5.9 %, which is within the accepted range of $0 \leq \delta r \leq 8{,}5$ % [7]. VEC =9.2 enters the range of VEC≥8, hence a single FCC phase is predicted [12].

X-ray diffraction patterns of equiatomic AlCoCrFeNi powder before and after mechanical alloying are presented in Figure 1. In the initial state (stirred for 15 minutes), diffraction lines corresponding to the elemental composition of AlCoCrFeNi powder are visible. According to X-ray phase analysis after 2 h HEBM, BCC and FCC phases are formed after 2 h HEBM. The diffraction peak of Al at 2θ=38.46° disappears. The dissolution of Co and Ni in each other results in the formation of FCC phase. According to the results of [13-16] over 10 hours mechanical alloying at 200-300 rpm, the BCC phase prevails in the AlCoCrFeNi system. Also, in [14] it is reported that after 20 hours treatment B2 phase is formed and complete amorphization of the structure occurs at 84 hours treatment.

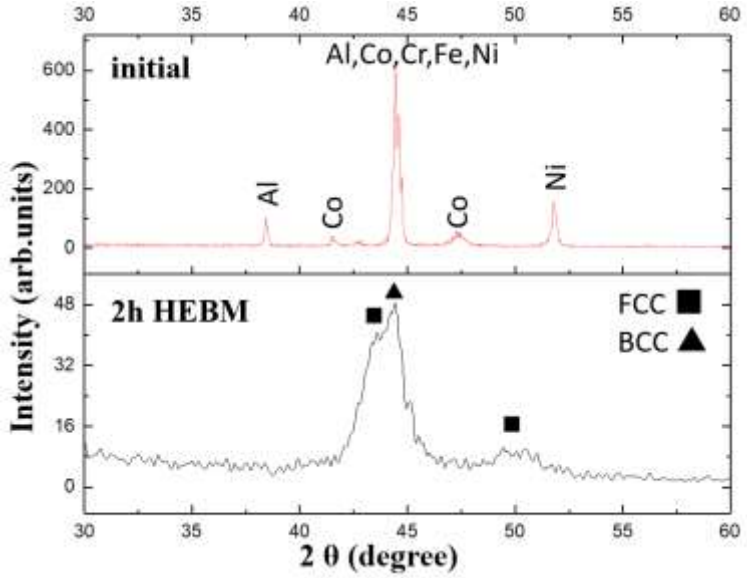

Figure 1. X-ray diffraction patterns of equiatomic AlCoCrFeNi powder before and after HEBM

The chemical composition of the powder before and after HEBM was analyzed by EDS mapping (Fig. 2). The EDS mapping results of AlCoCrFeNi powders after HEBM showed a homogeneous distribution of elements without macrosegregation (Fig. 3). This indicates that the initial powders have completely reacted with each other, and the BCC and FCC phases were successfully synthesized in the process. Probably, in the process of mechanical alloying, continuous deformation, fracture and cold-welding lead to increased diffusion of elements, which accounts for the formation of the HEA.

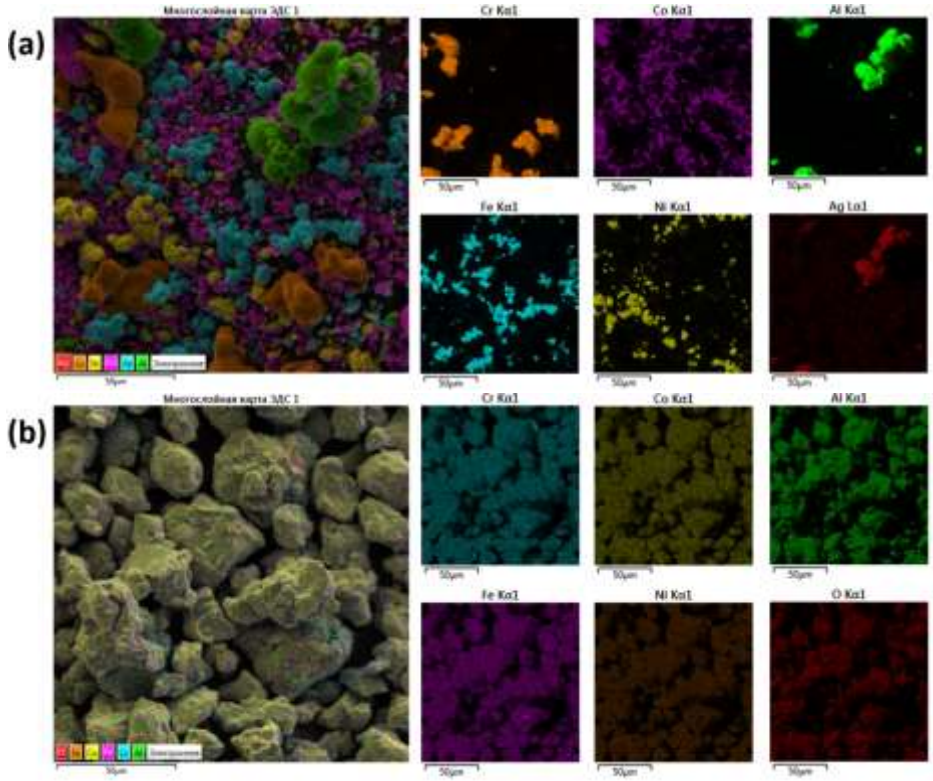

Figure 2. Elemental mapping results of AlCoCrFeNi powders (a) mixed state; (b) after HEBM for 2 hours.

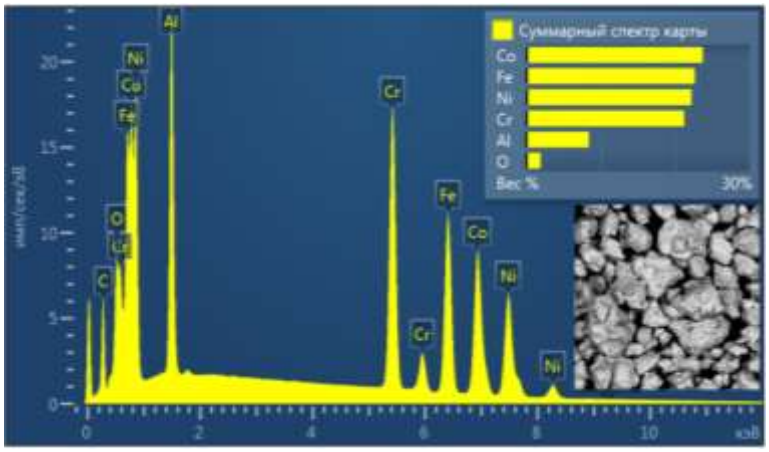

Figure 3. Total EDS spectrum mapping of AlCoCrFeNi powder after HEBM for a time of 2 hours

Figure 4 shows the results of the particle size distribution of the powders before and after HEBM. The initial powder size ranges from 13 μm to 36 μm, and after HEBM the powder size varies from 27 μm to 49 μm. The increase in the average particle size is due to the predominance of the agglomeration process over the fracture process. The particle size distribution data coincide with the results obtained using electron microscopy (Fig. 2).

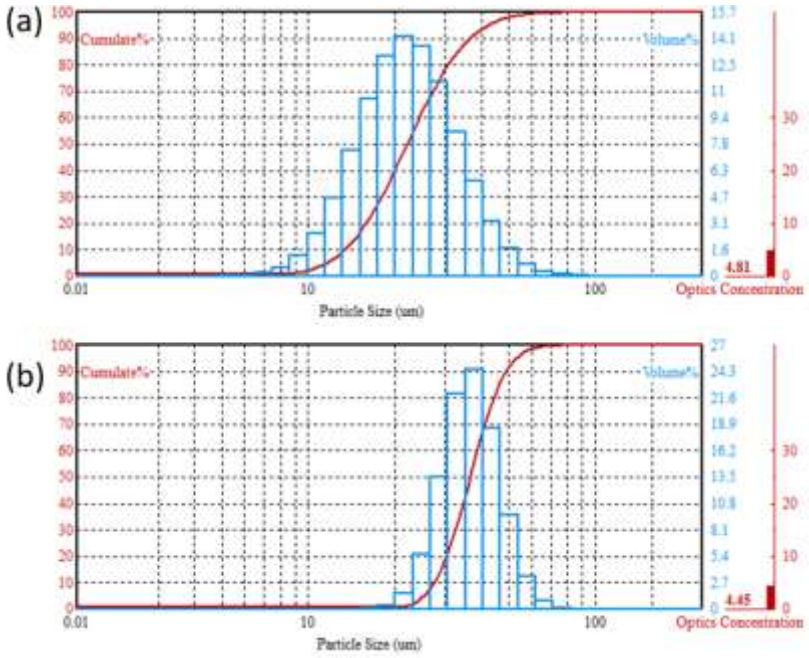

Figure 4. Particle size distribution of AlCoCrFeNi HEA particles (a) mixed state; (b) after HEBM for 2 h.

Conclusion

The elemental, phase and particle size distribution of AlCoCrFeNi powders before and after mechanochemical synthesis in a high-energy ball mill (HEBM) for 2 h under a controlled temperature regime of 23 °C - 33 °C were investigated. According to the results of XRD analysis, a solid solution with BCC and FCC structure is formed after mechanochemical synthesis. The formation of intermetallic and oxide compounds was not detected. EDS mapping results of AlCoCrFeNi powders after HEBM showed homogeneous distribution of elements without macro-segregation. The particle size distribution of the powder after HEBM ranged from 27 μm to 49 μm.

The conducted study is the first step in the development of a method for obtaining HEBM of the AlCoCrFeNi system mechanically activated in an Emax high-energy ball milling machine. The results presented

in this work indicate the possibility of synthesizing AlCoCrFeNi HEA in a short time of mechanochemical synthesis.

Acknowledgements.

This research has been funded by the Science Committee of the Ministry of Science and Higher Education of the Republic of Kazakhstan (Grant No. AP14972882).

References

1 Yeh, J-W. (2006). Recent progress in high-entropy alloys. *Annales de Chimie - Science des Matériaux, Vol. 31,* 633-648. DOI: 10.3166/acsm.31.633-648

2 Pogrebnjak, A.D., Bagdasaryan, A.A., Yakushchenko, I.V., & Bersenov, V.M. (2014). The structure and properties of high-entropy alloys and nitride coatings based on them. *Russian Chemical Reviews, Vol. 83*(11), 1027. DOI: 10.1070/RCR4407

3 Fu, Z.Q., Chen, W.P., Wen, H.M., Zhang, D.L., Chen, Z., Zheng, B.L., Zhou, Y.Z., & Lavernia, E.J. (2016). Microstructure and strengthening mechanisms in an FCC structured single-phase nanocrystalline Co25Ni25Fe25Al7.5Cu17.5 high-entropy alloy. *Acta Materialia, Vol. 107,* 59-71. DOI: 10.1016/j.actamat.2016.01.050

4 Ji, W., Fu, Z., Wang, W., Wang, H., Zhang, J., Wang, Y., & Zhang, F. (2014). Mechanical alloying synthesis and spark plasma sintering consolidation of CoCrFeNiAl high-entropy alloy. *Journal of Alloys and Compounds, Vol. 589,* 61-66. DOI: 10.1016/j.jallcom.2013.11.146

5 Varalakshmi, S., Kamaraj, M., & Murty, B.S. (2008). Synthesis and characterization of nanocrystalline AlFeTiCrZnCu high entropy solid solution by mechanical alloying. *Journal of Alloys Compounds, Vol. 460,* 253–257. DOI: 10.1016/j.jallcom.2007.05.104

6 Zhao, Y., Yang, T., Tong, Y., Wang, J., Luan, J., Jiao, Z., Chen, D., Yang, Y., Hu, A., Liu, C., & Kai, J. (2017). Heterogeneous precipitation behavior and stacking-faultmediated deformation in a CoCrNi-based medium-entropy alloy. *Acta Materialia, Vol. 138,* 72-82. DOI: 10.1016/j.actamat.2017.07.029

7 Miracle, D., & Senkov, O. (2017). A critical review of high entropy alloys and related concepts. *Acta Materialia, Vol. 122,* 448-511. DOI: 10.1016/j.actamat.2016.08.081

8 Vaidya, M., Prasad, A., Parakh, A., & Murty, B. (2017). Influence of sequence of elemental addition on phase evolution in nanocrystalline AlCoCrFeNi: Novel approach to alloy synthesis using mechanical alloying. *Materials & Design, Vol. 126,* 37-46. DOI: 10.1016/ j.matdes.2017.04.027

9 Miracle, D., Miller, J., Senkov, O., Woodward, C., Uchic, M., & Tiley J. (2014). Exploration and development of high entropy alloys for structural applications. *Entropy, Vol. 16*(No. 11), 494-525. DOI: 10.3390/e16010494

10 Kumar, A., Singh, A., & Suhane, A. (2022). Mechanically alloyed high entropy alloys: existing challenges and opportunities. *Journal of materials research and technology, Vol. 17,* 2431-2456. DOI: 10.1016/j.jmrt.2022.01.141

11 Tsai, M-H. (2013). Physical properties of high entropy. *Entropy, Vol. 15*(12), 5338-5345. DOI: 10.3390/e15125338

12 Guo, S., Ng, C., Lu, J., & Liu, C. (2011). Effect of valence electron concentration on stability of fcc or bcc phase in high entropy alloys. *Journal of Applied Physics, Vol. 109,* A. 103505. DOI: 10.1063/1.3587228

13 Rakhadilov, B.K., Baizhan, D.R., Sagdoldina, Z.B., & Torebek, K. Research of regimes of applying coats by the method of plasma electrolytic oxidation on Ti-6Al-4V. *Bulletin of the University of Karaganda-Physics*. doi/10.31489/2022PH1/99-106

14 Wei, L., Liu, X., Gao, Y., Peng, X., Hu, N., & Chen, M. (2021). Phase, microstructure and mechanical properties evaluation of AlCoCrFeNi high-entropy alloy during mechanical ball milling. *Intermetallics, Vol. 138,* A. 107310. DOI: 10.1016/j.intermet.2021.107310

15 Zhang Y., Zhang, B., Li, K., Zhao, G.L., & Guo S.M. (2016). Electromagnetic interference shielding effectiveness of high entropy AlCoCrFeNi alloy powder laden composites. *Journal of Alloys and Compounds, Vol. 734,* 220-228. DOI: 10.1016/j.jallcom.2017.11.044

16 Chen J., Niu, P., Wei, T., Hao, L., Liu, Y., Wang, X., Peng, Y. (2015). Fabrication and mechanical properties of AlCoNiCrFe high-entropy alloy particle reinforced Cu matrix composites. *Journal of Alloys and Compounds, Vol. 649,* 630-634. DOI: 10.1016/j.jallcom.2015.07.125

Е.Е. Қамбаров, А.Б. Кенесбеков, Ж.Б. Сағдолдина, Д.Б. Буйткенов

Жоғары энергиялы шарлы диірменде AlCoCrFeNi ұнтақтарының механохимиялық синтезі

Эквимолярлы қатынастағы AlCoCrFeNi ұнтақтары жоғары энергетикалық шарлы диірменнің (ЖЭШД) көмегімен механохимиялық синтез арқылы синтезделді. Рентгендік фазалық талдау және ЭҚК талдауы бар сканерлеуші электронды микроскопия әдістерімен механохимиялық синтезге дейінгі және одан

кейінгі AlCoCrFeNi ұнтақтарының элементтік және фазалық құрамы зерттелді. Валенттік электрондар концентрациясындағы (ВКЭ) қатты ерітіндінің фазалық тұрақтылығына жауап беретін физикалық параметрге алдын-ала математикалық есеп жүргізілді, яғни бұл жүйе балқытылған кезде ЦҚТ (ГЦК) фазасының пайда болуы керек екенін көрсетті. Алайда рентгенфазалық талдау нәтижесі синтез кезінде ЦҚТ және КЦТ фазалары бар қатты ерітінді түзілгені берілген. ЖЭШД-ден кейін AlCoCrFeNi ұнтағын картаға түсіргенде EDS нәтижелері макро сегрегациясыз элементтердің біркелкі таралғанын көрсетті. Бұл жұмыста ұсынылған нәтижелерде механохимиялық синтездің қысқа уақытында AlCoCrFeNi жоғары энтропиялық қорытпа жүйесінің түзілгені айтылған. Механохимиялық синтез кезінде үздіксіз деформация, деструкция және суық дәнекерлеу элементтердің диффузиясының жоғарылауына және ЖЭҚ түзілуіне әкеледі.

Кілт сөздер: жоғары энтропиялық қорытпа, механохимиялық синтез, жоғары энергетикалық шарлы диірмен, фазалық талдау, элементтік талдау, гранулометриялық құрамы.

Е.Е. Қамбаров, А.Б. Кенесбеков, Ж.Б. Сагдолдина, Д.Б. Буйткенов

Механохимический синтез порошков AlCoCrFeNi на высокоэнергетической шаровой мельнице

Порошки AlCoCrFeNi в эквимолярном соотношении были синтезированы методом механохимического синтеза на высокоэнергетической шаровой мельнице (ВЭШМ). Методами рентгенофазового анализа и сканирующей электронной микроскопии с ЭДС анализом были исследованы элементный и фазовый составы порошков AlCoCrFeNi до и после механохимического синтеза. Проведен предварительный математический расчет физического параметра, отвечающий за фазовую стабильность твердого раствора концентрации валентных электронов, который показал, что при сплавлении данной системы должна образоваться фаза ГЦК. Однако результат рентгенофазового анализа свидетельствует о том, что во время синтеза образовался твердый раствор с ГЦК и ОЦК фазами. Результаты EDS картирования порошков AlCoCrFeNi после ВЭШМ показали однородное распределение элементов без макросегрегации. Представленные в данной работе результаты свидетельствуют об образовании высокоэнтропийного сплава системы AlCoCrFeNi за короткое время механохимического синтеза. Непрерывная деформация, разрушение и холодная сварка при механохимическом синтезе приводят к повышению диффузии элементов и обусловливают образование сплава ВЭС.

Ключевые слова: высокоэнтропийный сплав, механохимический синтез, высокоэнергетическая шаровая мельница, фазовый и элементный анализ, гранулометрический состав.

DOI 10.31489/2023PH4/82-90

UDC 662.99

B.R. Nussupbekov[1], M.S. Ovcharov[1], E.Z. Oshanov[1], U.B. Yesbergenov[2*], M.S. Duisenbayeva[1], A.A. Tishbekov[1], M.K. Amanzholova[1]

[1]Karaganda Buketov University, Kazakhstan;
[2]"BILGE-ORAZ" LLP, Kazakhstan
[*]Corresponding authors e-mail: m_o_l_d_i_r_89@mail.ru

Determination of the effects of the diameters of the throttle holes on the fluid flow of an inertial hydrodynamic installation

In the article, in order to solve environmental problems associated with heating buildings and structures, the methods of converting electrical energy into thermal energy and the processes occurring at the same time are considered. Well-known thermal installations, such as vortex, cavitation, cavitation-vortex, rotary, do not fully meet the requirements of consumers. In these conditions, the search for effective solutions is an urgent task. Such solutions include a method of obtaining thermal energy by creating pressure at the throttle openings by inertia forces of a rotating mass of liquid. To determine the flow of liquid through the throttle holes, an experimental stand was made. With the help of the stand, we determined the flow rate of liquid through throttle holes with a diameter of 1.5, 2, 3 mm. During the experiment, it was found that the larger the diameter of the throttle opening, the higher the fluid flow. However, it is impossible to excessively increase the diameter of the throttle opening, as this will complicate the creation of pressure at the throttle openings. It is found that with an increase in the angular velocity of the rotor, the fluid pressure at the throttle openings increases, and the proportion of fluid flow from the preliminary static pressure in the total flow decreases. It is certain that the preliminary static pressure in the supply line has a significant effect on the flow rate only at low rotor speeds (ω up to = 76 rad / s), and with increasing angular velocity, its influence decreases and the coefficient *k* tends to 1.

Keywords: vortex effect, cavitation, swirling flow, kinetic energy, choke hole, liquid.

Introduction

In hydrodynamic heaters, thermal energy is generated by activation by external sources of internal energy of the liquid. These include vortex, cavitation-vortex and throttle types of heaters [1].

Vortex liquid heaters are a type of heat exchange devices that use the Zh. Ranka effect to heat or cool liquids. The wound. The vortex effect, or the Wound effect, manifests itself in a swirling flow of a viscous compressible fluid and is realized in a very simple device called a vortex tube [2]. When a liquid passes through a vortex tube, vortices and turbulent flows are created. This contributes to more intensive mixing of the liquid and more efficient heat exchange between the heated liquid and the environment [3].

One of the main advantages of vortex heaters is the high efficiency of heat transfer, since the vortex movements and turbulence created inside the device contribute to more intensive mixing of the liquid, which increases the efficiency of heat transfer.

However, vortex heaters have some disadvantages. Vortex elements may be subject to wear and require regular maintenance and replacement. In addition, the use of vortex heaters may require higher initial investments compared to traditional methods of heat generation.

Devices using vortex technology to generate heat are known. When exposed to water by an external force field of a mechanical type, for example, created by an electric pump, it is possible to obtain thermal energy due to:

1) dissipation of the energy of vortex motion due to the irreversible process of dissipation of part of the mechanical energy of motion due to viscous friction and the transfer of this energy into heat;

2) reversible phase transitions of water from the free state to an ordered, close to the liquid crystal state, in which the specific heat capacity of water in this phase is two times less than in the free state. Since during mechanical treatment of water in a reactor of a fixed volume, accompanied by cavitation, part of the water passes into a liquid crystal state, this exothermic phase transition is accompanied by the release of excess heat [4].

In the article [5], the methods of heating the hydraulic drive working fluid when operating at low temperatures are considered. The method of increasing the durability of a hydraulic drive operating at low temperatures is preheating the working fluid by throttling. The authors of the work proposed a design of a heating throttle with automatic regulation of the conditional passage remotely depending on the temperature of the working fluid in the hydraulic system tank and presented a method for calculating the main parameters of the proposed throttle. However, the authors of the works do not show the results of the calculation.

The paper [6] presents the results of a hydrodynamic liquid heater. The difference between this installation and other heaters is that it allows you to significantly simplify the design and increase the efficiency of the heating process. The main principle of its operation is the direct conversion of mechanical energy into thermal energy. As a result, the efficiency of the heater is 80%. However, the author of the works did not show the experimental data of the proposed installation.

It is shown in [7] that on modern supersonic aircraft, due to aerodynamic heating of the skin, the environment surrounding the hydraulic system has a temperature that is much higher than the permissible for the liquids used. Therefore, when creating hydraulic systems of such aircraft, it is impossible to use a convective heat exchange cycle to maintain a given liquid temperature. In this regard, the authors of the works considered stationary and non-stationary modes of operation of the hydraulic system, their calculation, determination of the temperature of the working fluid, methods of maintaining its set temperature. The obtained data allows us to estimate the surface temperature.

The article [8] presents the results of laboratory studies of hydrodynamic liquid heaters. The calculated data is shown. However, the proposed shape and diameter of the throttle valves do not allow to increase the required temperature. This requires an increase in the applied pressure. The maximum heating temperature of existing heaters is 56 °C.

The vortex technologies used for the autonomous heating system are based on the Rank–Hilsch effect. In most works, the mechanism of separation of the swirling flow into a cooled core and hot peripheral layers, as well as the thermogasodynamic parameters of devices implementing the vortex effect, are investigated. The presence of screw-shaped vortex structures in swirling flows and the significant influence of the precession of the vortex core on the energy separation process have been experimentally established. According to the hypothesis of vortex interaction, the energy separation process is the result of the interaction of two vortices moving along the axis towards each other, where the peripheral one rotates according to the law of a potential vortex, and the axial one according to the law of a quasi-solid body.

It is important to note that energy separation in the vortex interaction hypothesis is a complex and multifaceted phenomenon that requires detailed study and analysis using numerical models, experiments and theoretical approaches.

A physical phenomenon like cavitation occurs when the pressure in a certain area of a liquid decreases to a level at which the liquid begins to evaporate, forming bubbles. Then, when the pressure around the bubbles rises again, the kinetic energy of the colliding particles at the moment of closing of the bubbles causes local hydraulic micro-shocks, accompanied by high pressure and temperature drops in the centers of the bubbles (according to calculations, temperatures can reach values of 1000-1500 °. With and above and the local pressure can reach 150-200 MPa.

The work [9] is devoted to the study of the parameters of the installation for heating the coolant using liquid injection through throttle openings. A scheme of a full-size experimental stand has been developed and the principles of its operation are described in detail. For visual observation of the state of the liquid at different angular speeds of rotation of the rotor, a transparent drum model is made. However, the transparent model is subject to deformations with strong rotation, and it is also difficult to evaluate the data.

In the case when the closing of bubbles occurs near the walls of the hydraulic system, continuous micro-impacts can cause mechanical erosion and local damage to surfaces. Due to high temperatures and the presence of oxygen in the air, active oxidation of surfaces occurs. Oxidative processes are further aggravated by the fact that dissolved air in a liquid contains almost one and a half times more oxygen than atmospheric air.

Experimental

To determine the flow of liquid through the throttle holes, an experimental stand was made [10].

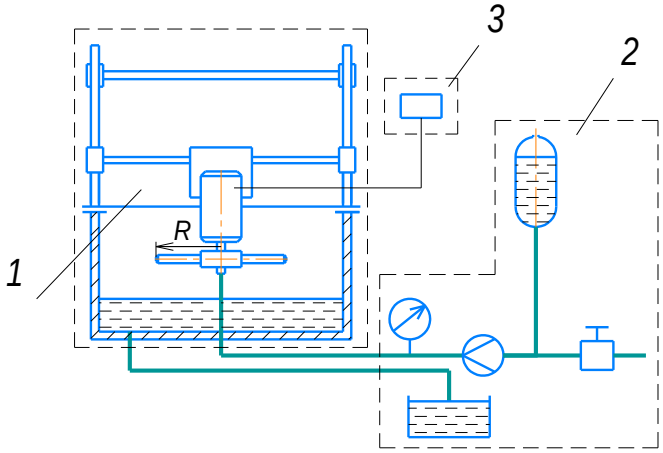

Figure 1. Scheme of the experimental stand 1-main unit, 2-hydraulic unit, 3-power supply unit

The stand allows for the study of liquid forcing through throttle holes with a diameter of 1.5, 2, 3 mm, located at a distance of 0.235 m from the center of rotation of the rotor, with a static height of the liquid column equal to 1.0 m (9796.462 Pa).

The opening of the valve 13 ensures the beginning of water flow through the supply line 9 to the throttle openings, as soon as the column of liquid in the accumulator 12 reaches a predetermined level, readings are taken from the flow meter 11. The liquid flow rate (Q_n) is fixed for the angular velocities of the rotor varying in the range 0...314 rad/s.

When the electric motor 4 is switched on, the mass of liquid inside the rotor is rotated. Inertial forces arise in the rotating mass of the liquid, which create pressure in the radial direction in front of the throttle openings.

It is known that when the rotor rotates, the liquid in the drum cavity tends to the periphery, thereby forming a ring of liquid, the cross section of which directly affects the pressure at the throttle openings. Since the distance from the center of rotation to the throttle holes (R) remains constant, equal to 0.235 m, the pressure value is affected only by the change in angular velocity.

Results and Discussion

The flow of liquid through the throttle holes depends on several factors, such as the diameter of the hole, the pressure of the liquid in front of the hole, the viscosity of the liquid, the length and shape of the channel in front of the hole, etc.

For an ideal frictionless fluid, the flow rate of the fluid through the throttle orifice can be calculated using the Torriceli-Chazele equation. However, in practice, due to friction and other losses, the fluid flow rate may be less than that calculated using the Torriceli-Chazele equation. Therefore, for a more accurate calculation of fluid flow through the throttle opening, it is necessary to take into account factors related to specific operating conditions and the design of the system.

The theoretical flow of liquid through the throttle openings is calculated by the expression

$$Q_m = S\sqrt{\frac{2Pg}{\gamma}}, \quad (1)$$

where S - the area of the throttle opening.

With a constant radius of the rotor drum, having previously assumed the internal cross-section diameters of the liquid ring equal to 0.4, 0.3, and 0.2 m, it is possible to determine the calculated values of the liquid pressure at the throttle openings [10].

According to the expression (1), we determine the theoretical flow rate of the liquid for the diameters of the throttle orifice 1.5, 2, 3 mm, using the calculated pressures. The results of the theoretical flow rate are included in Tables 1-3.

Table 1

Theoretical fluid flow through a 1.5 mm diameter choke hole, at different positions of the fluid ring

Angular velocity of the rotor, ω (rad/s)	Theoretical fluid flow rate (Q_{m1}) through the throttle opening, at different radii of the inner ring of fluid in the rotor drum (m^3/s)			
	r_1=0,4 (m)	r_2=0,3 (m)	r_3=0,2 (m)	r_4=0,0 (m)
0	0,00	0,00	0,00	0,00
42	6,968E-05	9,29E-05	0,000106	0,000116
76	0,00012609	0,000168	0,000193	0,00021
136	0,00022563	0,000301	0,000345	0,000376
215	0,00035669	0,000476	0,000545	0,000594
314	0,00052094	0,000695	0,000796	0,000868

Table 2

Theoretical fluid flow through a 2 mm diameter choke hole, at different positions of the fluid ring

Angular velocity of the rotor, ω (rad/s)	Theoretical fluid flow rate (Q_{m2}) through the throttle opening, at different radii of the inner ring of fluid in the rotor drum (m^3/s)			
	r_1=0,4 (m)	r_2=0,3 (m)	r_3=0,2 (m)	r_4=0,0 (m)
0	0,00	0,00	0,00	0,00
42	0,00012387	0,000165	0,000189	0,000206
76	0,00022415	0,000299	0,000342	0,000374
136	0,00040111	0,000535	0,000613	0,000669
215	0,0006341	0,000845	0,000969	0,001057
314	0,00092609	0,001235	0,001415	0,001543

Table 3

Theoretical fluid flow through a 3 mm diameter choke hole, at different positions of the fluid ring

Angular velocity of the rotor, ω (rad/s)	Theoretical fluid flow rate (Q_{m3}) through the throttle opening, at different radii of the inner ring of fluid in the rotor drum (m^3/s)			
	r_1=0,4 (m)	r_2=0,3 (m)	r_3=0,2 (m)	r_4=0,0 (m)
0	0,00	0,00	0,00	0,00
42	0,00027871	0,000372	0,000426	0,000465
76	0,00050433	0,000672	0,00077	0,000841
136	0,00090249	0,001203	0,001379	0,001504
215	0,00142673	0,001902	0,002179	0,002378
314	0,0020837	0,002778	0,003183	0,003473

According to Tables 1-3, the larger the diameter of the throttle opening, the higher the theoretical fluid flow. However, it is impossible to indefinitely increase the diameter of the throttle hole, as this will complicate the creation of pressure at the throttle holes.

Considering that the stand [2] provides a preliminary static fluid P_n pressure inside the rotor, expression (2) will take the form

$$Q_{\Sigma m} = S\sqrt{\frac{2(P+P_n)g}{\gamma}}, \tag{2}$$

where P_n - preliminary static pressure of the liquid in the supply line.

According to expression (2), we determine the theoretical flow rate of the liquid for the diameters of the throttle opening 1.5, 2, 3 mm, taking into account the preliminary static pressure of the liquid P_n in the system. The results of the total theoretical consumption are shown in Figures 2-4.

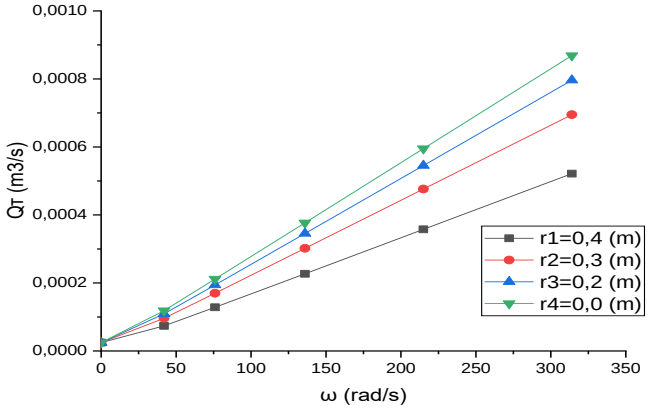

Figure 2. Total theoretical fluid flow through a 1.5 mm diameter choke hole, at different positions of the fluid ring

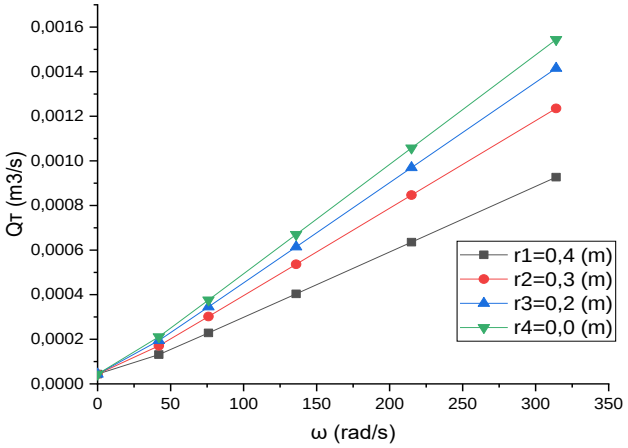

Figure 3. Total theoretical fluid flow through a 2.0 mm diameter choke hole, at different positions of the fluid ring

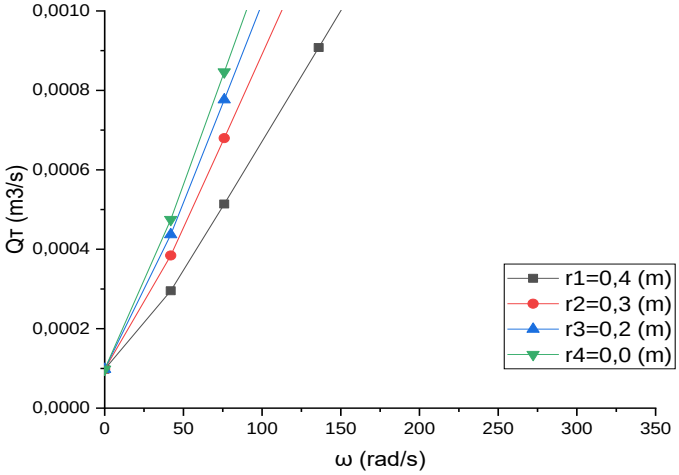

Figure 4. The total theoretical flow of liquid through the throttle hole with a diameter of 3.0 mm, at different positions of the liquid ring

According to formula (1), with an increase in the angular velocity of the rotor, the fluid pressure at the walls of the throttle opening increases, then the proportion of fluid flow from the preliminary static pressure in the total flow decreases. The relationship between expressions (1) and (2) can be represented as

$$Q_m = k \cdot Q_{\Sigma m}, \quad (3)$$

where: k - the coefficient of distribution of fluid flow from static pressure for different angular velocities of the rotor.

From expression (3), the coefficient can be defined as the ratio of the theoretical flow rate to the total theoretical flow rate, and since the flow rates depend on the angular velocity and cross section of the fluid ring in the rotor drum, these dependence graphs are shown in Figure 5.

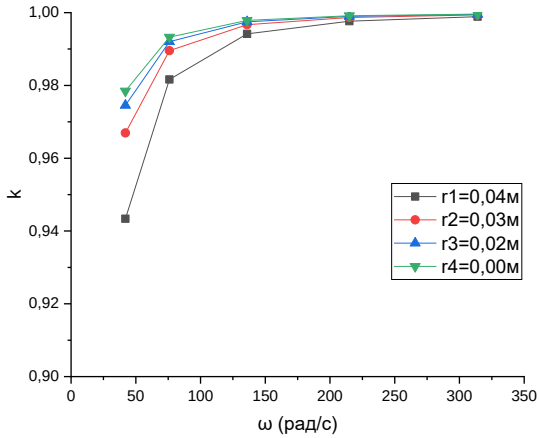

Figure 5. Dependence of the liquid flow distribution coefficient on the static pressure in the total flow rate for different angular velocities of the rotor

Figure 5 shows that the preliminary static pressure in the supply line has a significant effect on the flow rate only at low rotor speeds (up to ω = 76 rad / s), and with increasing angular velocity, its influence decreases and the coefficient k tends to 1. This is due to the fact that with an increase in the angular velocity of the rotor, the fluid pressure at the throttle openings is several times higher than the static pressure in the supply line.

It should also be noted that the value of the coefficient of distribution of fluid flow from static pressure k depends on the angular velocity of the rotor and the inner radius of the fluid ring in the drum, but does not depend on the diameter of the throttle opening.

It follows from the above that the experimental values obtained at the stand are applicable to a thermal installation at certain positions of the liquid ring in the rotor drum.

Since during experimental studies [2] the flow meter 11 shows the total main flow rate of the liquid, the inertial flow rate is determined by the expression

$$Q_i = k \cdot Q. \quad (4)$$

It follows from expression (4) that the inertial flow rate and the flow through the throttle openings of the thermal installation are identical.

Knowing that the inertial radial velocity can be represented as

$$\upsilon_i = \frac{k \cdot Q}{S} = \frac{Q_i}{S}, \quad (5)$$

where S – the area of the throttle opening.

However, in most practical situations, the effect of coriolis forces on the flow of liquid through the throttle openings of a rotating vessel is insignificant and can be ignored. This is due to the fact that the influence of coriolis forces on the flow of liquid depends on many factors, such as the speed of rotation of the vessel, the diameter of the holes and other parameters, which in most cases are not critical for the flow of liquid.

Conclusions

To determine the effect of the diameters of the throttle holes on the fluid flow of the inertial hydrodynamic installation, an experimental stand was made. The results of the experiment showed that the larger the diameter of the throttle opening, the higher the fluid flow.

Using the calculated pressures, the theoretical flow rate of the liquid for the diameters of the throttle opening 1.5, 2, 3 mm was determined, as well as the effect of the preliminary static pressure on the total theoretical flow rate. The calculated data showed that with an increase in the angular velocity of the rotor, the fluid pressure at the walls of the throttle opening increases, and the proportion of fluid flow from the preliminary static pressure in the total flow decreases. The obtained dependence showed that the preliminary static pressure in the supply line has a significant effect on the flow rate only at low rotor speeds (up to ω = 76 rad / s), and with increasing angular velocity, its influence decreases and the coefficient k tends to 1 regardless of the diameter of the throttle holes. This is due to the fact that with an increase in the angular velocity of the rotor, the fluid pressure at the throttle openings is several times higher than the static pressure in the supply line.

Acknowledgements

This research is funded by the Science Committee of the Ministry of Science and Higher Education of the Republic of Kazakhstan (Grant No. AP19678501).

References

1 Калинин А.А. Параметрическая оптимизация электротехнологического комплекса для автономного теплоснабжения / А.А. Калинин. — Караганда, 2018. — 150 с. — [Электронный ресурс]. — Режим доступа: https://www.kstu.kz/wp-content/uploads/dis/Калинин%20А%20А%20Диссертация.pdf

2 Меркулов А.П. Вихревой эффект и его применение в технике / А.П. Меркулов. — М.: Машиностроение, 1969. — 185 с.

3 Гуцол А.Ф. Эффект Ранка / А.Ф. Гуцол // УФН. — 1997. — Т. 167. — Вып. 6. — С. 665–687.

4 Калинин А.А. Архитектура автоматизированной системы научных исследований энергетических характеристик ГДН с трубным ротором / А.А. Калинин // Научные тр. Междунар. симпоз. «Информационные и системные технологии в индустрии, образовании и науке» (21–22 сентября 2006 г.). — Караганда: Изд-во Караганд. гос. техн. ун-та, 2006. — С.110–112.

5 Мохаммад А.А. Расчет дроссельного устройства разогрева рабочей жидкости гидропривода с автоматическим управлением в зависимости от температуры / А.А. Мохаммад, И.А. Хорош, М.А.Титов, Н.П. Куликова // Вестн. КрасГАУ, 2015. — № 12. — С. 38–44. — [Электронный ресурс]. — Режим доступа: https://elibrary.ru/item.asp?id=25054268)6.

6 Пасюк А.С. Гидродинамический нагреватель жидкости в пищевой промышленности / А.С. Пасюк // Вестн. науки и образования. — 2018. — Т. 1, № 2 (38). — С. 30–33. — [Электронный ресурс]. — Режим доступа: https://elibrary.ru/item.asp?id=32430829)

7 Шумилов И.С. Температура рабочей жидкости авиационных гидросистем / И.С. Шумилов // Машины и установки: проектирование, разработка и эксплуатация. — 2016. — № 2. — С. 51–75. — [Электронный ресурс]. — Режим доступа: https://www.researchgate.net/publication/301945902_Fluid_Temperature_of_Aero_Hydraulic_Systems/fulltext/573a6fcc08aea45ee83f8e17/Fluid-Temperature-of-Aero-Hydraulic-Systems.pdf

8 Oshanov Y. Influence of the main properties of the liquid on the temperature indicators of the inertial heat generator [Electronic resource] / Y. Oshanov, M. Ovcharov, B. Nussupbekov, M. Stoev // Bulgarian Chemical Communications. — 2020. — Vol. 52. — P. 188–191. Access mode: http://www.bcc.bas.bg/BCC_Volumes/Volume_52_Special_A_2020/BCC-52-A.pdf.

9 Nussupbekov B. Development and creation of a hydrodynamic liquid heating unit / B. Nussupbekov, Y. Oshanov, M. Ovcharov, E. Mussenova, D. Ospanova, M. Bolatbekova // Eastern-European Journal of Enterprise Technologies. — 2022. — N 5/8 (119). — P. 62–69. doi: https://doi.org/10.15587/1729-4061.2022.264227

10 Oshanov E.Z. Influence of inertial forces on the flow rate velocity of fluid outflow through the throttle bores of the rotor / E.Z. Oshanov, M.S. Ovcharov, B.R. Nusupbekov // Heat Transfer Research. — 2022. — N 53(14). — P. 1–8. https://www.scopus.com/record/display.uri?eid=2-s2.0-85134825340&origin=resultslist&sort=plf-f

Б.Р. Нусупбеков, М.С. Овчаров, Е.З. Ошанов, У.Б. Есбергенов, М.С. Дуйсенбаева,
А.А. Тишбеков, М.Қ. Аманжолова

Дроссель саңылау диаметрлерінің инерциялық гидродинамикалық қондырғының сұйықтық ағынына әсерін анықтау

Мақалада ғимараттар мен құрылыстарды жылытуға байланысты электр энергиясын жылу энергиясына айналдырудың экологиялық мәселелерін шешуге бағытталған әдістер мен процестер қарастырылған. Құйынды, кавитациялық, кавитациялық-құйынды, айналмалы сияқты белгілі жылу қондырғылары тұтынушылардың талаптарын толық қанағаттандырмайды. Осы жағдайларда тиімді шешімдерді іздеу өзекті міндет болып табылады. Мұндай шешімдерге сұйықтықтың айналмалы массасының инерция күштерімен дроссельдік тесіктерге қысым жасау арқылы жылу энергиясын алу әдісі жатады. Дроссель саңылаулары арқылы сұйықтық ағынын анықтау үшін эксперименттік стенд жасалды. Стендтің көмегімен біз диаметрі 1.5, 2, 3 мм дроссель саңылаулары арқылы сұйықтық ағынын анықтадық. Тәжірибе барысында дроссель саңылауының диаметрі неғұрлым үлкен болса, сұйықтық ағыны соғұрлым жоғары болатындығы белгілі болды. Дегенмен, дроссель саңылауының диаметрін шамадан тыс ұлғайтуға болмайды, себебі бұл дроссель саңылауларында қысым жасауды қиындатады. Ротордың бұрыштық жылдамдығының жоғарылауымен дроссель саңылауларындағы сұйықтық қысымы артып, жалпы ағынның алдын-ала статикалық қысымынан сұйықтық ағынының үлесі төмендейтіні анықталды. Жеткізу желісіндегі алдын-ала статикалық қысым ротордың үлкен айналымымен ғана емес (ω =76 рад/с дейін) ағынға айтарлықтай әсер ететіні сөзсіз, ал бұрыштық жылдамдықтың өсуімен оның әсері азаяды және коэффициент k 1-ге ұмтылады.

Кілт сөздер: құйынды әсер, кавитация, бұралған ағын, кинетикалық энергия, дроссель саңылауы, сұйықтық.

Б.Р. Нусупбеков, М.С. Овчаров, Е.З. Ошанов, У.Б. Есбергенов, М.С. Дуйсенбаева,
А.А. Тишбеков, М.К. Аманжолова

Определение влияния диаметров дроссельных отверстий на поток жидкости инерционной гидродинамической установки

В статье для решения экологических проблем, связанных с обогревом зданий и сооружений, рассмотрены способы преобразования электрической энергии в тепловую и процессы, происходящие при этом. Известные тепловые установки, такие как вихревые, кавитационные, кавитационно-вихревые, ротационные не в полной мере удовлетворяют требованиям потребителей. В данных условиях поиск эффективных решений является актуальной задачей. К таким решениям можно отнести способ получения тепловой энергии путем создания давления у дроссельных отверстий силами инерции вращающейся массы жидкости. Для определения расхода жидкости через дроссельные отверстия был изготовлен экспериментальный стенд. С помощью стенда нами был определен расход жидкости через дроссельные отверстия диаметром 1,5; 2; 3 мм. В ходе эксперимента было выявлено, что чем больше диаметр дроссельного отверстия, тем выше расход жидкости. Однако нельзя чрезмерно увеличивать диаметр дроссельного отверстия, так как это осложнит создание давления у дроссельных отверстий. Установлено, что с повышением угловой скорости ротора растет давление жидкости у дроссельных отверстий, а доля расхода жидкости от предварительного статического давления в общем расходе снижается. Определено, что предварительное статическое давление в подводящей магистрали оказывает существенное влияние на расход только при небольших оборотах ротора (до ω = 76 рад/с), а с ростом угловой скорости ее влияние уменьшается и коэффициент *k* стремится к 1.

Ключевые слова: вихревой эффект, кавитация, закрученный поток, кинетическая энергия, дроссельное отверстие, жидкость.

References

1 Kalinin, A.A. (2018). Parametricheskaia optimizatsiia elektrotekhnologicheskogo kompleksa dlia avtonomnogo teplosnabzheniia [Parametric optimization of electrotechnological complex for autonomous heat supply]. Karaganda. Retrieved from https://www.kstu.kz/wp-content/uploads/dis/Калинин%20А%20А%20Диссертация.pdf [in Russian].

2 Merkulov, A.P. (1969). Vikhrevoi effekt i ego primenenie v tekhnike [Vortex effect and its application in technology]. Moscow: Mashinostroenie [in Russian].

3 Gutsol, A.F. (1997). Effekt Ranka [Runque effect] / A.F. Gutsol. *UFN*, 167, 6, 665–687 [in Russian].

4 Kalinin, A.A. (2006). Arkhitektura avtomatizirovannoi sistemy nauchnykh issledovanii energeticheskikh kharakteristik GDN s trubnym rotorom [Architecture of an automated system for scientific research of the energy characteristics of a gas pump with a pipe rotor]. *Nauchnye trudy Mezhdunarodnogo simpoziuma «Informatsionnye i sistemnye tekhnologii v industrii, obrazovanii i nauke» (21–22 sentiabria 2006 g.) — Scientific proceedings of the International Symposium "Information and System Technologies in Industry, Education and Science" (September 21-22, 2006).* Karaganda: Izdatelstvo Karagandinskogo gosudarstvennogo tekhnicheskogo universiteta, 110–112 [in Russian].

5 Mokhammad, A.A., Khorosh, I.A., Titov, M.A., & Kulikova, N.P. (2015). Raschet drosselnogo ustroistva razogreva rabochei zhidkosti gidroprivoda s avtomaticheskim upravleniem v zavisimosti ot temperatury [The calculation of the throttle device heating working fluid of hydraulic drive having a temperature dependence]. *Vestnik Krasnoiarskogo gosudarstvennogo agrarnogo universiteta — Bulletin of Krasnoyarsk State Agrarian University*, 12, 38–44. Retrieved from https://elibrary.ru/item.asp?id=25054268)6 [in Russian].

6 Pasyuk, A.S. (2018). Gidrodinamicheskii nagrevatel zhidkosti v pishchevoi promyshlennosti [Hydrodynamic liquid heater in the food industry]. *Vestnik nauki i obrazovaniia — Bulletin of Science and Education, 1* (2 (38)), 30–33. Retrieved from https://elibrary.ru/item.asp?id=32430829) [in Russian].

7 Shumilov, I.S. (2016). Temperatura rabochei zhidkosti aviatsionnykh gidrosistem [Temperature of the working fluid of aircraft hydraulic systems]. *Mashiny i ustanovki: proektirovanie, razrabotka i ekspluatatsiia — Machines and plants: design, development and operation*, 2, 51–75. Retrieved from https://www.researchgate.net/publication/301945902_Fluid_Temperature_of_Aero_Hydraulic_Systems/fulltext/573a6fcc08aea45ee83f8e17/Fluid-Temperature-of-Aero-Hydraulic-Systems.pdf [in Russian].

8 Oshanov, Y., Ovcharov, M., Nussupbekov, B., & Stoev, M. (2020). Influence of the main properties of the liquid on the temperature indicators of the inertial heat generator. *Bulgarian Chemical Communications*, 52, 188–191. Retrieved from http://www.bcc.bas.bg/BCC_Volumes/Volume_52_Special_A_2020/BCC-52-A.pdf.

9 Nussupbekov, B., Oshanov, Y., Ovcharov, M., Mussenova, E., Ospanova, D., & Bolatbekova, M. (2022). Development and creation of a hydrodynamic liquid heating unit. *Eastern-European Journal of Enterprise Technologies, 5* (8 (119)), 62–69. doi: https://doi.org/10.15587/1729-4061.2022.264227

10 Oshanov, E.Z., Ovcharov, M.S., & Nusupbekov, B.R. (2022). Influence of inertial forces on the flow rate velocity of fluid outflow through the throttle bores of the rotor. *Heat Transfer Research*, *53*(14), 1–8. https://www.scopus.com/record/display.uri?eid=2-s2.0-85134825340&origin=resultslist&sort=plf-f

DOI 10.31489/2023PH4/91-95

UDC 620.193

A.T. Berdibekov[1], V.Ch. Laurinas[2], A.V. Dolya[1], V.V. Gruzin[1], S.A. Guchenko[2*], A.S. Baltabekov[2]

[1]Research Institute of Arms and Military Equipment of the Military Research Center of the National Defense University named after the First President of the Republic of Kazakhstan – Elbasy, Astana, Kazakhstan;
[2] Karaganda Buketov University, Karaganda, Kazakhstan
[*]Corresponding authors e-mail: guchen@mail.ru

Possibility of using inexpensive steel protected by deposited vacuum-arc coatings as a basis for parts and tools coating technology

The aim of the work was to identify the possibility of using under extreme conditions parts made of inexpensive steel, protected by sequentially deposited films ─ Cr and then simultaneously TiN + CrN, micron thickness. Steel grade St3 (Fe ~ 97%) was chosen as the basis. In our country, as in many others, this steel is not only the most common structural material with easy processing and low cost, but also produced in large volumes. The deposition of two consecutive layers of films ─ Cr and TiN + CrN on steel substrates was carried out using vacuum-arc technology (Arc-PVD). The measurements were carried out after the process of periodic heating of the samples to a temperature of 650^0C, followed by rapid cooling, implemented by immersing the samples in water. The main parameters of the coating were measured ─ wear resistance, heat resistance, microhardness. Each thermal effect lasted 20 hours, and the entire heating-cooling process was carried out 5 times. The results obtained in this work can be considered very promising for the protection of inexpensive steels.

Keywords: **v**acuum-arc technology, protective coating, wear resistance, heat resistance, microhardness.

Introduction

Starting from the end of the sixties of the last century, cutting tools with protective coatings applied to them began to appear on the international market. Since then, various methods have been used for applying coatings for various purposes to machine parts and mechanisms. Among a wide range of technologies for applying protective coatings, vacuum ion-plasma methods find great attention [1-6]. Their feature is the direct conversion of electrical energy into technological impact, based on structural-phase transformations in the precipitated condensate.

Currently, work is being intensively carried out to save expensive metals. With their help, cutting tools are made, as well as parts operating in an air atmosphere at high temperatures. One of the solutions to this problem can be the vacuum-arc deposition of protective coatings on parts made from more economical alloys. In this case, the thickness of the deposited films usually lies in the range of several microns. Such an insignificant film thickness is quite enough to, for example, significantly improve corrosion resistance, heat and heat resistance, wear resistance, and also reduce the coefficient of friction of parts. Thus, coatings meet many parameters of operational and technological requirements.

Materials and experimental details

For the deposition of two layers ─ Cr and TiN + CrN on steel substrates, the vacuum-arc technology (Arc-PVD) was used, which also has another name ─ cathode ion bombardment (CIB). Using this technology, a Cr coating was deposited in an argon atmosphere at a pressure of 0.1 Pa. Further, after removing argon from the chamber and replacing it with nitrogen, also at a pressure of 0.1 Pa, a CrN + TiN film was deposited simultaneously with two cathodes [7].

The films were deposited in an NNV-6.6-I1 vacuum setup, in which chromium and titanium cathodes were installed. The third was a plasma source with an incandescent cathode, which, at a current of 20 A, made it possible to clean the substrate surfaces by ion (Ar+) bombardment before coating [5]. During the deposition of coatings, the temperature of the substrates after ion cleaning was maintained at ~450^0C, which significantly increased adhesion.

It should be noted that the design of the HNV-6.6-I1 setup allows one to deposit films on all surfaces of the substrates, since the substrates in the installation chamber rotate both around their axis and in a circle, with adjustable speeds of both rotations. This option made it possible to load 12 substrates for carrying out

the planned experiments. At least such a number of samples was necessary because the process of thermal action leads to an increase in the mass of the sample, and the measurement of wear resistance leads to a decrease. In this regard, one group of 5 samples was used to measure heat resistance, the second, also of 5 samples, was used to measure wear resistance. In addition, because when measuring wear resistance, friction contact was made at 20 points of the film surface, the sample that passed the wear resistance test was no longer used.

The substrates were made of St3 steel. They were a disk, 25 mm in diameter and 3 mm thick. Both planes of the disc were ground on a surface grinder, and since coatings were planned to be applied to all surfaces of the substrate, they were polished on a polishing machine. Next, the substrates were washed in an ultrasonic bath and treated with steam using a steam-jet device, wiped with coarse calico soaked in ethanol, placed in an oven and kept in it for two hours at a temperature of 150^0C.

Results and discussion

In the first series, a TiN + CrN coating was deposited on the substrates without an intermediate Cr layer. The St3 steel substrate showed a low Vickers microhardness (194 HV) measured on an HVS-1000A instrument. The adhesion of the deposited TiN + CrN layer also turned out to be low. Probably, this led to the fact that the film cracked when trying to measure its microhardness. The crack is quite well observed along the circumference of the indenter, which is shown in Figure 1.

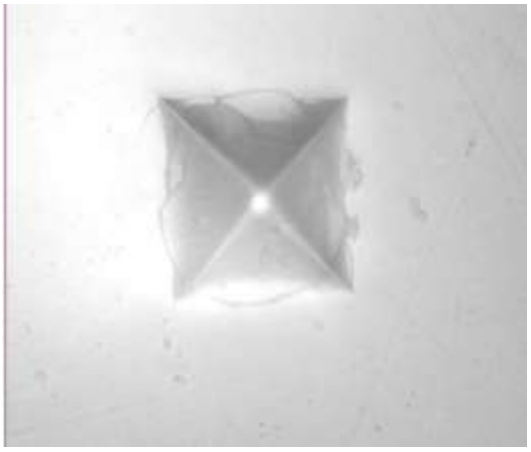

Figure 1. Image taken during microhardness measurement (400 magnification).

To exclude the occurrence of such defects in the future, a layer of chromium with a thickness of ~3 μm was deposited, which has a higher microhardness compared to the substrate.

After making sure that the deposited chromium layer does not crack during microhardness measurements, layers of Cr (~3 μm thick) and TiN + CrN (~5 μm thick) were successively deposited on 12 substrates.

Figure 2 shows the spectrum taken from the applied coating, which was not subjected to thermal action, using a MIRA-3 LMU scanning electron microscope.

Next, the microhardness and wear resistance to thermal impact were measured. The results are shown in Table. To measure the wear resistance parameters, we used a tribometer developed by employees of the Research Center for Ion-Plasma Technologies and Modern Instrumentation [5] and a RADWAG AS60/220R2 electronic balance with an accuracy of 0.06 mg.

To determine the effect of thermal action on microhardness and wear resistance, as well as the heat resistance of the coating itself, the samples were placed in a muffle furnace at a temperature of 650^0C [8]. The temperature was maintained in automatic mode with an accuracy of 5^0C for 20 hours, then the oven was turned off and the samples were placed in distilled water at a temperature of 15^0C in a twenty-liter thermostat. After rapid cooling, the samples were dried with a stream of warm air and were ready for measurements. With such a sequence, the procedures were performed in 5 cycles.

All obtained measurement results are shown in Table.

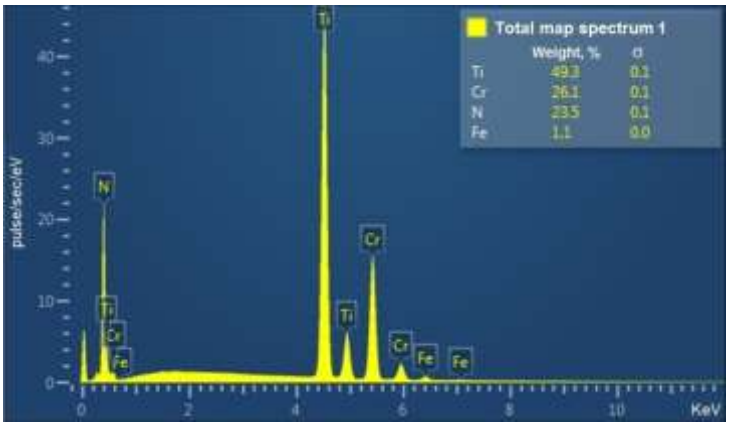

Figure 2. Spectrum taken from the central part of the sample using a scanning electron microscope before thermal treatment.

T a b l e

The table shows the dynamics of the weight gain of samples under the influence of temperature, the parameters of microhardness and the rate of abrasion of coatings

N	Microhardness, HV	Wear rate, μg/s	Dynamics of weight gain of samples exposed to a temperature of 650^0C for 20 hours, μg/cm^2
Before thermal exposure	830	0.020	0
After 1 cycle	780	0.023	0.287
After 2 cycles	760	0.025	0.205
After 3 cycles	750	0.025	0.163
After 4 cycles	740	0.025	0
After 5 cycles	740	0.025	0

Figure 3 shows the spectrum taken from the coating after passing through all 5 cycles of thermal exposure using a MIRA-3 LMU scanning electron microscope.

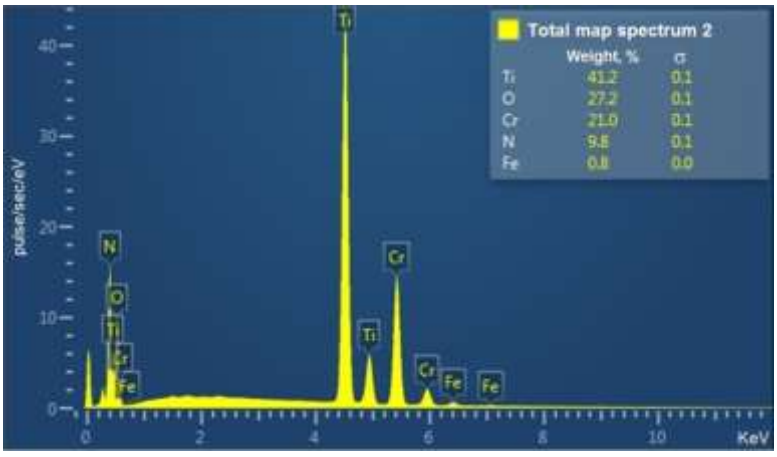

Figure 3. Spectrum taken from a coating on a substrate using a scanning electron microscope.

All parameters obtained as a result of thermal exposure are shown in Table.

Before the thermal treatment of the samples, their coating color was light yellow, the wear rate was 0.020 μg/s, and the microhardness was 830 HV.

After passing through the first cycle of thermal exposure, the color of the coatings changed and became saturated yellow, the mass of the samples increased by 0.287 μg/cm^2, the wear rate increased to 0.023 μg/s, and the microhardness decreased to 780 HV. The second cycle changed the color to dark yellow, the mass of the samples increased by another 0.205 μg/cm^2, the wear rate increased to 0.025 μg/s, and the microhardness decreased to 760 HV.

The impact of the third cycle led to a change in the color of the coating, it turned purple, the weight of the samples increased by 0.163 μg/cm^2, the wear rate did not change, 0.025 μg/s, and the microhardness decreased to 750 HV.

Completion of the fourth and last, fifth, cycles did not lead to a change in the color of the coatings, as well as the wear rate. As for the mass gain, the further dynamics of the mass gain became equal to zero. The microhardness, which decreased to 740 HV after the fourth cycle, also did not change after the fifth.

Thus, it follows from the obtained data that over the entire studied time interval (100 hours) of keeping the samples at 650°C, the dependence of the mass increase slows down over time, and after 80 hours becomes close to zero. This fact can be explained by the fact that practically one of the components, titanium nitride, was completely converted into titanium oxides, and chromium nitride at this temperature was little susceptible to oxidation.

As for the change in the color of the films, it can most likely be assumed that titanium nitride, which gives a light yellow color, is mainly converted into oxides. Chromium nitride gives a gray color, while chromium oxides can only be green or black. At the first stage of thermal treatment, mainly TiO appears, leading to the appearance of yellow and dark yellow color of the samples. The emerging Ti_2O_3 gives a violet color, so a dark yellow color appeared.

Conclusions

Thus, using the results obtained in the work, we can draw a number of conclusions:

1) The obtained dynamics of change in the mass of the samples, which became equal to zero already after the fourth cycle and did not change any more, allows us to speak about the high thermal stability of the applied coatings at temperatures not exceeding 650^{0}C.

2) The wear resistance of the protective coating is more than 2 orders of magnitude greater than the wear resistance of St3 steel, and is little affected by changes after thermal exposure.

3) Stabilization of microhardness and wear resistance, which also appeared after the fourth cycle, indicates the possibility of using these coatings at large temperature differences ― in the range from heating 650^{0}C to rapid cooling to 15^{0}C.

Consequently, the results obtained correspond in a number of cases to the possibility of using parts made of St3 steel with sequentially deposited micron layers of Cr and TiN + CrN, and operation is also possible at high temperatures.

Acknowledgments

This scientific article was published as part of the implementation of the scientific program of program-targeted funding for 2021-2023 IRN № BR1090150221 “Development of technology for protective coatings of surfaces of weapons and military equipment to protect against aggressive environmental factors and operating conditions” (the study is funded by the Science Committee of the Ministry of Education and science of the Republic of Kazakhstan).

References

1 Holmberg, K., & Erdemir, A. (2017). Influence of tribology on global energy consumption, costs and emissions. VTT Technical Research Centre of Finland, 360 p.

2 Cha, S. (2015). (Eds.) Consumption Due to Friction in Motored Vehicles and Low-Friction Coatings to Reduce It. Springer International Publishing Switzerland: Coating Technology for Vehicle Applications, 248 p.

3 Reshetnyak, E.N., & Strelnitsky, V.E. (2008). Synthesis of strengthening nanostructured coatings Issues of Atomic Science and Technology, 2, 119-130.

4 Yurov, V.M., Laurinas, V.Ch., Guchenko, S.A., et al. (2013). Structure and properties of multiphase ion-plasma coatings. Karaganda: Publishing and Printing Center of the Kazakh Russian University, 150 p.

5 Guchenko, S.A., Eremin, E.N., Zavatskaya, O.N., et al. (2019). Effect of N_2 and Ar on the properties of multicomponent ion-plasma coatings 12X18H10T+Cu+Al. *IOP Conf. Series: Journal of Physics: Conf. Series,* 1260, 062009,

6 Urbahs, A. (Eds.). (2018). Evaluation of the Physical and Mechanical Characteristics of Ion-Plasma Antifriction Coatings Based on Ti-Cu. *Trans Tech Publications Ltd, Switzerland: Key Engineering Materials Submitted,* 366 p.

7 Barshilia Harish, C., Anjana Iain, & Rajam, K.S. (2004). Structure, hardness and thermal stability of nanolayered TiN/CrN multilayer coatinqs. *Vacuum, Vol*. 72, 241–248.

8 Laurinas, V.Ch., Syzdykova, A.Sh., Eremin, E.N., et al. (2015). High-temperature strength and corrosion resistance of alloy steel coatings. *Bulletin of the University of Karaganda-Physics, 4* (80), 24–3.

А.Т. Бердібеков, В.Ч. Лауринас, А.В. Доля, В.В. Грузин, С.А. Гученко, А.С. Балтабеков

Вакуумды-доғалы технологиямен қапталған жабындармен қорғалған арзан болатты бөлшектер мен құралдардың негізі ретінде пайдалану мүмкіндігі

Негіз ретінде St3 (Fe~97%) маркалы болат таңдалды. Аталған марка біздің және өзге де елдерде болат өңдеуге оңай, құны арзан, ең кең таралған конструкциялық материал болып табылады және үлкен көлемде шығарылады. Cr және TiN + CrN қатарлас екі қабықша қабаттарымен болат төсемелерін қаптау вакуумдық-доғалық технология арқылы жүзеге асырылды (Arc-PVD). Өлшем үлгілері 6500С температураға дейін мезгіл-мезгіл қыздыру процесінен кейін үлгілерді суға батыру арқылы жылдам салқындату арқылы жүргізілді. Қаптаманың тозуға төзімділік, ыстыққа төзімділік, микроқаттылық сияқты негізгі параметрлері өлшенді. Әрбір термиялық экспозиция 20 сағатқа созылды, ал барлық қыздыру-салқындату процесі 5 рет жүргізілді. Бұл жұмыста алынған нәтижелерді арзан болаттарды қорғау үшін өте перспективалы деп санауға болады.

Кілт сөздер: вакуумды-доғалық технология, қорғаныш қаптама, тозуға төзімділік, ыстыққа төзімділік, микроқаттылық.

А.Т. Бердибеков, В.Ч. Лауринас, А.В. Доля, В.В. Грузин, С.А. Гученко, А.С. Балтабеков

Возможность использования в качестве основы деталей и инструментов недорогой стали, защищенной нанесенными вакуумно-дуговой технологией покрытиями

В качестве основы была выбрана сталь марки St3 (Fe~97 %). В нашей стране, как и во многих других, данная сталь не только является наиболее распространенным конструкционным материалом, обладающим легкой обработкой и низкой стоимостью, но и производится в больших объемах. Нанесение двух последовательных слоев пленок — Cr и TiN + CrN — на стальные подложки производилось с использованием вакуумно-дуговой технологии (Arc–PVD). Измерения проводились после процесса периодического нагрева образцов до температуры 650^0C с последующим быстрым охлаждением, реализованным путем погружения образцов в воду. Измерялись основные параметры покрытия: износостойкость, жаростойкость, микротвердость. Каждое термическое воздействие длилось 20 ч, а весь процесс «нагрев–охлаждение» проводился 5 раз. Результаты, которые были получены в настоящей работе, можно считать весьма перспективными для защиты недорогих сталей.

Ключевые слова: вакуумно-дуговая технология, защитное покрытие, износостойкость, жаростойкость, микротвердость.

АВТОРЛАР ТУРАЛЫ МӘЛІМЕТТЕР
СВЕДЕНИЯ ОБ АВТОРАХ
INFORMATION ABOUT AUTHORS

Abdukarimov, Abdullaziz — PhD, associate professor of Namangan Engineering and Technology Institute, Namangan, Kasansay st.7, 160115, Uzbekistan. E-mail: abdullaziz.abdukarimov@mail.ru; ORCID: 0000-0003-2384-3249;

Aimukhanov, A.K. — Candidate of physical and mathematical sciences, associate professor, professor of the Department of radiophysics and electronics, leading researcher, Karaganda Buketov University, Scientific Center for Nanotechnology and Functional Nanomaterials, Karaganda, Kazakhstan;

Amanzholova, M.K. — teacher, master of technical sciences, Department of transport and logistics systems, Karaganda Buketov University, Karaganda, Kazakhstan, E-mail: makpal.amanzholova@yandex.ru;

Baiman, Gulzagira — Senior lecturer, Department of physics, M.O. Auezov South Kazakhstan University, Shymkent, Kazakhstan; bgb_zht@mail.ru; ORCID ID: https://orcid.org/0000-0003-4250-842X;

Baltabekov, Askhat — PhD, associate professor, Department of physics and nanotechnology, Karaganda Buketov University, Karaganda, Kazakhstan; abskargu@mail.ru; ORCID ID: https://orcid.org/0000-0001-8829-2527;

Beisembekov, M.K. — 1 year PhD student, Karaganda Buketov University, Karaganda, Kazakhstan;

Berdibekov, Aidar – PhD, associate professor, colonel, head of the research, Institute of Weapons and Military Equipment of the Military Research Center of the National Defense University named after the First President of the Republic of Kazakhstan – Elbasy, Astana, Kazakhstan. ORCID ID: 0000-0002-1255-7637;

Bezvesilnaya, E.N. (contact person) — Doctor of technical sciences, professor, Department of automation and non-destructive testing systems, National Technical University of Ukraine “Igor Sikorsky Kyiv Polytechnic Institute”, Ukraine, E-mail: o.bezvesilna@gmail.com;

Buitkenov, D.B. — PhD in “Physics”, leading researcher of the research center “Surface Engineering and Tribology”, S. Amanzholov East Kazakhstan University, Ust-Kamenogorsk, Kazakhstan;

Dolya, Alexander — Master (Sci.), major, head of the Research Service of the engineering and technical Department of the Research Institute of Weapons and Military Equipment of the Military Research Center of the National Defense University named after the First President of the Republic of Kazakhstan – Elbasy, Astana, Kazakhstan;

Duisenbayeva, M.S. (contact person) — doctoral student, master of natural sciences, Department of Engineering Thermophysics named after Professor Zh. S. Akylbayev, Karaganda Buketov University, Karaganda, Kazakhstan, E-mail: m_o_l_d_i_r_89@mail.ru;

Dzhakupova, Moldir — 2nd year master student, Department of Physics and Nanotechnology, Karaganda Buketov University, Karaganda, Kazakhstan; moldir.93@inbox.ru;

Fedorenko, O.V. (contact person) — Candidate of physical and mathematical sciences, associated professor, Al-Farabi Kazakh National University, Almaty, Kazakhstan; e-mail: fedor23.04@mail.ru;

Girnis, Svetlana — Candidate of technical sciences, associate professor of the Faculty of Architecture and Construction, Toraighyrov University, Pavlodar, Kazakhstan, E-mail: girnis@mail.ru; ORCID: 0000-0002-4955-9476;

Gruzin, Vladimir — Doctor of eechnical science, professor, senior researcher, Research Institute of Weapons and Military Equipment of the Military Research Center of the National Defense University named after the First President of the Republic of Kazakhstan – Elbasy, Astana, Kazakhstan. ORCID ID: 0000-0002-1128-5246;

Guchenko, Sergey — Master (Sci.), junior researcher, Research center “Ion-plasma technologies and modern instrumentation”, Karaganda Buketov University, Karaganda, Kazakhstan. ORCID ID:0000-0002-9954-5478;

Hrynevych, Mariia Stepanivna — Assistant of the Department of robotics, Power Engineering and Automation named after Prof. B.B. Samotokina State University “Zhytomyr Polytechnic”, Ukraine, E-mail: kakit_gms@ztu.edu.ua;

Kambarov Y.Y. (contact person) — 3rd year PhD student, International school of engineering, D. Serikbayev East Kazakhstan Technical University, Ust-Kamenogorsk, Kazakhstan; e-mail: yedilzhan@gmail.com;

Kayumova Ainur — 1st year PhD student, Department of physics and nanotechnology, Karaganda Buketov University, Karaganda, Kazakhstan; aneka.08@mail.ru; ORCID ID: https://orcid.org/0000-0003-4684-0083;

Kengesbekov A.B. — postdoctoral student, Junior Researcher of Plasma Science LLP, Ust-Kamenogorsk, Kazakhstan;

Kossov, V.N. (contact person) — Doctor of physical and mathematical sciences, professor, corresponding member of the National Academy of Sciences of the Republic of Kazakhstan, Academician of the National Academy of Sciences of the High School of RK, Head of the Physics Department, Abai Kazakh National Pedagogical University, Almaty, Kazakhstan; e-mail: kosov_vlad_nik@list.ru;

Krasikov, S.A. — Candidate of technical sciences, leading research scientist, Abai Kazakh National Pedagogical University, Almaty, Kazakhstan; e-mail: sa.krassikov@mail.ru;

Kufian MohdZieaudin — PhD, associate professor of University of Malaya, Kuala lumpur. Malaysia;

Kyrychuk Yuriy Volodymyrovych — Doctor of technical sciences, professor, head of the Department of automation and non-destructive testing systems national technical university of Ukraine “Igor Sikorsky Kyiv Polytechnic Institute”, Ukraine, E-mail: y.kyrychuk@kpi.ua;

Laurinas Vytautas — Candidate of physical and mathematical sciences sciences, associate professor, Physical-Technical Faculty, Karaganda Buketov University, Karaganda, Kazakhstan. ORCID ID: 0000-0001-7079-254X;

Makashev Kuanysh — PhD, senior lecturer of the Faculty of Architecture and Construction, Toraighyrov University, Pavlodar, Kazakhstan, E-mail: makashevkuanysh10@gmail.com; ORCID: 0009-0005-2971-6322;

Makhabayeva A.T. — Senior lecturer of the Department of radiophysics and electronics, Karaganda Buketov University, Karaganda, Kazakhstan;

Nedopekin Oleg — PhD, Associate Professor, Department of general physics, Kazan Federal University, Kazan (Volga Region), Russia; Oleg.Nedopekin@kpfu.ru; ORCID ID:https://orcid.org/0000-0002-0208-3503;

Nussupbekov, B.R. — Candidate of technical sciences, professor of the Department of engineering thermophysics named after Professor Zh.S. Akylbayev, Karaganda Buketov University, Karaganda, Kazakhstan, E-mail: bek_nr1963@mail.ru;

Oshanov, E.Z. — Senior lecturer of the Department of transport and logistics systems, Karaganda Buketov University, Karaganda, Kazakhstan, E-mail: oshanovez@mail.ru;

Ovcharov, M.S. — Candidate of technical sciences, associate professor of the Department of transport and logistics systems, Karaganda Buketov University, Karaganda, Kazakhstan, E-mail:mihail.ovcharov.40@mail.ru;

Piyanzina Irina — PhD, senior research fellow, Kazan Federal University, Kazan (Volga Region), Russia; i.piyanzina@gmail.com;ORCID ID: https://orcid.org/0000-0003-4251-9196;

Rozhkova X.S. — PhD, Senior Lecturer of the Department of radiophysics and electronics, Karaganda Buketov University, Karaganda, Kazakhstan;

Sagdoldina Zh.B. — PhD in “Technical Physics”, associate professor, senior researcher of the research center “Surface Engineering and Tribology”, S. Amanzholov East Kazakhstan University, Ust-Kamenogorsk, Kazakhstan;

Saidakhmetov Pulat — Candidate of science (physics), assistant professor, Department of physics, M. Auezov South Kazakhstan University, Shymkent, Kazakhstan; timpf_ukgu@mail.ru; ORCID ID: https://orcid.org/0000-0002-9146-047X;

Savilov Sergey — Doctor of chemical sciences, docent, M.V. Lomonosov Moscow State University, Moscow, Russia; savilov@mail.ru; ORCID ID: https://orcid.org/0000-0002-5827-3912;

Serikov Timur (contact person) — PhD, associate professor, Department of physics and nanotechnology, Karaganda Buketov University, Karaganda, Kazakhstan; serikov-timur@mail.ru; ORCID ID: https://orcid.org/0000-0003-4302-9674;

Seydaz, T. — PhD student, Abai Kazakh National Pedagogical University, Almaty, Kazakhstan; e-mail: seydaz.talgat@mail.ru;

Stanevich Viktor — Candidate of technical sciences, associate professor, professor of the Faculty of Architecture and Construction, Toraighyrov University, Pavlodar, Kazakhstan, E-mail: svt_18@mail.ru; ORCID: 0000-0002-7581-2658;

Sultanov Akhmadjon — PhD, associate professor of Namangan Engineering and Technology Institute, Namangan, Kasansay st.7, 160115, Uzbekistan. E-mail.ru: surix@mail.ru;

Tayurskii Dmitrii — Doctor of science (physics and mathematics), professor, vice- rector, Kazan Federal University, Kazan (Volga Region), Russia; Dmitry.Tayurskii@kpfu.ru; ORCID ID:https://orcid.org/0000-0001-6106-7581;

Tazhibayev, S.K. (contact person) — 3nd year PhD student, Karaganda Buketov University, Karaganda, Kazakhstan; e-mail: tazh1981@gmail.com;

Tishbekov, A.A. — Master of technical sciences, Department of transport and logistics Systems, Karaganda Buketov University, Karaganda, Kazakhstan, E-mail: Tishbekov@list.ru;

Tolochko Tatyana Alekseevna — Senior lecturer of the Department of automation and non-destructive testing systems, National Technical University of Ukraine “Igor Sikorsky Kyiv Polytechnic Institute”, Ukraine, E-mail: prilad168@gmail.com;

Ukrainets Vitaliy (contact person) — Doctor of technical sciences, associate professor, professor of the Faculty of Architecture and Construction, Toraighyrov University, Pavlodar, Kazakhstan; E-mail: vitnikukr@mail.ru; ORCID: 0000-0002-6451-5463;

Yesbergenov, U.B. — Director of “BILGE-ORAZ” LLP, Kazakhstan;

Zeinidenov, A.K. — PhD, associate professor of the Department of radiophysics and electronics, dean of the Faculty of physics and technology, Karaganda Buketov University, Karaganda, Kazakhstan;

Zhakanova A.M. — Junior researcher, Karaganda Buketov University, Karaganda, Kazakhstan;

Zhanbirbayeva Perizat — 1st year PhD student, Department of Physics and Nanotechnology, Karaganda Buketov University, Karaganda, Kazakhstan; perizat.zhanbirbaeva@mail.ru; ORCID ID: https://orcid.org/0000-0002-9351-956X;

Zhaneli, M. — PhD student, Abai Kazakh National Pedagogical University, Almaty, Kazakhstan; e-mail: janeli.magjan@gmail.com.

2023 жылғы
«Қарағанды университетінің хабаршысы. “Физика” сериясы»
журналында жарияланған мақалалардың көрсеткіші

Указатель статей, опубликованных в журнале
«Вестник Карагандинского университета. Серия “Физика”»
в 2023 году

Index of articles published in
«Bulletin of the Karaganda University. “Physics” Series»
in 2023

ЖЫЛУФИЗИКАСЫ ЖӘНЕ ТЕОРИЯЛЫҚ ЖЫЛУТЕХНИКАСЫ
ТЕПЛОФИЗИКА И ТЕОРЕТИЧЕСКАЯ ТЕПЛОТЕХНИКА
THERMOPHYSICS AND THEORETICAL THERMOENGINEERING

АРНАЙЫ ШЫҒАРЫЛЫМ
СПЕЦИАЛЬНЫЙ ВЫПУСК
SPECIAL ISSUE